THE UNIVERSITY OF HULL

Investigation into the role of the epigenetic target CBX2 in Glioblastoma

being a Thesis submitted for the Degree of Masters by Research in Biomedical Sciences at the University of Hull

by

Hannah Beattie

BSc (Hons) Biomedical Science

August 2023

Abstract

Glioblastoma (GBM) has been identified as an extremely difficult tumour to treat owing to issues of heterogeneity, as well as the aggressive nature of the tumours' growth. Despite current treatments using a combination of methods, treatment resistance contributes to their eventual failing. Therefore, alternative treatment methods are being explored. One such approach includes exploiting epigenetic targeting of key histone modifications. This investigation focusses on the Chromobox domain 2 (CBX2) protein, which has been shown to be overexpressed in several tumour types, including GBM. CBX2 is involved in histone modification, with it being hypothesised that the downstream effects of CBX2's involvement include silencing of tumour suppressor genes.

This study used both 2D and 3D models to evaluate the role of CBX2 within two GBM cell lines, U-87 MG and SNB-19. RNA interference, through siRNA knockdown, was used to silence CBX2 gene expression in a transient manner. Transfection of plasmids containing full length and chromodomain-depleted CBX2 were also used to cause overexpression of the molecule. The effects of changes to the CBX2 messenger RNA (mRNA) were evaluated using western blotting and RT-qPCR, so as to analyse the change in CBX2 expression at the protein and mRNA level, respectively. An additional first look at the differences of CBX2 expression within a static vs. continuous perfusion microfluidic device also took place, providing a starting point for future investigation of GBM and CBX2, and potentially any other gene of interest, within a more physiologically relevant model.

Key observations included a reduction in cell number within the U-87 MG cell line following the transfection of siCBX2. At the mRNA level, CBX2 expression within SNB-19 was also seen to be significantly reduced, compared to the siScr control, following transfection of siCBX2. CBX2 overexpression altered the expression of CBX2 detected at the protein level, with western blots showing a molecule at 72kDa for the full length CBX2 plasmid and approximately 66kDa for the chromodomain-depleted CBX2 transcript, compared with the 52kDa molecule that was consistently detected in both GBM and breast cancer cell lines. Microfluidic experiments proved successful in maintaining spheroids on-chip for at least 96 hours, with no significant change in CBX2 expression observed between static and dynamic models.

In the future, it is proposed that the microfluidic devices can be used with patient-biopsies so that a personalised response to therapy, standard or alternative, can be assessed in a way that helps plan treatment. Furthermore, the 3D models could be developed to incorporate more components and be used to better understand GBM biology and develop additional treatment strategies.

Acknowledgements

I would like to thank my supervisors, Professor John Greenman and Dr. Mark Wade for their time, patience, and expertise in teaching and guiding me through my project. Thank you for all your help and support.

Thank you to all the PGR students and staff in the Allam 3rd Floor and Hardy 124 laboratories, for your support and technical training. I would also like to thank everyone in the Head and Neck research group based at the Daisy laboratories at Castle Hill Hospital, for all your support and encouragement during the write-up period.

I would like to thank my amazing friends, Danielle Marsh, Katie Sherwood, and Abigail Chappell Dixon for always being there and encouraging me throughout. Finally, a huge thank you to my parents for your unwavering support and believing in me as I complete my Masters.

Contents

List of Figures

List of Tables

Abbreviations

AT	AT hook
AV	Annexin V
BBB	Blood brain barrier
BCA	Bicinchoninic acid
bp	Base pairs
CBX	Chromobox
CCNU	Lomustine
cDNA	Complementary DNA
CNS	Central nervous system
CSC	Cancer stem cells
DCP	Dead-cell protease
DMEM	Dulbecco's modified eagle medium
DMSO	Dimethyl sulfoxide
ECACC	European collection of authenticated cell cultures
ECL	Enhanced chemiluminescence
ECM	Extracellular Matrix
EGFR	Epidermal growth factor receptor
EZH2	Enhancer of zeste homolog 2
FBS	Foetal bovine serum
FDA	Fluorescein diacetate
GAPDH	Glyceraldehyde 3-phosphate dehydrogenase
GBM	Glioblastoma
GEM	Genetically engineered mice
GEO	Gene Expression Omnibus
H&E	Haematoxylin and eosin
H2AK119	H2A lysine 119
H2Aub	Ubiquitination of H2A
H3K20me3	Tri-methylation of H3 at lysine 20
H3K27me3	Tri-methylation of H3 lysine 27
HIF-1α	Hypoxia-Inducible factor 1

HIG2	Hypoxia inducible protein 2
HPH	Human polyhomeotic homolog
IDH	Isocitrate dehydrogenase
IHC	Immunohistochemistry
K	Lysine
kDa	Kilodaltons
LDH	Lactate dehydrogenase
MGMT	O6-methylguanine-DNA-methyltransferase
MRI	Magnetic resonance imaging
mRNA	Messenger RNA
MW	Molecular weight
NP	Nanoparticles
NICE	National Institute for Clinical Excellence
OKN-007	OKlahoma Nitrone 007
PBS	Phosphate buffered saline
Pc	Pc box
PCGF	Polycomb group factor
PCV	Vincristine
PI	Propidium iodide
PMMA	Polymethyl methacrylate
PRC1	Polycomb repressive complex 1
PRC2	Polycomb repressive complex 2
PTM	Post-translational modifications
PVDF	Polyvinylidene difluoride
qPCR	Quantitative polymerase chain reaction
R	Arginine
RBL2	Retinoblastoma-like protein 2
RCF	Relative centrifugal force
RING	Really interesting new gene
RNAi	RNA interference
RPL13A	Ribosomal protein L13a
RPM	Revolutions per minute

RPMI	Roswell park memorial institute
RT	Reverse transcription
RT-qPCR	Quantitative reverse transcription polymerase chain reaction
S	Serine
SDS-PAGE	Sodium dodecyl sulphate–polyacrylamide gel electrophoresis
shRNA	Short hairpin RNA
siRNA	Short interfering RNA
siScr	Scrambled-siRNA
STR	Short tandem repeat
T	Threonine
TBST	Tris buffered saline with added Tween20
TERT	Telomerase reverse transcriptase
TME	Tumour microenvironment
TMZ	Temozolomide
TNBC	Triple negative breast cancer
ULA	Ultra-low adhesion
VEGF	Vascular Endothelial Growth Factor
WHO	World Health Organisation
ΔΔCt	Delta-Delta Ct

Chapter 1: Introduction

1.1. Glioblastoma

Within the clinical world, brain malignancies are considered to be a major problem, as some tumour types are particularly difficult to treat. These malignancies exhibit extreme aggressiveness, generally showing rapid proliferation, with further problems of heterogeneity and the acquisition of treatment resistance. Due to the relatively high morbidity, there is an urgent need for further research into brain tumour biology to improve treatment methodologies.

1.1.1. Background

A glioblastoma (GBM) is a brain tumour seen almost exclusively within the brain or spinal cord. Previously referred to as 'Glioblastoma Multiforme', GBM is highly variable in nature, with multiple different glial brain cells being observed, however the classification was shortened to 'Glioblastoma' in the 4th edition of the World Health Organisation (WHO) Classification of Tumors of the Central Nervous System (CNS) (Louis et al., 2007). It has recently been reclassified by the WHO in the 5th edition of the Classification of Tumors of the CNS; GBM is now classed as a grade IV tumour possessing wildtype isocitrate dehydrogenase (IDH) enzyme and is considered one of the most highly aggressive forms of cancer (Louis et al., 2021). It is thought that GBM develops from astrocytes, neural stem cells, and oligodendrocyte precursor cells following multiple genetic mutations (Shao & Liu, 2018; Yao et al., 2018); however, the exact cellular origins are still disputed. GBM grows extremely quickly, making it imperative that treatment begins as quickly as possible following diagnosis. Studies investigating the growth rate of GBM reported a median percentage specific growth rate of 1.4% per day, with a doubling time for the tumour mass of 49.6 days (Stensjøen et al., 2015). In comparison, Triple Negative Breast Cancer (TNBC), also considered an aggressive form of cancer, has been shown to have a specific growth rate of only 1.0% per day, with a tumour volume doubling time of 103 ± 43 days (Ryu et al., 2014; Lee et al., 2016).

1.1.2. Epidemiology

GBM is one of the most common brain cancers seen, with up to 60% of such malignancies being identified as this type of tumour (Rock et al., 2012; Vitovcova et al., 2020). The prevalence rate of GBM in the United States of America varies between 3.19 - 3.23 cases per 100,000 people/ year (Ostrom et al., 2013; Lukas et al., 2019; Ostrom et al., 2020). The number of cases of GBM is relatively low when compared to other solid malignancies such as breast cancer, which has an incident rate between 93.2 – 130.8 cases per 100,000 people/ year (incidence rates of this tumour type vary greatly due to ethnicity) (DeSantis et al., 2019). However, GBM is particularly difficult to treat, owing to issues associated with the blood brain barrier (BBB), as well as tumour heterogeneity and therapy resistance which develop during treatment. As a result, patient survival is markedly lower when compared with other tumour types; furthermore, patient life expectancy following diagnosis has not significantly improved over the past 20-30 years (Tamimi & Juweid, 2017).

Patient survival following diagnosis is between 12 - 15 months (Stupp et al., 2009; Koshy et al., 2012; Witthayanuwat et al., 2018), despite extensive treatment methods which generally include a combination of surgery followed by radiotherapy and/ or chemotherapy. Molecular profiling techniques are employed to determine the IDH status of the GBM brain tumour, the results of which provide information on the most likely outcome of the patient. Prior to the recent reclassification, it was thought that the majority of primary GBM tumours (approximately 90%) exhibited IDH wildtype status (Ohgaki & Kleihues, 2013; Kim et al., 2021); and are the most aggressive form of malignancies. In comparison, patient survival for those with metastatic TNBC falls at an average of 18 months, with a 5-year survival rate of only 10.81% of patients for those with this type of malignancy (Vagia et al., 2020; Hsu et al., 2022). However, the overall 5-year survival rates for TNBC patients, metastatic and non-metastatic cases, was seen to be much higher, at 81.28% (Hsu et al., 2022).

The majority of GBM cases are seen within older people, with the median age of diagnosis being 64 years old (Ostrom et al., 2013). Additionally, more cases were seen in males than in females (in the USA), with incidence rates of 4.03 and 2.54 per

100,000 people, respectively (Ostrom et al., 2020). A previous study demonstrated the incidence rates of GBM within England, with more cases also observed with male patients, with an average incidence rate of 5.87 for men and 3.54 for women, over a 5-year period (Brodbelt et al., 2015). Another consequence of the recent re-classification of tumours of the CNS is that there is now a separate classification for pediatric-type gliomas of varying grades, even if they have the IDH wildtype, due to the significant clinical differences between adult and pediatric-type gliomas (Louis et al., 2021). This study will focus on adult malignancies.

1.1.3. Tumour Biology

The biology of GBM is strongly influenced by the tumour microenvironment (TME), which provides an environment that generally aids tumour progression and development. The classification of GBM as an aggressive tumour is based upon multiple factors, including a high rate of cell division, and tumour invasiveness into the surrounding brain tissue, a key feature of many forms of glioma (Cuddapah et al., 2014). An additional key hallmark of cancer demonstrated within GBM, is resistance to apoptosis, through the repair of DNA damage incurred during treatment (Krakstad & Chekenya, 2010).

As the tumour grows rapidly, some areas within the tumour are likely to become restricted regarding the blood flow available, and as a result such areas do not have access to the normal oxygen levels and / or nutrient supply (Haar et al., 2012). Areas with low oxygen levels are known as hypoxic, which can trigger the development of cell necrosis, and this is associated with a poorer prognosis for the patient (Lin et al., 2020; Yee et al., 2020). Hypoxic conditions are typically regarded to be around a 2% oxygen level (Kusanto et al., 2021), compared to about 20% in atmospheric air. Hypoxia can aid in the progression of the tumour through the angiogenic pathway, a key feature of tumorigenesis. Neo-angiogenesis, the production of new blood vessels, facilitates tumour progression by improving oxygen and nutrient delivery, allowing the tumour mass to increase further. Angiogenesis is a complex process, with one of the major contributors being Hypoxia-Inducible factor 1 (HIF-1α), which is produced in cells in response to a hypoxic environment, which causes ‘chaotic’ angiogenesis

(Zimna & Kurpisz, 2015). The accumulation of HIF-1α triggers the production of pro-angiogenic factors, such as Vascular Endothelial Growth Factor (VEGF); this alters the balance of the angiogenic switch, allowing uncontrolled angiogenesis to occur (Jain, 2003; De Francesco et al., 2013; Zimna & Kurpisz, 2015). Alternatively, HIF-1α may also be produced independently from hypoxic areas by endothelial cells; accumulation of HIF-1α occurs following phosphorylation of profilin-1 at Tyr129, resulting in failed degradation of HIF-1α (Fan et al., 2014).

However, tumour vasculature produced as a result of neo-angiogenesis is highly irregular, resulting in vessels that leak, reducing the effectiveness of drug delivery (Zanotelli & Reinhart-King, 2018). Recent research has been undertaken to identify possible anti-angiogenic therapies, targeting the development of new blood vessels as the tumour progresses in order to restrict further growth (Stacker & Achen, 2013; Wang et al., 2017a; Schulte et al., 2021). Such therapies include those looking to target pro-angiogenic factors associated with hypoxia-driven angiogenesis, e.g., the VEGF pathway. One highly explored example is bevacizumab, which has been employed in some treatment regimens to target VEGF, in an attempt to reduce tumour growth; bevacizumab binds to VEGF, inhibiting its function (Estrada et al., 2019). However, although approved by the FDA in the USA, bevacizumab is not approved by the National Institute for Clinical Excellence (NICE) for use in the UK; studies show that bevacizumab does not significantly improve overall survival for patients, with additional side-effects reported (Diaz et al., 2017).

Hypoxia within the tumour has been linked to a poorer prognosis for those with the IDH wildtype of GBM, through mechanisms such as the suppression of immune cells, through interference with inhibitory receptors expressed by immune cells (Xiong et al., 2021). For example, the receptors, PDCD1 and TIGIT have been identified as being inhibited, repressing the immune cell capabilities of tumour associated macrophages (Xiong et al., 2021). As well as promoting treatment resistance, hypoxia further promotes aggressive tumour growth through enhanced tumour invasion within the brain due to the chaotic nature of the vasculature (Monteiro et al., 2017; Roy et al., 2020).

In addition to IDH wildtype, GBM commonly possesses other mutations, including, Epidermal growth factor receptor (EGFR) amplification, Telomerase reverse transcriptase (TERT) promotor mutation, and gross alterations to chromosome 7 (gain of material) and chromosome 10 (loss of material) (Brat et al., 2018; Stichel et al., 2018; Louis et al., 2021). A study by Stichel et al. (2018) demonstrated that in most cases, a combination of at least two of these key mutations were seen in IDH wildtype GBM; the presence of all three genetic alterations was only seen in GBM and was a poor prognostic factor.

1.1.4. Tumour Treatment

1.1.4.1. Treatment Methods Currently Employed

Despite continued research, there has been little in the way of progress in improving patient survival significantly over the last 2 decades. The current 'best practice', introduced following the Stupp protocol outlined in their 2005 publication, uses a combination of surgery, chemotherapy, and radiation for maximum effectiveness, with Temozolomide (TMZ) being the most effective chemotherapeutic agent seen (Stupp et al., 2005).

As a result of TMZ inclusion, patients were shown to survive 14.6 months on average, an increase of 2.5 months, compared to just radiotherapy treatment, as observed through clinical trials (Stupp et al., 2005). Further progress has been made in recent years by the Stupp group, in which the addition of Tumour-Treating Fields to TMZ-based treatment was able to further increase patient survival to 20.9 months, compared to 16 months for those subjected to a solely TMZ-based treatment (Stupp et al., 2017). Tumour-treating fields consist of applying low electric fields to areas of malignancy, which adversely affects the cell division of glioblastoma cells. However, minimal progress has been made overall towards the development of more effective treatment strategies.

Additional analysis into the advantages of TMZ inclusion has also been conducted by many, including the Witthayanuwat et al. (2018) group, who confirmed that patient survival increases when TMZ is used in addition to surgery and radiotherapy. Research has also been conducted using novel therapies in addition to TMZ inclusion, in an attempt to improve the current ‘best practice’. One such route has seen the development of OKlahoma Nitrone 007 (OKN-007), an anti-inflammatory molecule seen to aid in reducing cell proliferation (Towner et al., 2013). Use of OKN-007 has been shown to increase the effectiveness of TMZ and improve patient survival (Towner et al., 2019). Such studies are looking to not only reduce tumour growth, but to reduce instances of TMZ resistance that develop during treatment. A selection of recent experimental studies are briefly summarised in Table 1.1. The issues of TMZ (and chemo-resistance) are discussed further in Section 1.1.7.

Table 1.1. Selection of experimental studies for improved treatment of GBM.

Experimental study	Purpose of the study	Patients	Findings/ outcomes of the study
Wang et al. (2017b)	Analysed the effects of using cisplatin alongside TMZ to enhance the effects of TMZ by inhibiting the DNA repair enzyme, O6-methylguanine-DNA-methyltransferase (MGMT). It was observed that TMZ effectiveness is increased in cases of reduced MGMT function.	27 patients. Average age, 56 years.	Results of study are promising; however, there is a need for larger, randomised studies.
Kim et al. (2018)	To investigate the use of procarbazine and lomustine (CCNU) as a possible chemotherapeutic method for treating recurrent GBM. With the aim of treating the patient without including vincristine (PCV) as part of the treatment course, so as to reduce the side effects experienced by patients on PCV.	8 patients. Median age, 56.5 years.	Demonstrated that the use of procarbazine and CCNU used in combination was not suitable for the treatment of GBM, due to adverse effects.
Lesueur et al. (2019)	Ongoing clinical trial. Using the Stupp model as the basis for treatment, the study focuses on testing the addition of a radio-sensitising agent (Olaparib) to the current treatment method, in an	Plan for the enrolment of 79 patients.	N/A

	attempt to reduce instances of radio-resistance.		
Hanna et al. (2020)	To determine the effects and viability of the use of Olaparib on the patient.	48 patients. Median age, 51 years.	Olaparib was shown to successfully penetrate the tumour core. However, side effects of TMZ were exacerbated when used alongside Olaparib (intermittent dosing of Olaparib was required to reduce these effects). Models used to illustrate the effects of Olaparib required improvement.
Compter et al. (2021)	Analyse the benefits of chloroquine when used in combination with radiation and TMZ. With the aim of using chloroquine to target autophagy within the tumour and therefore reduce hypoxia within the malignancy. A benefit of the study includes the reduction of treatment resistance which may arise as a result of hypoxia.	13 patients. Median age, 58 years.	Although issues with toxicity were observed following the use of high doses of chloroquine, the use of other autophagy targeting drugs, which look to inhibit and reduce instances of tumour hypoxia, should be explored.

1.1.4.2. Surgical Issues

The invasiveness of GBM contributes to the difficulty experienced during surgical removal of the tumour, as its diffuse nature prevents complete removal, due to tumour cells invading surrounding areas of the brain (Wilson et al., 2014; DeCordova et al., 2020). The initial, primary tumour often spreads into the surrounding tissue, establishing a secondary tumour within the brain, seeding future GBM recurrence (Velásquez et al., 2019). Additionally, tumour location can restrict and prevent removal; GBM cells can often be found situated in key areas of the brain, such as those which control motor function, making it difficult to excise the malignancy (Davis, 2016). In these instances, maximal safe resection takes place, in which the greatest amount of tumour which can be removed is resected during microsurgery; it has been noted that the greater the proportion of tumour resected, the longer the patient is expected to survive following treatment, with overall survival increasing from 14.5 to 18.4 months with incomplete and complete surgery, respectively (Haj et al., 2017).

Several avenues of research have been conducted seeking to increase the percentage of tumour resected during surgery, including the introduction of MRI guided surgery (Senft et al., 2010). Maximal surgical resection, as well as a combination of radiotherapy and chemotherapy are employed for patients who can withstand these intense treatments. With the median age of diagnosis being 64 years of age, there are additional concerns regarding treatment for elderly patients with GBM (Ostrom et al., 2013). Due to the stresses of the aggressive treatment required, the potential benefits must outweigh the strain placed upon the patient for treatment to commence. For example, surgery will take place to remove the maximum amount of tumour, but additional therapies, such as chemotherapy and radiotherapy may not be employed; a study by Iwamoto et al. (2008) demonstrated that elderly patients were less likely to receive such treatments, and this was associated with poorer survival. Within the UK, a guide on the most appropriate treatment course for each patient is outlined by NICE (2018).

However, the patient, following a discussion with their clinical care team, may choose to opt out of any ‘curative’ treatment, and in this case, would receive palliative care. Research conducted into the benefits of continuing to offer treatment to elderly patients demonstrated a positive impact on patient survival (Gállego Pérez-Larraya & Delattre, 2012). For example, a study by Ewelt et al. (2011) demonstrated that the use of complete surgical removal on elderly patients, as opposed to taking a biopsy only, improved patient survival from 2.2 months to 13.9 months.

1.1.4.3. Reasons for Treatment Failure

Although it has been determined that a combination of therapies provides the greatest benefit in terms of patient survival, issues with adjuvant radiotherapy and chemotherapy treatments have been observed. Specifically, instances of treatment resistance have been frequently seen, as discussed later in Sections 1.1.6 and 1.1.7. Whilst most parts of the GBM tumour are sensitive to radiation and chemotherapy drugs, some parts of the tumour mass can develop treatment resistance (Qazi et al., 2017). These resistant, unaffected cells are then able to continue growing at their normal rate, advancing the progression of the tumour through recurrence. Such issues are attributed to the high levels of cellular heterogeneity seen within GBM, resulting in varying levels of treatment sensitivity within the tumour (Massey et al., 2020). Research has been undertaken in which a more patient specific approach was tested to try and account for GBM heterogeneity, through the use of drug sensitivity and treatment resistance testing on cell cultures produced from GBM patient samples. A study by Skaga et al. (2019), utilised biopsies taken from GBM patients to establish cell cultures, from which patterns of treatment resistance were identified, indicating the most effective drugs for each patient from which the biopsy was derived. The Skaga group have since furthered their investigation of TMZ treatment sensitivity using patient biopsies to establish Glioblastoma stem cells for high throughput testing of TMZ, confirming the clinical relevance of their model (Skaga et al., 2022). Crucially, this model was able to predict patient survival based on TMZ sensitivity, as well as showing the heterogenous nature of GBM with TMZ sensitivity. The more recent study by Skaga increased the patient cohort from 10 in the previous study, to 51 patients, enabling an improved investigation of GBM.

Despite extensive efforts using the Stupp method, even with complete/ maximal surgical removal (Figure 1.1), tumour recurrence is invariably observed, a problem compounded by therapy resistance (Rapp et al., 2017; Goenka et al., 2021).

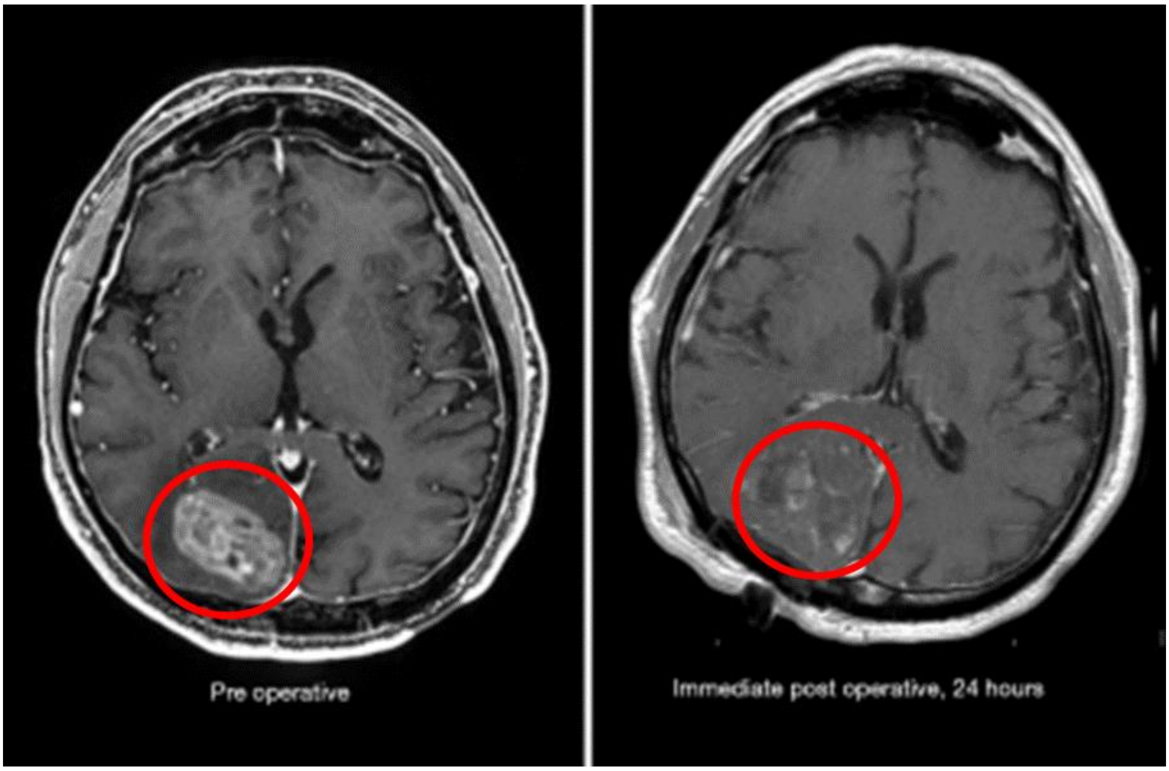

Figure 1.1. Magnetic Resonance Imaging (MRI) of a patient's brain pre- and post-operation (24 hours post-operation), in which maximal resection of GBM has occurred (Shukla et al., 2017). Tumour position highlighted in red on the MRI scan, pre- and post- surgery.

1.1.4.4. Future Treatments

Despite some minor improvements in treatments, alternative methods are being sought to improve patient survival and quality of life further, for those afflicted with this debilitating cancer. One route of research looks to explore epigenetic alteration as a therapeutic method. However, research is currently in the early stages, with the clinical benefits of epigenetic regulation of the tumour yet to be explored. Epigenetics and GBM will be discussed in depth in Section 1.2.

1.1.5. Heterogeneity

As stated above, much of the difficulty in treating GBM has been attributed to the high level of heterogeneity within the tumour; both inter- and intra-heterogeneity has been observed. Intra-tumoral heterogeneity is where the tumour has sub-populations of cells with different genetic mutations (Becker et al., 2021); with instances of spatial intra-tumoral heterogeneity commonly being observed (Lukas et al., 2019). Consequently, each of the sub-groups react differently to various treatments. Although some mutations promote a greater sensitivity to treatments, others lead to higher levels of resistance. For example, the EGFR mutation has been linked to enhanced treatment resistance; with varying levels of EGFR expression being present across distinct tumour subpopulations, leading to differing levels of treatment sensitivity within the tumour mass (Eskilsson et al., 2018). Previous work by Eskilsson highlighted the impact of the presence of EGFR mutations, with an increase in angiogenesis being a key contributor to tumour progression as a result (Eskilsson et al., 2016). Another crucial observation by Eskilsson et al. (2016) was the emergence of different EGFR mutations further along in the tumour development, demonstrating the ever-changing target for treatment.

The extent of cellular heterogeneity within GBM was explored by Patel et al. (2014) who utilised single-cell RNA sequencing to analyse GBM in the context of tumour heterogeneity, by isolating and sequencing full length transcriptomes obtained from cells from resected GBM tumour tissue. The group identified variability in the intertranscriptional relationships between the cells analysed, demonstrating variability across the cells, with multiple subtypes of cells present within each sample. A more recent study by Xiong et al. (2020) also utilised single-cell RNA sequencing data, obtained from the Gene Expression Omnibus (GEO) database, determining that the greatest heterogeneity observed in GBM patients is caused by inter-heterogeneity. This study focused on analysing the different cell subtypes present, as well as key features such as cell communication to determine levels of heterogeneity across 4019 cells which had been obtained from primary GBM patients exhibiting IDH (Xiong et al., 2020).

1.1.6. Radioresistance through Cancer Stem Cells

It has been observed than Cancer Stem Cells (CSC) play a role in regenerating the tumour following unsuccessful treatment attempts. These stem cells are able to regenerate damaged cells, promoting a fresh ‘wave’ of new tumour cells able to proliferate and grow. Bao et al. (2006) demonstrated that CSC show targeted activation of key features of the cell cycle, specifically the DNA damage response checkpoint. Through control of this response, in which damaged cells are arrested at the DNA damage response checkpoint, DNA repair of cells is encouraged; if this process becomes dysfunctional, CSC allow uncontrolled proliferation, producing cells with ‘damaged’ DNA. Additionally, Bao et al. (2006) showed that CSC can repair tumour cell DNA that has been damaged during radiotherapy treatment, renewing the cells affected by ionising radiation treatment and conferring radio-resistance. A recent study by Liu et al. (2020) confirmed the radioresistant properties of CSC in GBM, also showing that such stem cells are capable of conferring greater radioresistance in response to treatment through DNA damage repair; the control of the response was linked to greater CD44 expression by the malignant cells.

CD133 has been identified as being a key biomarker of CSC in gliomas, with its presence being linked to increased levels of tumorigenesis and promotion of cellular regrowth of tumour cells following radiotherapy and chemotherapy (Bao et al., 2006; Li, 2013; Barzegar Behrooz et al., 2019). Furthermore, it has been observed that CSC which possess the CD133 marker have a greater ability to prevent tumour cells from undergoing apoptosis (Angelastro & Lamé, 2010); a second hallmark of cancer. Preliminary investigations have taken place, targeting CD133 positive CSC in order to reduce the radio- and chemo-resistant tendencies of this cell population, with one study identifying the benefits of using CAR-T immunotherapy for this purpose (Vora et al., 2020).

1.1.7. Chemotherapy Drug Resistance

Treatment resistance has been observed in response to chemotherapy, aiding in continued tumour survival and proliferation (Wu et al., 2021). As with radioresistance, some forms of chemotherapy resistance have been attributed to areas of hypoxia (Haar et al., 2012; Doktorova et al., 2015; Zheng et al., 2021). Such resistance has been associated with the morphology of hypoxic regions, in which inadequate blood flow prevents the chemotherapy agent from gaining access to malignant cells in these parts of the tumour mass. Instances of abnormal vasculature have also been linked to chemoresistance through mediation of endothelial cell plasticity which drives the production of irregular blood vessels (Huang et al., 2016). In addition to issues of drug delivery, other studies have identified key markers, which when controlled/ inhibited by hypoxic regions, can result in increased levels of chemoresistance. For example, in GBM, the microRNA miR-137, thought to act as a tumour suppressor, has been seen to be inhibited as a result of hypoxia and consequently results in reduced sensitivity to chemotherapy, specifically in response to TMZ (Li et al., 2020). Additionally, it has been noted that hypoxia within the tumour can trigger the development and production of CSC within the tumour (Ahir et al., 2020), leading to the problems highlighted in Section 1.1.6, in particular instances of radioresistance.

Consequently, hypoxia poses a major challenge when treating GBM as it not only promotes chemoresistance, but also encourages re-growth of the tumour following treatment. Examples of chemoresistance which have been observed include that of GBM resistance to the anti-angiogenic treatment, bevacizumab. The use of bevacizumab to treat GBM is limited, with studies outlining no significant improvement in overall patient survival when used in conjunction with the standard method of treatment (Chinot et al., 2014; Gilbert et al., 2014). A further look at the possible reasons for the chemoresistance observed following bevacizumab use, demonstrated possible links with hypoxia. One such study outlined the interplay between hypoxia inducible protein 2 (HIG2) and HIF-1α, demonstrating that when HIG2 expression is elevated, as induced by bevacizumab treatment, expression of HIF-1α is also increased, in turn leading to increased levels of VEGF and consequential pro-angiogenesis (Mao et al., 2016). The cause of resistance to bevacizumab was also explored by Carvalho et al. (2021) who analysed the effects of bevacizumab on 40 patients. This study identified c-Met and VEGFR2 as having a negative impact on tumour progression following bevacizumab treatment, with overexpression of these factors linked to reduced time before tumour progression takes place. As such, the impact of tumour heterogeneity is further highlighted.

Alternative routes of research have been conducted, in which the abnormal vasculature within tumours was targeted in an attempt to reduce the effects of an insufficient blood supply on chemoresistance during cancer treatment (Shen et al., 2019). Thalidomide was seen to increase the ‘normal’ vasculature in murine models of breast and colorectal cancer, allowing improved delivery of the chemotherapeutic agent, improving effectiveness, and aiding in the suppression of tumour growth;

achieved through control of pro- and anti- angiogenic factors (Shen et al., 2019). A recent meta-analysis demonstrated that GBM patients treated with Thalidomide showed no major treatment benefits, compared to those treated with bevacizumab (Wang et al., 2016). As such, hypoxia remains a problem during GBM treatment.

Most notably are issues of chemoresistance in relation to TMZ use. Despite being the current preferred chemotherapy drug, several instances of chemoresistance have been identified, reducing the effectiveness of this treatment (Shi et al., 2017). As such, the mechanisms by which this resistance occurs are being analysed in order to find possible therapeutic targets and diagnostic markers to reduce instances of chemoresistance when TMZ is employed. Such as, the use of the agent OKN-007 in conjunction with TMZ, as mentioned in Section 1.1.4.1, which was seen to provide increased sensitivity to otherwise TMZ-resistant tumours (Towner et al., 2019). Alternative routes of research have looked to identify markers which increase instances of chemoresistance when overexpressed, such as long-coding RNA SBF2 antisense RNA 1 and the circular RNA, ASAP1; such markers could be used as prognostic markers and targets for therapy during treatment (Zhang et al., 2019; Wei et al., 2021).

1.1.8. Tumour Models

1.1.8.1. 2D Cell Culture Models

To investigate GBM, as with any malignancy, appropriate tumour models are needed. Cell culture methods are chosen for their ability to provide a mechanism for which cell biology can be observed, studying the interaction between cells with and without treatment. Through these mechanisms, testing of new therapeutic methods on tumour cells can be performed and observed. In this investigation, established cell lines were utilised. Using human GBM cell lines, 2D and 3D culture methods can be performed through the continued maintenance of cells. The use of 2D cell culture has become prevalent in the initial stages of cancer research, with cells being used in the identification of new and innovative treatment methods, as well as the testing of new drugs (Edmondson et al., 2014; Du et al., 2018).

2D cell culture models provide an easily reproducible system for modelling a basic representation of the tumour, through the use of long-established cell lines. The use of cell lines is a relatively inexpensive modelling method, requiring minimal maintenance to sustain consistent cell growth, allowing for experiments to be repeated with little variability between cell samples (Kapałczyńska et al., 2018; Brüningk et al., 2020). Cell lines can be purchased and maintained for several years by periodically freezing down cells at a low passage number for storage in liquid nitrogen. Additionally, minimal equipment is required for 2D model maintenance, whereas 3D models or indeed microfluidic devices require many more components, such as specialist flasks or syringe pumps for example. 2D cell cultures use cell lines established from patient-derived tumours and can be maintained and grown for several weeks as a monolayer of cells in a sterile flask on treated tissue culture flasks or plates, usually being incubated at 37˚C in an environment of air with 5% CO_2, with little cell-cell interaction (Li & Cui, 2014; Liu & Chen, 2018; Brüningk et al., 2020). Due to their relatively low purchase and maintenance costs, cell lines provide a good starting point for initial tests on new therapeutic methods. Following 2D analysis, further tests usually now progress to 3D cell culture methods, which better model the patient's tumour *in vivo*.

However, all models have their limitations, the most prominent of any 2D model is its inability to mimic the TME correctly, due to the omission of key features, such as the Extracellular Matrix (ECM), characteristics of which profoundly affect the response of cells to stimuli, including that of therapeutic procedures (Bahcecioglu et al., 2020). Within a patient's tumour, multiple and varying cell types are seen, creating a unique TME in which the cells interact with one another as well as the ECM. It is within the tumour mass that these interactions alter factors such as cell proliferation, gene expression, tumour progression, and sensitivity to treatment. Specifically, the ECM is responsible for the control of migration and invasion of glioma cells during tumour progression, with proteins such as proteoglycans primarily responsible for regulating the movement of cells across the ECM (So et al., 2021). The TME of GBM consists of a vast array of components, including astrocytes, neurons, CSC, hypoxic regions, as well as the BBB, which together control features such as tumour growth, angiogenesis, evasion of the immune system, as well as tumour invasion (Bar, 2011; Tomaszewski et al., 2019). With the lack of ECM as well as the fact that the majority of 2D models comprise a single cell type, such models are unable to provide an accurate assessment of tumour response to treatment, and so cannot be solely relied upon.

Although 2D culture models are still currently used during early stages of drug development it is well-established that results gained often do not translate to effective drug treatment, as seen during clinical trials (Edmondson et al., 2014; Wong et al., 2019). Therefore, the move towards more widespread use of 3D cultures is taking place. It has been noted, in a study of colorectal cancer cell lines, that 2D and 3D models react differently to radiotherapy and chemotherapy, with 3D models offering more resistance, reflective of an *in vivo* response (Koch et al., 2021). Due to the high prevalence of resistance observed in GBM, the use of 3D models may elicit a more accurate response to treatment and extensive work is being undertaken to develop and test these systems (Brancato et al., 2020).

1.1.8.2. 3D Cell Culture Models

As outlined above, there is a transition from 2D to 3D models, due to the clinical benefits observed during cancer drug and treatment development (Bahcecioglu et al., 2020; Fitzgerald et al., 2020; Jensen & Teng, 2020; Van Zundert et al., 2020). One factor that 3D cell models can begin to model is the spatial aspect of the TME. 3D models have been able to demonstrate improved cell-cell interactions, as well as cell interaction with the ECM, compared to a 2D system (Aihara et al., 2016; Neufeld et al., 2021). The inclusion of these factors is crucial when developing new therapeutic techniques and testing new cancer drugs as this will improve the success rate seen when progressing from initial 2D and 3D models to clinical trials (Edmondson et al., 2014). Successful translation of pre-clinical to clinical drug trial success has been observed to be as low as 5% for anti-cancer therapeutics, indicating a need for improved tumour models during pre-clinical testing (Hutchinson & Kirk, 2011; Malakpour-Permlid & Oredsson, 2021).

Multiple 3D models have been developed using many different technologies and approaches; spheroids and organoids are some of the most common, both of which are capable of improving the interaction seen between cells when communicating *in vivo* (Chitturi Suryaprakash et al., 2020; Doctor et al., 2020; Huang et al., 2020). Spheroids are as described, a spherical mass which can be encouraged to form from cells in a ball-like structure, from either one cell line or a combination of cell types. Whereas organoids are a more complex 3D structure, formed from cells or tissue (or both), capable of replicating the cellular process of the tissue, for a more accurate model. However, organoids require more components in order to promote cell-cell signalling and organoid growth, for example, the use of an ECM (Rossi et al., 2018).

For example, recent research has seen the development of models such as cerebral organoids; this model utilises glioma stem cells alongside cerebral organoids to encourage the development of patient-derived tumours within the organoid mass for use as a drug screening model (Linkous et al., 2019). 3D models can be broadly separated into scaffold-based and scaffold-free systems, which can be produced using various techniques (Doctor et al., 2020). Commonly used models for scaffold-free spheroids utilise Ultra Low Adhesion (ULA) plates (example seen in Figure 1.2.A), the hanging drop method, as well as continuous agitation techniques in which the cells are prevented from adhering to the surface of the plates used (Foty, 2011; Santo et al., 2016; Ryu et al., 2019; Franchi-Mendes et al., 2021; Luo et al., 2021; Javed et al., 2022).

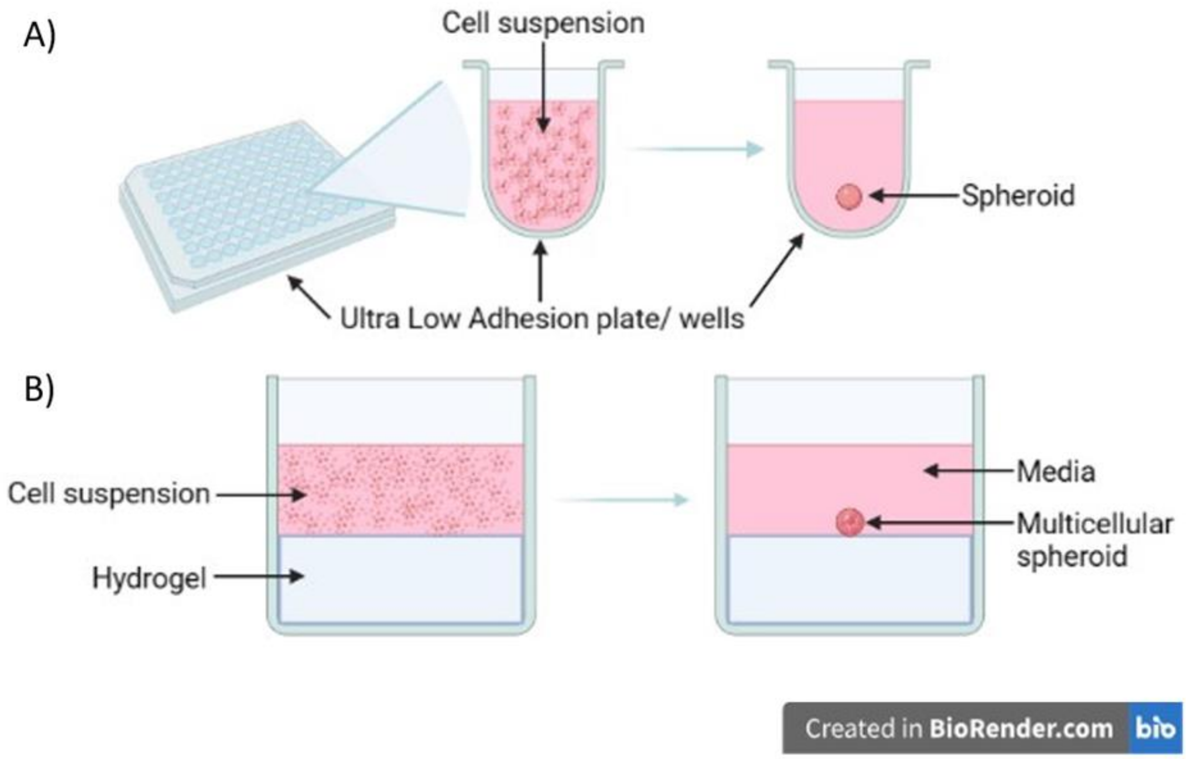

Figure 1.2. Examples of 3D models. A) Production of spheroids using Ultra-Low Adhesion plates – a scaffold-free method. B) The use of a hydrogel matrix to act as a framework to encourage the formation of spheroids – a scaffold-based method. Figure produced using BioRender.

Alternatively, scaffold-based models may be used, including hydrogels, organoids, and bio-printed models (Krieger et al., 2020; Paolillo et al., 2021; Unnikrishnan et al., 2021). A key feature of scaffold-based systems, as the name suggests, is the inclusion of a frame around which an ECM-like structure can form. It is hypothesised that this improves the mimicking of the TME, compared with structure-less methods, allowing features such as hypoxic regions to be generated (Unnikrishnan et al., 2021; Valdoz et al., 2021). For example, hydrogels can be employed to act as a scaffold when producing multicellular spheroids (example shown in Figure 1.2.B), providing a 3D external ECM framework for improved cell-cell interactions. Multicellular spheroids also better mimic the TME, as heterogenous areas can develop (Nath & Devi, 2016).

A recent study by Bruns et al. (2022) demonstrated the use of spheroids held in hydrogels to analyse the effects of TMZ on GBM cell lines, by maintaining the spheroids in culture for 7 days. For this investigation, the aim was to study altering the stiffness of the hydrogels to mimic the various structures of the brain, and thereby observing any effects this had on spheroid response to TMZ, by measuring cell viability and invasion (Bruns et al., 2022). It was observed that hydrogel stiffness did affect TMZ penetration into the spheroids, with TMZ affecting cell viability to a greater degree in the spheroid core in the softer gels, suggesting that tumour composition, such as the stiffness of the ECM, may impact treatment effectiveness. Alternative methods, such as electrospinning have been utilised to produce an ECM-like scaffold in order to replicate the GBM structure (Unal et al., 2020). Within this study, electrospinning was used to form scaffolds with nanofibers, with models demonstrating enhanced cell adhesion and communication.

The TME is particularly difficult to replicate due to several key features, namely, the heterogenous nature of tumours, with multiple cell populations present within a tumour mass; substantial heterogeneity is also observed between the tumours of different GBM patients. The morphology of the tumour also poses a problem as the core frequently becomes necrotic due to areas of low oxygen (Bahcecioglu et al., 2020). Similarly, as with areas of low oxygen, there are also areas of low nutrient supply within the tumour (Bahcecioglu et al., 2020). Although 2D cells grow effectively in a monolayer formation on a flask, this is not representative of the TME, due to the constant access to media, which provides the nutrients required of the cells, as well as a limitless oxygen supply, thus allowing for undisturbed growth (Brüningk et al., 2020; Atat et al., 2022). However, the nature of spheroids allows for the production of a necrotic core as the spheroid forms and grows, enabling hypoxia to be represented; it has been observed that tumour spheroids develop the oxygen and nutrient gradients seen within the TME (Hirschhaeuser et al., 2010; Brüningk et al., 2020). As such, the spheroid model provides a more accurate representation of how the tumour would react *in vivo* to the treatments employed, including issues of treatment resistance which are often seen with GBM (Nunes et al., 2019).

As they develop, spheroids produce layers which give rise to the varying gradients observed; a hypoxic and necrotic core, followed by a layer of viable but quiescent (inactive) cells, and finally surrounded by an outer layer of proliferating cells which remains in contact with the media (Nath & Devi, 2016). Crucially, this layer of proliferating cells provides an opportunity to observe the effects of treatment on spheroid growth. This 3D structure better mimics the TME which can be seen *in vivo*, with areas of necrosis, as a result of metabolic waste build-up and poor vasculature, with proliferation seen throughout the tumour (Kim, 2005; Nath & Devi, 2016). The inclusion of hypoxic regions within the spheroids provides the opportunity to study the chemoresistance observed during treatment which occurs due to the presence of hypoxic regions (Doktorova et al., 2015; Ma et al., 2021b). The hypoxic regions present within spheroids are illustrated in Figure 1.3, which shows the necrotic centre of spheroids, surrounded by the layer of live, proliferating cells, as indicated by live-dead staining. The introduction of cellular heterogeneity is more representative of the *in vivo* environment, particularly the intra-tumoral variations observed in relation to sensitivity to treatment methods which often affects treatment success.

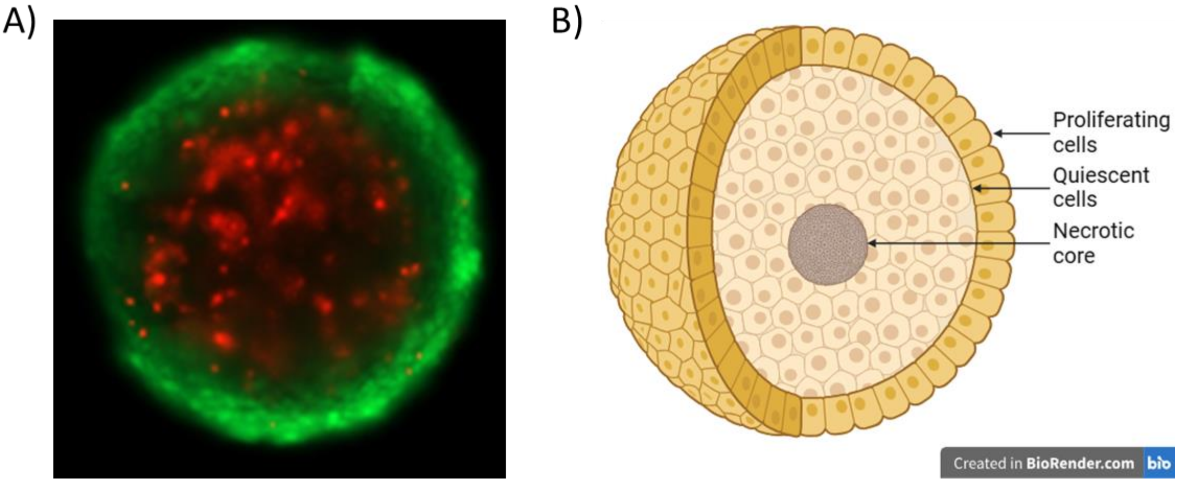

Figure 1.3. Example image of a spheroid. A) Live-dead stain of a spheroid. Following incubation with fluorescein diacetate (FDA), which stains live cells green, and propidium iodide (PI), which stains dead cells red (Sennett, 2019). B) Diagrammatic representation of a spheroid. The different layers of the spheroid are highlighted. Figure 1.3.B. produced using BioRender.

1.1.8.3. Xenograft Model

Alternative tumour models include xenografts, in which either tumour cells or patient-derived tumour tissue are implanted into immunocompromised specimens and allowed to grow (Richmond & Su, 2008). Following tumour growth, analysis can be performed; the tumour's reaction to treatment can be observed as it would react *in* *vivo* within the patient, enabling the effectiveness of various drugs, including drug delivery, to be observed. This is primarily due to the model including mouse vasculature surrounding the tumour, which greatly effects the effectiveness/ delivery of drugs administered, thus providing a more accurate representation of the TME.

Often, mice are chosen in this instance due to some physiological similarities seen between mice and humans. There are a number of autologous mouse models. Such as Genetically Engineered Mice (GEM), a well-established model which utilises a mouse tumour, rather than an implanted GBM tumour. Despite several limitations of GEM, including reproducibility and therefore variability between mice, such models do have a fully intact immune system (Fomchenko & Holland, 2006; Sahu et al., 2022); the tumours are encouraged to grow within GEM, which are then targeted by the mouse's own immune system, alongside any additional treatment methods being tested. For xenografts, it is crucial that immunocompromised mice are selected for use, as this will allow for the xenograft model to develop without the murine immune system rejecting the foreign tumour cells (Morton & Houghton, 2007; Okada et al., 2019). However, the immunocompromised nature of this mouse model may negatively impact the results, due to the removal of an effective immune response; thus, the TME response is not truly reflective of tumour presence/ growth.

Whilst often seen as subcutaneous xenograft mouse models, an intracranial xenograft mouse model has been used in a similar study to demonstrate the effects of altering CBX2 expression on tumour growth (Wang et al., 2021). This group utilised a mouse model to house U87 cells which had undergone CBX2 knockdown, observing a reduction in tumour growth. Other examples of the use of xenograft models in GBM include that of a study by Zhang et al. (2021) which focussed on the analysis of pericytes and their possible effects on chemoresistance in GBM patient-derived xenografts following TMZ administration, through the DNA damage repair mechanism.

A key factor in the use of animal models is the need for ethical approval to be sought prior to research taking place, however this can also be said for the use of primary human cells. Despite this, subcutaneous xenograft mouse models are considered an excellent tool in drug development.

1.1.8.4. Development of Microfluidic Devices

In recent years, research has been directed towards the development of microfluidic devices able to hold resected tumour tissue *ex vivo*, in an *in vivo* like environment (Cheah et al., 2010; Bower et al., 2017; Riley et al., 2019; Olubajo et al., 2020). Some examples of devices are shown in Figure 1.4. As such, tumour tissue can be analysed whilst being subjected to various treatments, including chemotherapy and radiotherapy, the aim usually being to find the most effective drug, drug combinations, or radiation dose (Hattersley et al., 2012; Carr et al., 2014; Cheah et al., 2017; Kennedy et al., 2019). The ability to test resected tumour tissue provides an important step towards a personalised and time-sensitive model capable of identifying the best treatment course for each patient. In addition to this, analysis has been conducted in determining the ability of microfluidic devices to move towards improving the replication/ representation of tumour heterogeneity *ex vivo*, with Head and Neck Squamous cell carcinomas and GBM tumours being investigated in this context (Kennedy et al., 2019; Olubajo et al., 2020). Kennedy et al. (2019) demonstrated that radiotherapy treatment could be applied to resected tumour tissue, maintained on a microfluidic device for 68 hours, and was able to reduce cell proliferation. Whilst Olubajo et al. (2020) maintained resected GBM tissue on chip for 72 hours, showing through analysis of biomarkers and tissue morphology that cell viability was successfully maintained on chip.

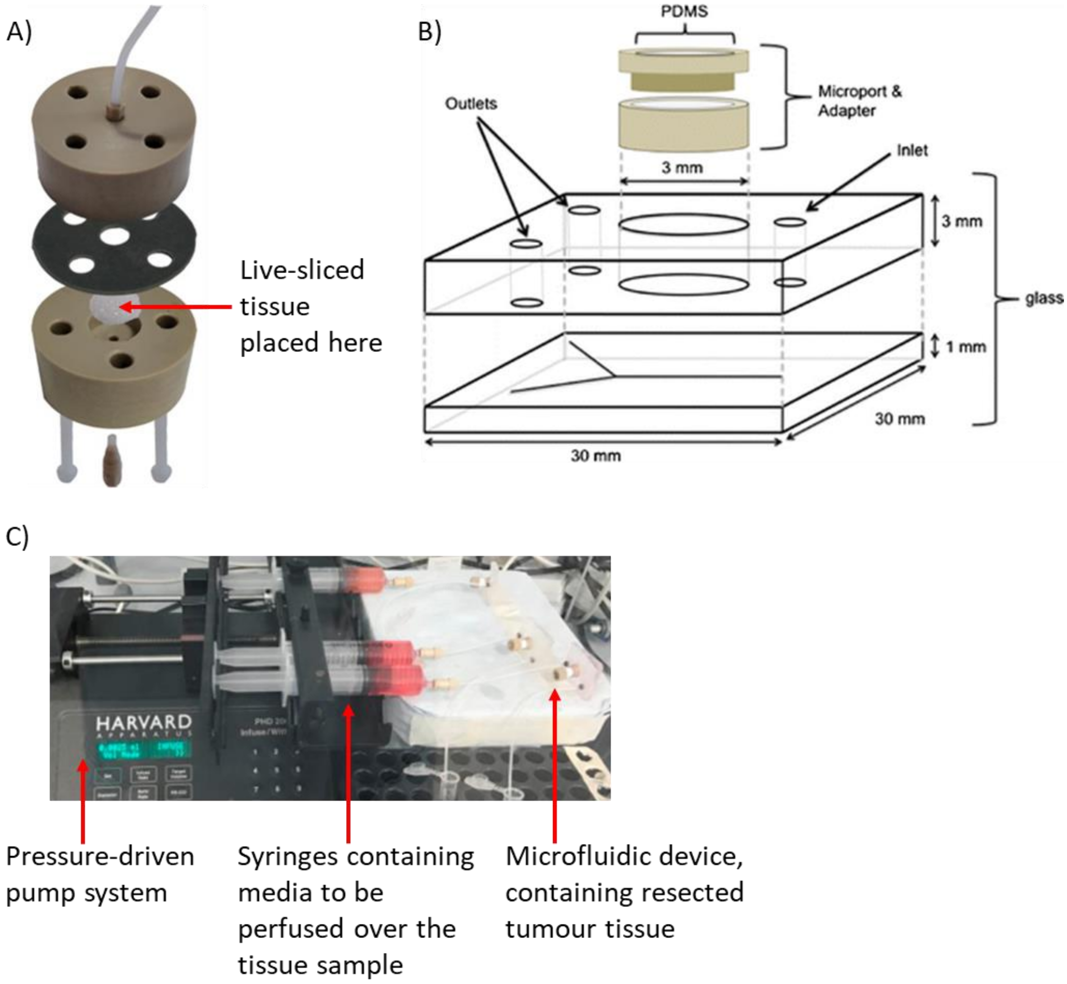

Live-sliced tissue placed here

Pressure-driven pump system

Syringes containing media to be perfused over the tissue sample

Microfluidic device, containing resected tumour tissue

Figure 1.4. Examples of microfluidic devices which used tissue biopsies. A) Microfluidic device designed to hold live-sliced tissue in place, with inlet and outlet tubes for media perfusion (Riley et al., 2019). B) Microfluidic device for the maintenance of resected tumour tissue which is held within the central chamber (3mm central column) (Hattersley et al., 2011). C) Example of a microfluidic set-up with pump system used to perfuse media over tissue held within a microfluidic chip (Olubajo et al., 2020).

A key feature of most/ all microfluidic devices containing tissue, is that of continuous perfusion which enables a constant flow of media to be supplied to the cells/ tissue held within the chamber of the chip (Hung et al., 2005; Kimura et al., 2008; Tanweer et al., 2013). Whilst a constant flow of fresh media is supplied, the waste materials and media produced are also removed to prevent a build-up. The effluent produced can also be used to monitor the tissue responses. By collecting the effluent periodically, such as every 24 hours, the viability of the cells can be analysed/ tested for using viability and cell death assays throughout the tissue maintenance period within the device. Through collection of effluent, the use of microfluidic devices has shown to be able to maintain cell viability and prevent cell death over periods of 4-12 days.

Several analytical methods such as Lactate Dehydrogenase (LDH) and Annexin V (AV) have been used to determine cell viability and cell apoptosis, respectively (Riley et al., 2019; Olubajo et al., 2020). Further apoptotic markers used include Cytochrome C, which is released from cells undergoing apoptosis and can therefore be used to observe levels of cell death during maintenance as well as after treatment (Hattersley et al., 2012; Carr et al., 2014; Rana et al., 2022). Once the maintenance period is complete, the tissue itself can be analysed using trypan blue to determine cell viability of the tissue (Riley et al., 2019). Additional tests include cell staining using Propidium Iodide (PI) to quantify cell death (Bahmani et al., 2011; Bower et al., 2017). Such assays are useful tools for analysing the effectiveness of the microfluidic device in maintaining cell viability, as well as the efficacy of chemotherapy agents and radiotherapy on tumour tissue.

Microfluidic devices can also be used to hold spheroids-on-a-chip, allowing for a dynamic 3D model (Petreus et al., 2021) enabling research to be conducted prior to working with tumour tissue. Spheroids-on-a-chip can also be utilised as a hypoxia model by combining the characteristics of spheroids along with enhanced replication of the TME through microfluidics (Refet-Mollof et al., 2021). Within this field, groups have looked to develop different chip designs for microfluidic devices. By reconfiguring the central chip chamber and overall design, the chip can be used to hold spheroids and/ or resected tumour tissue, or indeed act as the model for whole organs, maintaining samples *ex vivo*, in an *in vivo* environment. For example, lung-on-a-chip models have been designed to replicate the organ to replicate the *in vivo* response to treatment; as modelled by one example shown in Figure 1.5 (Zhang et al., 2018; Shrestha et al., 2020). The use of organ-on-a-chip models can be used as part of drug development during the pre-clinical research stage (Kimura et al., 2018; Ma et al., 2021a).

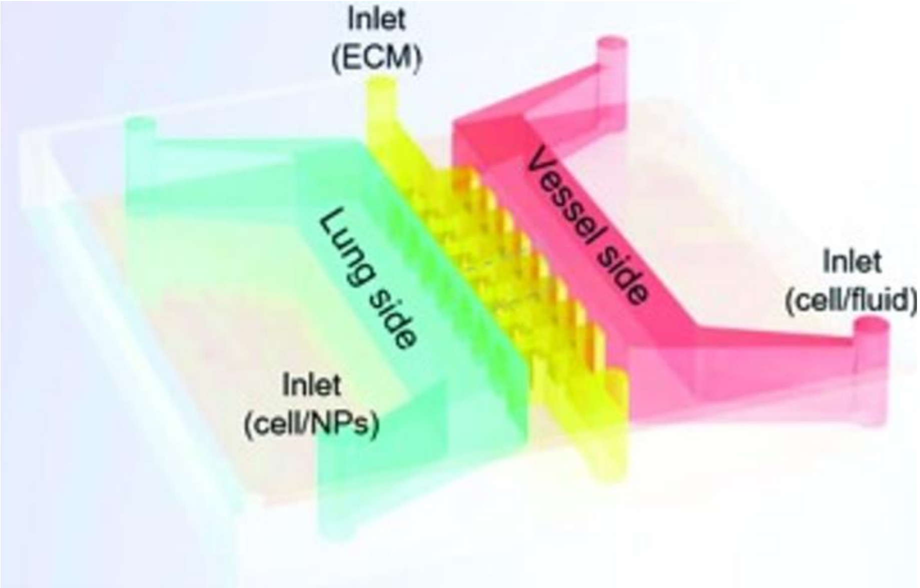

Figure 1.5. Example of lung-on-a-chip model. Three channels are used to mimic the in vivo TME; namely, the relationship between alveoli and capillaries within the lung (Zhang et al., 2018). NP = Nanoparticles.

Although microfluidic devices capable of holding patient tissue are widely considered to be the gold standard tumour model, there is a limit to the amount of tumour tissue that can be resected. Additionally, in many cases insufficient material would be available for the study, thus preliminary investigations would commonly use 3D models to provide both basic static and dynamic conditions. When sufficient tumour tissue is available, the tissue can be maintained within a microfluidic device as either lump tissue, typically around 10mg, or as tissue slices, sliced at 350µm thickness and cut using a biopsy punch at 5mm diameter (Riley et al., 2019; Olubajo et al., 2020). Slice tissue is generally preferred where possible as this provides a more reproducible and consistent method, as well as providing a cross-section of the tumour sample.

Various brain cancer chips have been developed by several groups, using different types of microfluidic devices to maintain patient derived cells for testing and observation *ex vivo*. Akay et al. (2018) collected tumour tissue from GBM patients and dissociated the sample, after which, the cells were loaded into the microfluidic chip and maintained whilst being subjected to TMZ and bevacizumab. Previously, this group used the same microfluidic chip with GBM cell lines for the purpose of drug screening; crucially the chip design used was capable of allowing multiple channels of different drugs and drug concentrations to flow over the cell model encased within the chip (Figure 1.6) (Fan et al., 2016). When maintained successfully, these cells could be analysed post-treatment to measure the response to the drugs used. An example of another microfluidic device developed as part of GBM treatment research, includes that of a microfluidic chip able to house a collagen hydrogel embedded with cells within its central chamber, with a focus on replicating pseudopalisade formation (a key histopathological feature of GBM) (Ayuso et al., 2017) so as to observe their effect on varying levels of nutrients and oxygen seen within tumours, and therefore the effect on tumour progression.

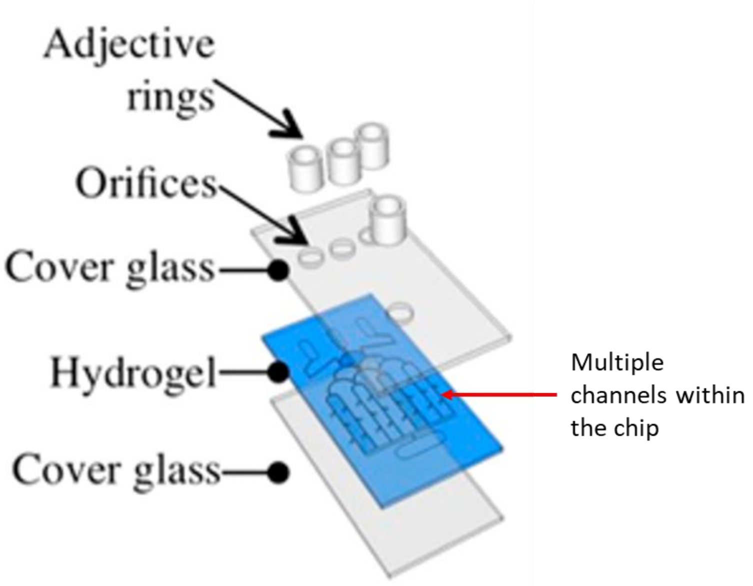

Figure 1.6. Multichannel microfluidic chip for testing multiple drugs simultaneously on GBM cells. The GBM cells used are encouraged to form spheroids on the chip (using hydrogel). The hydrogel layer contains the multiple channels within the chip, through which the different drugs can flow over the spheroids held in place (Fan et al., 2016).

Further applications of microfluidic chip use have seen the addition of tumour characteristics to the microfluidic devices in order to improve the TME representation, including that of the BBB (Xu et al., 2016; Wang et al., 2017c). Such microfluidic models look to represent the effects of the BBB on tumour sensitivity, as the BBB has shown to have a significant effect on whether various treatments can access the tumour (Shergalis et al., 2018). This is due to the regulatory properties of the BBB, controlling the exchange of substances across the barrier, between the blood and the brain (Wang et al., 2017c). As such, drug delivery and therefore effectiveness may be analysed with greater accuracy if the BBB can be incorporated into the model, as demonstrated by Campisi et al. (2018) who created a vascular network capable of testing the efficacy of drug delivery *in vitro*. A further factor that needs to be considered is the effect of shear stress, the force applied to the sample held within the device. As such, an ‘ultimate’ microfluidic model for GBM would comprise a BBB and the ability to measure and alter shear stress (Chen et al., 2021); two features usually missing in static models. Shear stress can affect the viability of the tissue within, as well as the required flow rate of media perfused over the sample.

1.2. CBX2

Due to the complexity of GBM and the subsequent difficulty in its treatment, alternative treatment options are being sought, including that of epigenetic targeting. Epigenetic factors have the ability to promote or suppress tumour progression. By targeting epigenetic modifications to stop them from promoting tumour progression, or indeed increase their suppressive effects, tumour development may be reduced, aiding traditional treatment methods.

1.2.1. Epigenetics

Epigenetics is the control of gene expression through alterations which do not change the fundamental DNA sequence. Gene expression alteration may occur through histone modification, DNA methylation, or through non-coding RNA (Audia & Campbell, 2016).

The DNA nucleosome core is comprised of 147 base pairs (bp) of DNA, which wrap around an octamer of histone proteins; this octamer is made up of two of each of four histones, H2A, H2B, H3, and H4 (MacAlpine & Almouzni, 2013) (Figure 1.7). Histones provide the structure of chromatin; chromatin is comprised of a mixture of DNA and proteins which in turn makes up the structure of chromosomes found within cells. Through chemical modification of the amino acid tails that make up histone proteins, DNA transcription can be controlled through the switching of chromatin between the heterochromatin and euchromatin states (Figure 1.8). When in the heterochromatin form, DNA is transcriptionally inactive due to the tight coil formation of the chromatin, in which the transcription machinery, including RNase Polymerase II, cannot get access to the promoter regions of the DNA (Li et al., 2007; Morrison & Thakur, 2021). Conversely, when in the euchromatin form, chromatin is loosely packed so that the promotor is accessible, enabling the transcription of genes (active state) (Li et al., 2007; Morrison & Thakur, 2021). As such, gene expression can be controlled by the active state of chromatin, with gene expression being activated when euchromatin is present and silenced/ inactivated when chromatin is in the heterochromatin state.

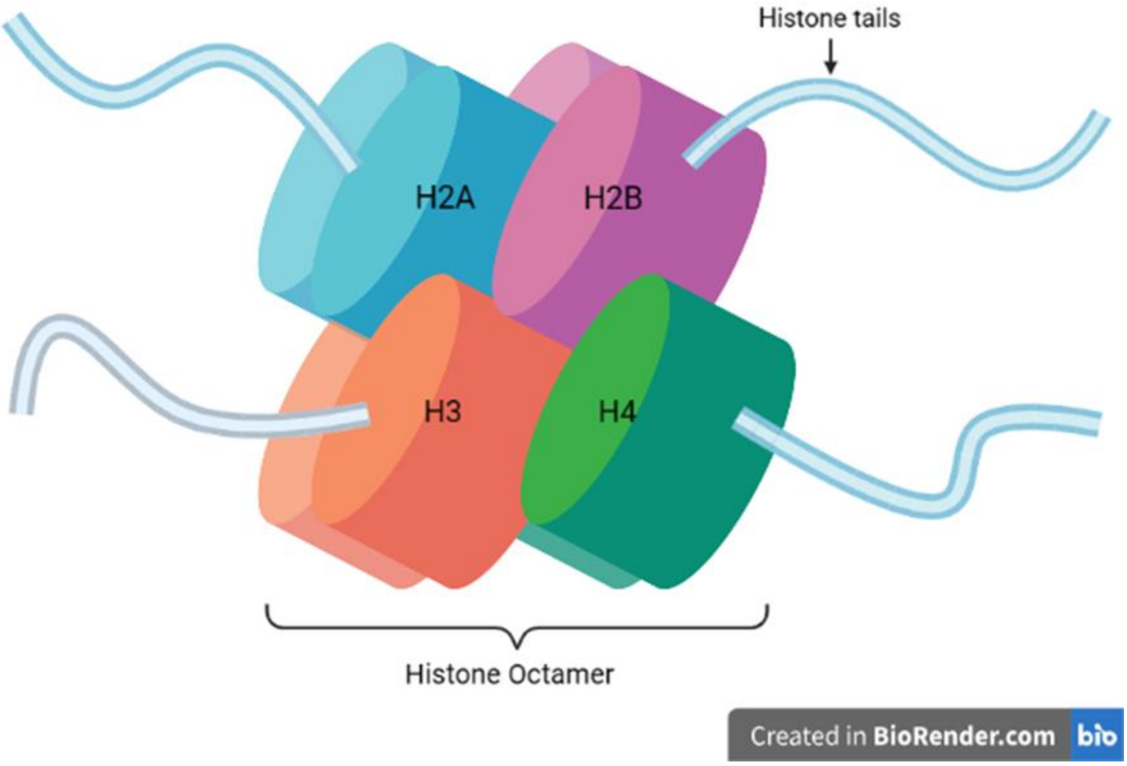

Figure 1.7. The histone octamer core. Containing two copies of each of the following molecules: H2A, H2B, H3 and H4. Amino acid tails protrude from the core histones. The histone tails are rich in lysine (K) and arginine (R). Figure produced using BioRender.

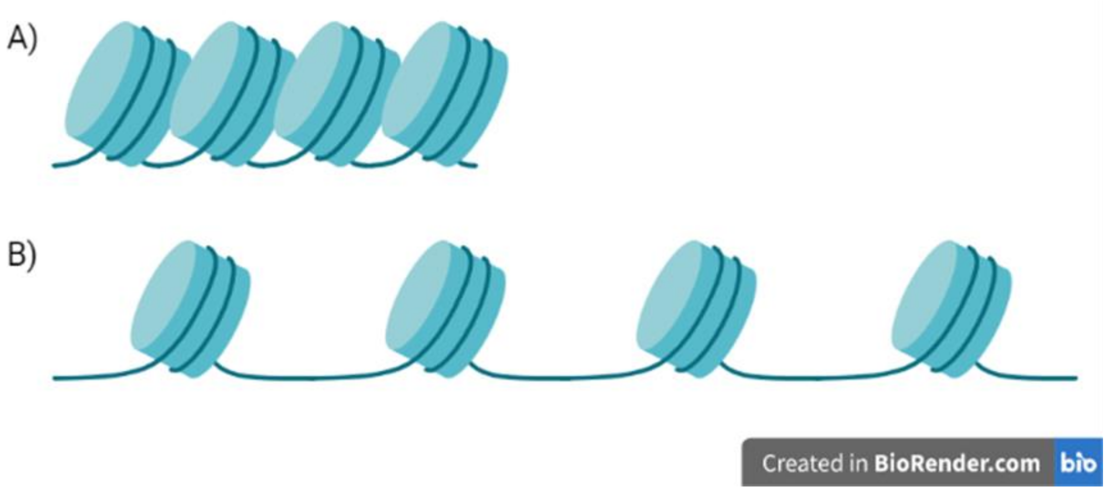

Figure 1.8. Chromatin structure. A) Chromatin in the transcriptionally inactive, heterochromatin state – closed structure. B) Chromatin in the transcriptionally active, euchromatin state – open structure. Figure produced using BioRender.

It is through these histone complexes that histone modification can occur, as the amino acid tails which are joined to the inner histone core of the histone protein (Figure 1.7), can be altered through the addition or removal of certain chemical moieties, including acetyl, methyl, and phosphate groups. Post-translational modifications (PTM) are most frequently seen on the N-terminal of the histone tails, with the protruding amino acid tails consisting primarily of lysine (K) and arginine (R), with serine (S) and Threonine (T) also present (Sidoli & Garcia, 2017). Referred to as acetylation, methylation, and phosphorylation (removal of groups denoted using 'de-' as a prefix to each of these), alteration of the amino acids of the N-terminal tails through these PTM can be used to control the active state of chromatin (Gan et al., 2015).

Another key PTM is that of ubiquitination, during which ubiquitin is added to the histone, facilitated by E3 ligase, often seen in relation to the H2A histone (Barbour et al., 2020); ubiquitination of H2A (H2Aub) is linked to oncogenic effects, through gene silencing (Zhang et al., 2017). The addition of the methyl group may be seen as mono-, di-, or tri-, in which one, two, or three groups are added, the presence of each are often linked to different functions (Zhang et al., 2013). However, depending on which amino acid is methylated, the gene affected may vary. Typically, methylation is associated with gene silencing. For example, silencing of the LHX6 gene is induced by methylation within pancreatic cancer, promoting tumour growth (Abudurexiti et al., 2020).

Key chromatin enzymes are utilised to facilitate PTM changes, which are known as writer, reader, and eraser proteins (Biswas & Rao, 2018). As the name suggests, the writer proteins are capable of adding PTM to the amino acid tails, whereas the eraser proteins remove them. Reader proteins are used to identify key PTM present within the amino acid tails, so that such modifications can be used to cause either activation or silencing of gene expression. It has been noted that a combination of these proteins, or indeed those which hold both writer and reader abilities are used to regulate and maintain the chromatin status, and therefore can control the active state of the chromatin through PTM (Zhang et al., 2015). As such, these tails may become targets for modifications in order to alter the transcriptional activity of the histone, which controls specific genes.

In cancer, the properties of histone modification are utilised in order to promote tumour growth and progression. During ‘normal’ practices, both heterochromatin and euchromatin are seen naturally within cells, promoting gene silencing and gene activation where required. However, in cancer, the levels of heterochromatin and euchromatin are altered to enable tumour progression, by switching on factors which drive cancer growth and switching off tumour suppressors; both chromatin states are used to maximise tumour development. Specifically, cell growth and survival genes are seen to be transcriptionally active and in their euchromatin state, whereas it is thought that tumour suppressor genes are in their heterochromatin state and are therefore transcriptionally inactive and ‘switched off’, due to gene silencing through epigenetic regulation (Yu et al., 2008).

There is evidence of histone modifications being altered in different cancer types, with studies focussing on key modifications which have been linked to cancer progression. For example, H3K9 methylation was shown to increase treatment resistance in prostate cancer (Baratchian et al., 2022). Other histone modifications linked to cancer include an increase in levels of H3K20me3 (tri-methylation of H3 at Lysine 20), which is associated with bladder cancer; this may serve as a prognostic marker for patients, with elevated levels of H3K20me3 associated with a poorer prognosis (Schneider et al., 2011).

Crucially however, epigenetic alteration is not a permanent change, and so a key factor of therapeutic methods using epigenetic modification focusses on ‘switching’ on or off specific genes which may have been shown to promote tumour progression. Studies have shown that epigenetic regulation may offer an alternative method of treatment for tumour types which cannot be treated effectively using current methods. For example, histone deacetylase inhibitors have been utilised to reverse the effects of the eraser, histone deacetylases, which have been linked to the inhibition of tumour suppressors, promoting tumour development (Parbin et al., 2014). With the addition of histone deacetylase inhibitors, tumour progression is slowed as a result of increased apoptotic events within the tumour (Li & Seto, 2016).

1.2.2. PRC1 Complex

The Polycomb Repressive Complex 1 (PRC1) holds a key role in gene expression, through the transcriptional regulation of genes during development. The PRC1 complex consists of four sub-units; Really Interesting New Gene (RING) proteins, Polycomb Group Factor (PCGF) proteins, Human Polyhomeotic Homolog (HPH) proteins, and Chromobox (CBX) proteins. There are several versions of each sub-unit. There are two possible RING proteins, with six orthologs of the PCGF protein, additionally there are three HPH proteins, along with five possible CBX proteins observed within the PRC1 complex (Levine et al., 2002; Tajul-Arifin et al., 2003; Gao et al., 2012; Geng & Gao, 2020), as illustrated by Figure 1.9. The RING proteins have E3 ligase activity which facilitates ubiquitination of H2AK119 (Taherbhoy et al., 2015).

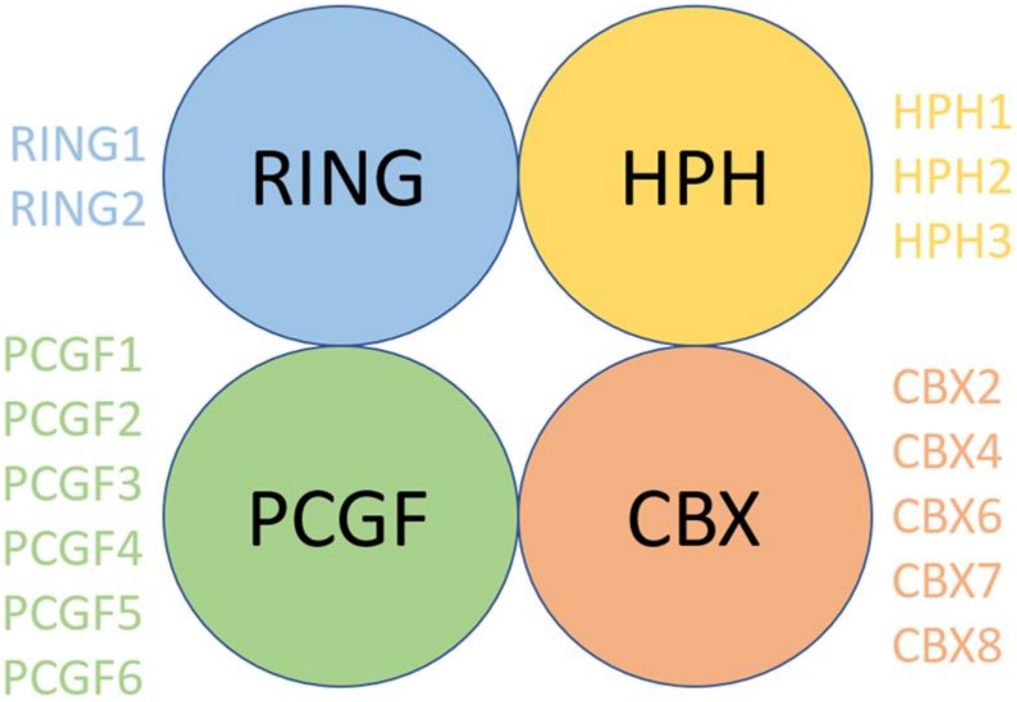

Figure 1.9. Components of the PRC1 complex. PRC1 complex comprised of four sub-units, RING, HPH, PCGF, and CBX proteins; with multiple versions of each sub-unit. Figure adapted from Waters (2019).

Due to the many sub-units of the PRC1 complex, there are multiple variations which can occur, the different combinations of which are thought to regulate the expression of different genes (Connelly & Dykhuizen, 2017). Studies into the effects of various PRC1 components are being conducted in search of possible therapeutic targets, due to the epigenetic regulatory effects of the PRC1 complex. Different factors of the PRC1 complex have been seen to be overexpressed, or in some cases, downregulated, promoting tumour progression through factors such as histone modification, for example (Nacerddine et al., 2012; Li et al., 2013; Koppens & van Lohuizen, 2016; Freire-Benéitez et al., 2021; Zheng et al., 2022). Some examples include CBX1 and CBX3, both of which have been shown to be overexpressed within hepatocellular carcinoma, with their function linked to increased cell proliferation (Yang et al., 2018; Zhang et al., 2022).

One key CBX protein is CBX2. When present within the PRC1 complex, CBX2 can recognise and silence specific genes by utilising histone modification of euchromatin to heterochromatin to ‘switch’ off gene expression by causing that gene to be transformed into its transcriptionally inactive state (Ma et al., 2014; van Wijnen et al., 2021). Acting in the capacity of an epigenetic reader protein, it has been determined that CBX2 directs the PRC1 complex to recognise the histone, H3 Lysine 27 which has undergone tri-methylation (H3K27me3) (Figure 1.10).

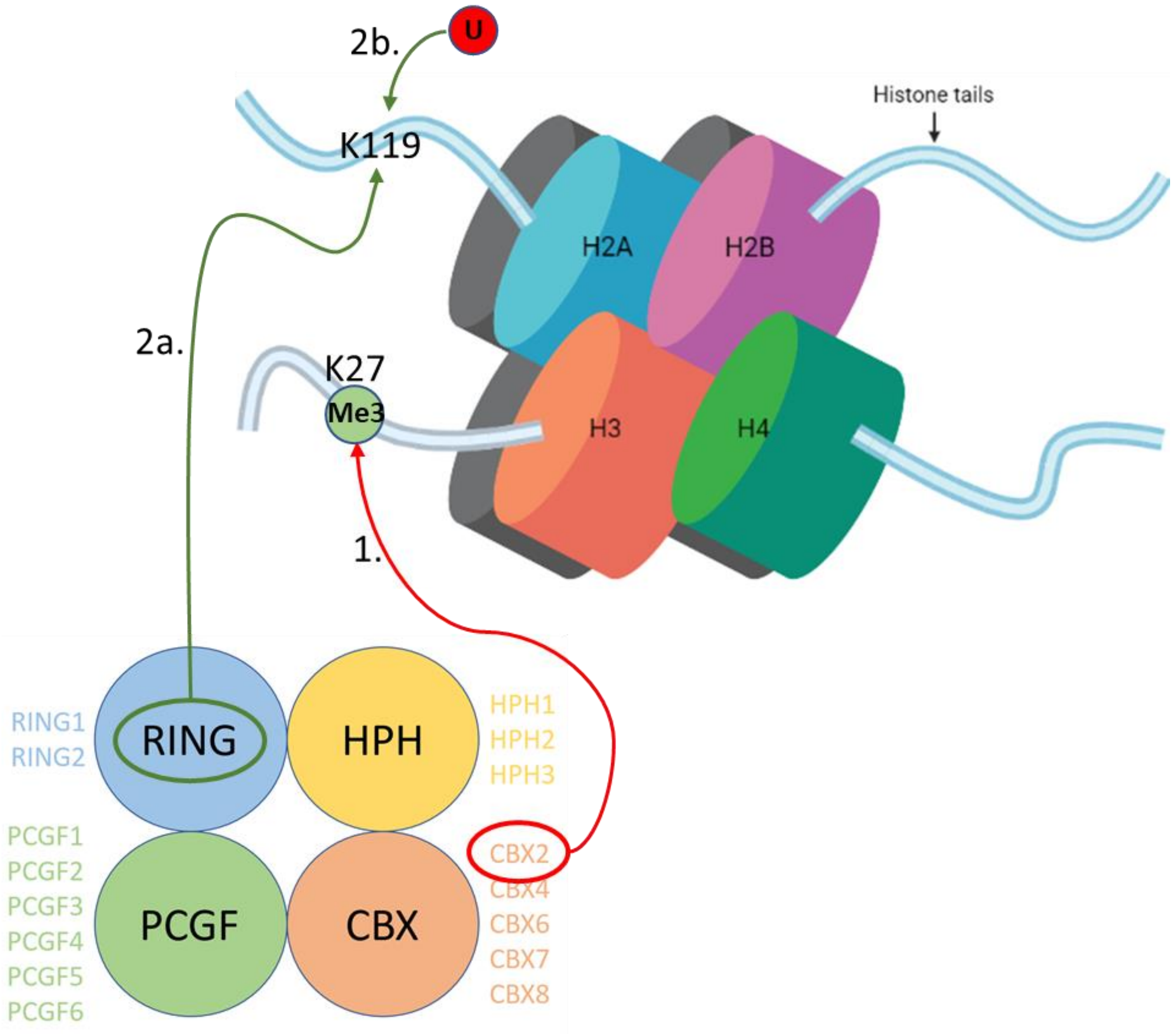

Figure 1.10. The process by which CBX2 switches off gene expression. 1) CBX2, part of the PRC1 complex, recognises H3K27me3. 2) The RING protein, part of the PRC1 complex, ubiquitinates H2AK119 which condenses chromatin and switches off gene expression.

H3K27me3, which is deposited by a secondary epigenetic regulator, Polycomb Repressive Complex 2 (PRC2), also plays a role in gene expression. It is the PRC2 complex which causes tri-methylation of H3K27, which is then recognised by the PRC1 complex (Raby et al., 2020). Of the PRC2 complex, it is the Enhancer of zeste homolog 2 (EZH2) sub-unit which completes this function (Figure 1.11).

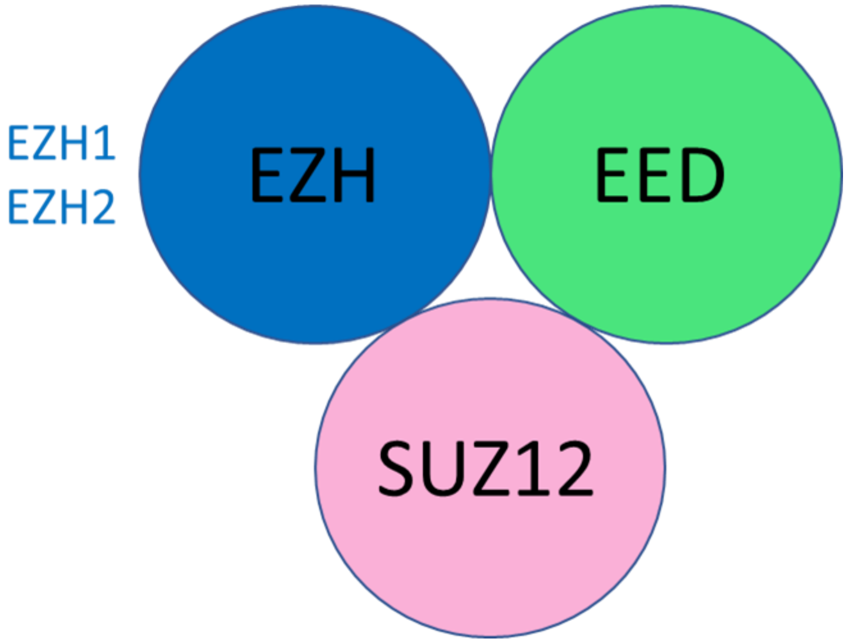

Figure 1.11. Components of the PRC2 complex. PRC2 complex comprises three sub-units, EZH, EED, and SUZ12 proteins; with two possible versions of the EZH sub-unit.

H3K27me3 binds to the chromodomain component of CBX2 within the PRC1 complex (Gil & O'Loghlen, 2014; Aranda et al., 2015). Following this, the RING protein then directs the PRC1 complex to ubiquitinate the histone, H2A Lysine 119 (H2AK119); both tri-methylation of H3K27 and ubiquitination of H2AK119 are associated with the repression/ switching off of gene expression (Bogliotti & Ross, 2012; Zhang et al., 2015). These events culminate in the condensing of chromatin to heterochromatin, making the chromatin transcriptionally inactive and ‘switching off’ gene expression, linking the presence of CBX2 to the silencing of specific genes.

With multiple CBX proteins observed, depending on which is present within the PRC1 complex, different regions within the chromatin which house H3K27me are targeted by the PRC1 complex. Together, the PRC1 and PRC2 complexes act as effective epigenetic regulators.

1.2.3. CBX2

The CBX2 protein has begun to be analysed in its capacity as an epigenetic regulator during cancer progression, specifically its possible ability to promote tumour growth and progression through silencing of key tumour suppressor genes. Key features of the protein, CBX2, suggest that it can direct and is responsible for PTM within the histone, causing targeted gene suppression. As such, epigenetic regulation is being explored for its possible applications as a therapeutic method.

Expression of the PRC1 component CBX2, has been identified as being elevated in several tumour types, including, breast cancer, gastric cancer, as well as in gliomas, and more specifically in GBM (Zheng et al., 2019; Wang et al., 2021; Zeng et al., 2021; Li et al., 2022). As a result of the overexpression of CBX2, studies have observed increased cell growth and proliferation and consequently reduced patient survival (Zheng et al., 2019). The tumorigenic properties of CBX2 have been linked to multiple pathways which promote factors such as tumour proliferation, progression, and invasion, including that of the YAP/β-catenin pathway, which is activated in the presence of elevated levels of CBX2 (Zeng et al., 2021). CBX2 has also shown to upregulate tumour proliferation through YAP within hepatocellular carcinoma (Mao et al., 2019). A study by Wheeler et al. (2018) demonstrated the effect of CBX2 on high grade serous ovarian carcinoma through knockdown of CBX2 expression in cell lines. The study looked to explore the relationship between CBX2 expression and occurrence of anoikis within the tumour. It was determined that elevated levels of CBX2, as seen within this form of ovarian carcinoma, promoted the avoidance of anoikis within cells, reducing cell death, and consequently promoting tumour growth and proliferation (Wheeler et al., 2018). Crucially, this study observed that by reducing CBX2 expression, cell proliferation was reduced, with additional benefits of a greater sensitivity to chemotherapy also observed.

CBX2 has also been analysed as an oncogenic driver within lung adenocarcinoma, with the knockdown of its expression both within *in vitro* and *in vivo* models demonstrating reduced tumour proliferation (Hu et al., 2022). The group also identified a link between CBX2 and EZH2, which both work to inhibit tumour suppressors; EZH2 is associated with histone methylation and transcriptional repression.

With CBX2 identified as an oncogenic driver, studies have started to look at the application of epigenetic regulation on reducing/ increasing CBX2 expression to further analyse its function, as well as the possibility for the protein to act as a therapeutic target. For example, a study by Bilton et al. (2022) demonstrated that CBX2 gene silencing in breast cancer is targeted towards tumour suppressors in order to promote tumour growth and progression; specifically, the tumour suppressor, Retinoblastoma-like protein 2 (RBL2).

Having observed elevated levels of CBX2 in gliomas, research has been directed towards the role of CBX2 within gliomas using epigenetic alteration to alter gene expression; knockdown of CBX2 expression conducted using short hairpin RNA (shRNA) (Wang et al., 2021). This group determined that a reduction in CBX2 expression, as facilitated by shRNA transfection agents, was able to reduce tumour proliferation and invasion. Additionally, it was seen that when expression of CBX2 was reduced, a knock-on effect was that of reduced activation of the Akt/PI3K pathway; this suggests a possible therapeutic target by which tumour proliferation can be reduced. The effect of gene silencing on tumour growth was observed in *in vitro*, 2D cell culture models, using the U-87 MG cell line for knockdown experiments and LN299 cells for CBX2 overexpression analysis. The effect of gene silencing was also observed in mice following addition of U-87 MG cells transfected with the knockdown agent into the mice brains; reduction in CBX2 expression demonstrated reduced tumour growth within the murine model (Wang et al., 2021). Thus, there is potential for the use of CBX2 as a target for treatment within GBM, by ‘knocking down’ the expression of CBX2, causing a reduction in GBM proliferation.

Research Aims and Objectives

The aim of this study is to analyse and determine the role of CBX2, an epigenetic regulator, within GBM, with the longer term objective of understanding any therapeutic potential in modulating this molecule. The work will use 2D and 3D cell models derived from the U-87 MG cell line, a well characterised mammalian GBM cell line.

The specific objectives for this study include an in-depth analysis of how CBX2 affects the growth of various brain cancer cell lines. This will be achieved through:

1) Validation of CBX2 protein (Western blot) and gene (RT-qPCR) knockdown in GBM cells using distinct CBX2 targeting siRNA.
2) Validation of CBX2 overexpression in GBM cells via transfection of plasmid constructs which express CBX2.
3) Investigation of changes to GBM cell behaviour (i.e., proliferation and death) following CBX2 knockdown and overexpression.
4) Preliminary analysis of changes in CBX2 expression in GBM spheroids maintained in a microfluidic device compared to static culture.

Chapter 2: Materials and Methods

2.1. Tissue Culture

The human GBM derived cell lines, U-87 MG (ECACC 89081402) and SNB-19 (ECACC 09063001), were selected for use within this study. Cell lines were obtained from the European Collection of Authenticated Cell Cultures (ECACC) and stored in liquid nitrogen until required. The GBM cell line U-251 MG was purchased from ECACC, however, cell line authentication using short tandem repeat (STR) profiling, completed by NorthGene (NorthGene™, 2022), identified the cell line as SNB-19, and this nomenclature is used throughout the thesis. As SNB-19 is also a glioma cell line it was used in addition to U-87 MG (Welch et al., 1995). Additional cell lines used were the breast cancer cell lines: MDA-MB-231 (human breast adenocarcinoma), MCF7 (human breast adenocarcinoma), and T47D (human breast tumour) (ECACC, 2022).

2.1.1. Cell Maintenance

All cell handling was performed under sterile conditions within a Biological Class II safety cabinet (ESCO, Singapore). All instruments and equipment used within the hood were sterilised using 2% (w/v) Virkon and 70% (v/v) ethanol. All sterile plasticware was purchased from Sigma-Aldrich, UK, and Sarstedt, UK, unless stated otherwise.

The U-87 MG and SNB-19 cell lines were cultured in Dulbecco's Modified Eagle Medium (DMEM); containing 4.5 g/L Glucose, stable L-Glutamine, as well as sodium pyruvate and sodium bicarbonate, purchased from Lonza, UK. For both cell lines, DMEM was supplemented with 10% (v/v) Foetal Bovine Serum (FBS) (Labtech, UK) and Penicillin-Streptomycin (final concentration of 0.1 U/ml and 0.1 mg/ml, respectively; purchased from Cytiva, UK). Additionally, sodium pyruvate (final concentration of 1mM, Lonza) was added to the DMEM for the SNB-19 cell line to aid growth. Roswell Park Memorial Institute (RPMI) 1640 Medium, purchased from Lonza, was used for the breast cancer cell lines, T47D, MCF7, and MDA-MB-231. The RPMI media contained L-Glutamine and was supplemented with FBS and Penicillin-

Streptomycin, as above. All supplements were added to the media using 20ml Luer syringes (BD Plastipak™, UK, Ref: 300613) and 0.22µm PES syringe filter (Sartorius, Germany). Cell lines were maintained at 37˚C in a 5% CO_2 atmosphere. The sub-culture routine was performed as per the instructions given by ECACC, requiring cells to be at 70-80% confluency before cells could be split. Cells were maintained within sterile, polystyrene, T75 flasks, with a growth surface of $75cm^2$. Cells were removed from the tissue culture flasks using trypsinisation, for which, 1x Trypsin (0.025%)/ EDTA (0.01%) (Gibco, USA) was used. Prior to trypsinisation, media was allowed to warm to 37˚C in a water bath (Stuart, SWB series, UK) to encourage cell growth.

When performing trypsinisation, all DMEM was removed from the flask and cells were gently washed in Phosphate Buffered Saline (PBS) to ensure all media was removed. The PBS was discarded before an appropriate volume of Trypsin/ EDTA was added. A rule of 1ml of Trypsin/ EDTA per $25cm^2$ of flask growth space was used, therefore 3ml of Trypsin EDTA was added when using T75 flasks. The flask was then incubated at 37˚C in a 5% CO_2 atmosphere for a minimum of 5 minutes (no more than 10 minutes incubation to prevent cell death). Once the cells had fully dissociated from the flask wall, an equal volume of DMEM was added to the flask to neutralise the enzymatic action of trypsin. The cell suspension was then centrifuged for 3 minutes at 400 Relative Centrifugal Force (RCF) to form a pellet using a Centrifuge 5702 (Eppendorf®, UK). The pellet was finally resuspended in 4ml of fresh DMEM, and 1ml of cell suspension was then added to each new flask along with 19ml of fresh media (1:19). The flask was returned to the incubator to allow cells to continue growing.

Cell lines were routinely frozen down and stored in liquid nitrogen to maintain low passage numbers; cells below passage 20 were considered low enough to freeze, with cells being used up to passage 40 before a new batch of cells was obtained from storage. Cells were suspended in a solution of 10% (v/v) Dimethyl sulfoxide (DMSO) (Fisher Scientific, USA) and 90% (v/v) FBS to aid cell survival during freezing and thawing.

2.1.2. Cell Counting

The number of cells present must be counted when setting up 2D short interfering RNA (siRNA) knockdown and plasmid overexpression experiments, when analysing the number of cells present following 2D siRNA knockdown and plasmid overexpression, as well as during the formation of spheroids. Cell counting was performed using an improved Neubauer haemocytometer (Hawksley, UK). Cells were obtained for counting as described in 2.1.1. Once in pellet form, the supernatant was removed, and the cell pellet was then re-suspended in 2.5ml of fresh media. By pipette, 10µl of the cell suspension was obtained and placed into a 0.5ml Eppendorf tube. Trypan blue (10µl) (Cytiva) was then added to the Eppendorf tube and the sample mixed by gentle pipetting. A haemocytometer and cover slip were cleaned using 70% ethanol before the cover slip was secured to the haemocytometer; the sample was then loaded onto the haemocytometer and analysed under a microscope. The cells present within the 4 outer grids of the haemocytometer were counted (Figure 2.1). Only live, white, cells were counted; any blue, dead cells identified from the uptake of Trypan blue were not counted. Following use, the haemocytometer and cover slip were cleaned using 70% ethanol.

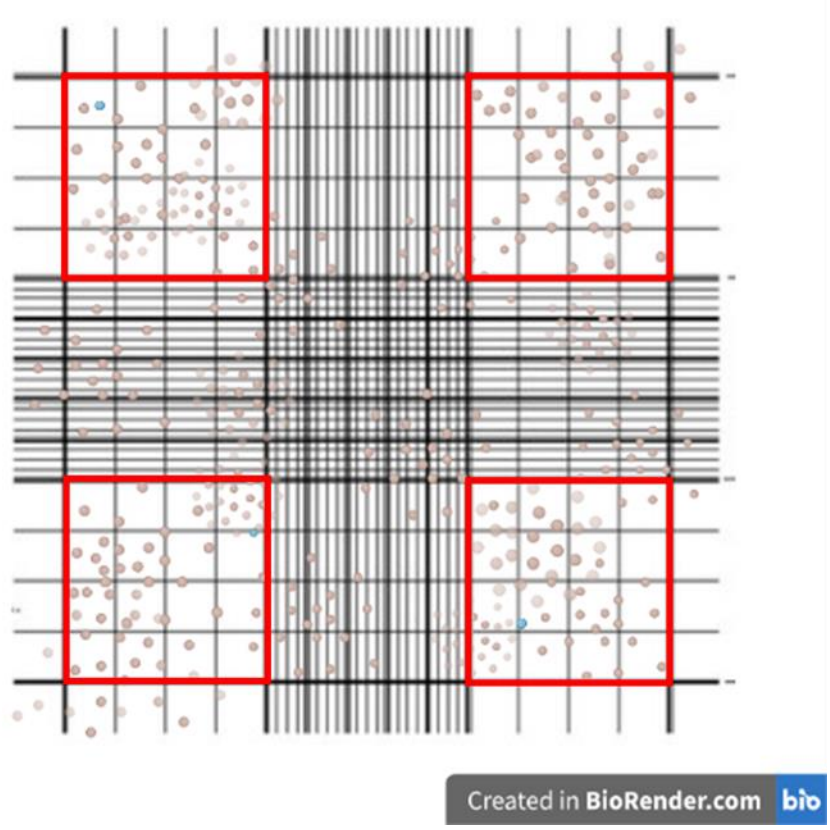

Figure 2.1. Representation of a haemocytometer grid with cells. The squares which were counted are highlighted in red. Cells which were touching the lines were counted, so that only the cells on the North and East (top and right) sides were counted, preventing duplicates. Cells stained with trypan blue; dead cells stained blue, with live cells remaining unstained. Figure produced using BioRender.

The following calculation was used to calculate the number of cells/ml of cell suspension:

$$Total\ cells\ counted\ \times \frac{Dilution\ factor}{Number\ of\ squares\ counted}\ x\ 10^4$$
$$= Cell\ concentration\ (cells/ml)$$

Example of calculation, with a cell count of 299 cells:

$$299\ \times \frac{2}{4} \times\ 10^4 = 1.495 \times 10^6\ cells/ml$$

The dilution factor is 2 due to the equal quantities (10µl) of cell suspension and trypan blue used.

The number of cells per ml of suspension was then used to determine the quantities of cell suspension and media needed to obtain the required number of cells for the formation of spheroids and 2D knockdowns.

2.1.3. Formation of Spheroids

As the 3D model of choice, spheroids were selected for use for their improved representation of the TME (Brüningk et al., 2020). Spheroids were produced using both the U-87 MG and SNB-19 cell lines, as well as all three breast cancer cell lines, MDA-MB-231, MCF-7, and T47D. For the formation of spheroids, 96-well ULA plates (Corning, UK) were employed. Cells were harvested and counted as described in 2.1.1 and 2.1.2, and the cell suspension diluted to the required concentration. For the U-87 MG cell line, 20,000 cells per well were required for each spheroid, whereas the SNB-19 cell line required 35,000 cells per well. All three breast cancer cell line spheroids were made up with 20,000 cells per well. The media required to dilute the cell suspension was calculated using the following equation (example included):

Result of cell count – 1.495×10^6 cells/ml

$$\frac{1.495 \ \times 10^6}{20000 \ \times 10} - 1$$
$$= 6.475 \, ml \ (Total \ amount \ of \ media \ to \ be \ added \ to \ 1ml \ of \ cell \ suspension)$$

This calculation gives a solution of 2.0×10^5 cells/ ml (the calculation was altered as required for cells which required more cells/ well). To form the spheroids, 100µl of the cell suspension was loaded into the individual wells of a 96-well ULA plate, equivalent to 20,000 cells/ well (Figure 2.2). To reduce evaporation of the media, 100µl of sterile PBS was loaded into the outer wells of the 96-well plate.

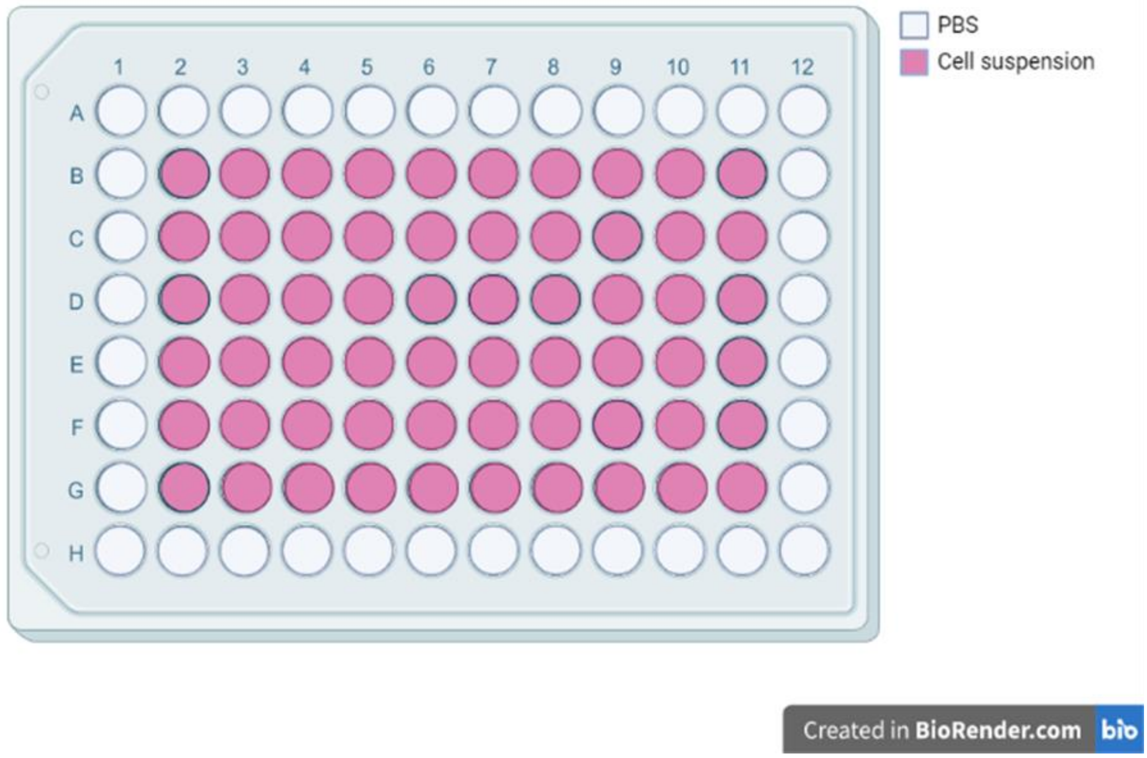

Figure 2.2. Representation of loading pattern for PBS and cell suspension into 96-well ULA plate (Corning), for spheroid formation. Figure produced using BioRender.

The plate was then incubated at 37˚C in a 5% CO_2 atmosphere for 72 hours to allow spheroid formation to occur (Figure 2.3). The spheroids were then used as part of 3D siRNA knockdown and microfluidic experiments; the spheroids will continue to grow for as long as is required, but will plateau in size after approximately 12 days, allowing changes in cell growth and protein expression to be observed. When maintaining the spheroids longer than 72 hours, additional media was added to replace any evaporated media. For example, 72 hours after the initial loading of cells, 100µl of fresh media was loaded into each well. Subsequently, every 2 or 3 days 100µl of media was removed from each well and replaced with 100µl of fresh media; so as not to exceed the volume of the well.

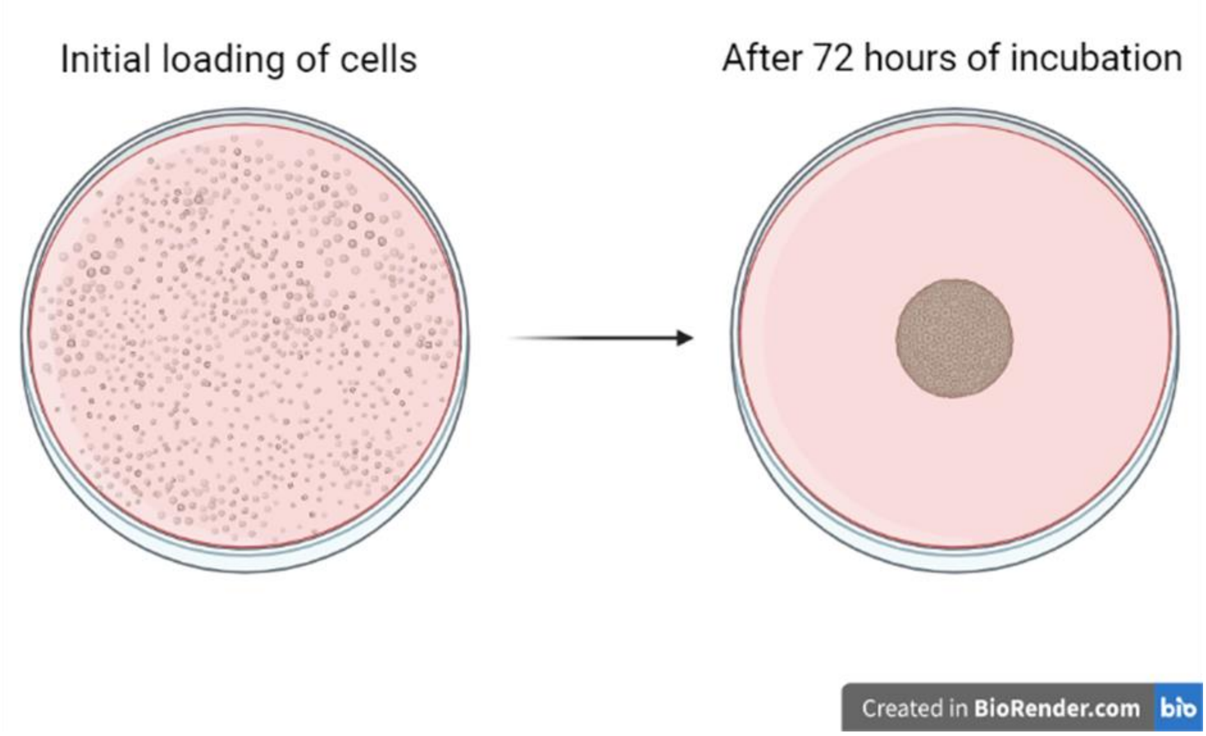

Figure 2.3. Visual representation of spheroid formation. Cells loaded into a single well of a 96-well ULA plate (Corning) (left), followed by the formation of the spheroid after 72 hours of incubation at 37˚C in a 5% CO_2 (right). As an example, the U-87 MG cells formed spheroids between 0.6 – 0.75mm after 72 hours of incubation. Figure produced using BioRender.

2.2. siRNA Knockdown

U-87 MG and SNB-19 were transfected with siRNA to achieve CBX2 mRNA knockdown. Custom scrambled-siRNA (siScr) and three CBX2-targeting siRNA were obtained from Sigma-Merck, with siScr acting as a non-targeting negative control. The three CBX2-targeting siRNA used were siCBX2 #1, siCBX2 #3, and siCBX2 #4, which were also used as part of the Bilton et al. (2022) study (Table 2.1). Transfection of cells with siRNA was facilitated by the addition of Invitrogen™ Lipofectamine™ RNAiMAX Transfection Reagent (Thermofisher, UK). The transfection of siRNA knockdown agents using Lipofectamine RNAiMAX has also been performed by other research groups to analyse the role of genes/ proteins (Dominguez-Sola et al., 2007).

Table 2.1. Sense and antisense strand sequences of custom siRNA.

siRNA	Sequences	
	Sense strand Sequence (5' - 3')	Antisense strand Sequence (5' - 3')
siScr	UUCUCCGAACGUGUCACGU	ACGUGACACGUUCGGAGAA
siCBX2#1	AGGAGGUGCAGAACCGGAA	UUCCGGUUCUGCACCUCCU
siCBX2#3	GCAAGGGCAAGCUGGAGUA	UACUCCAGCUUGCCCUUGC
siCBX2#4	CAAGGAAGCUCACUGCCA	UGGCAGUGAGCUUCCUUG

Transfection of siRNA targeting CBX2 was performed on 2D and 3D cells. Using CytoOne® RNase free 6-well plates (Starlab, UK), cells were loaded onto the plates at 150,000 cells/ well for the 2D model. Spheroids were produced for the 3D experiments as described in Section 2.1.3, with U-87 MG spheroids seeded in ULA plates at 20,000 cells/well, and SNB-19 spheroids seeded at 35,000 cells/well. Spheroids were grown for 72 hours before the transfection agents were loaded onto the cells.

For the transfection, a mastermix of basal media, siRNA, and RNAiMAX was prepared and allowed to incubate at room temperature for a minimum of 20 minutes (Table 2.2.); the siRNA and RNAiMAX were kept on ice when preparing the mastermix.

Table 2.2. Reagents used for siRNA knockdown Mastermix, with concentrations and volumes used.

Reagent	Volume used per sample (2D transfections)	Volume used per sample (3D transfections)
Basal Media	100µl	10µl
Custom siRNA (50µM stock)	1µl	0.1µl
RNAiMAX	2µl	0.2µl

For both the 2D and 3D knockdown experiments the transfection solution was made-up to a siRNA concentration of 25nM. For the 2D method, 100µl of the made-up siRNA Mastermix was loaded into the corresponding wells, with 2ml of the 75,000 cells/ml cell suspension added slowly to the side of the well. The 3D transfection was performed 72 hours after the spheroids were seeded in the ULA plates, with 10µl of the 25nM siRNA solution loaded into each well; 12 spheroids were loaded with each custom siRNA Mastermix. A visual representation of the 2D and 3D siRNA loading patterns can be seen in Figure 2.4.

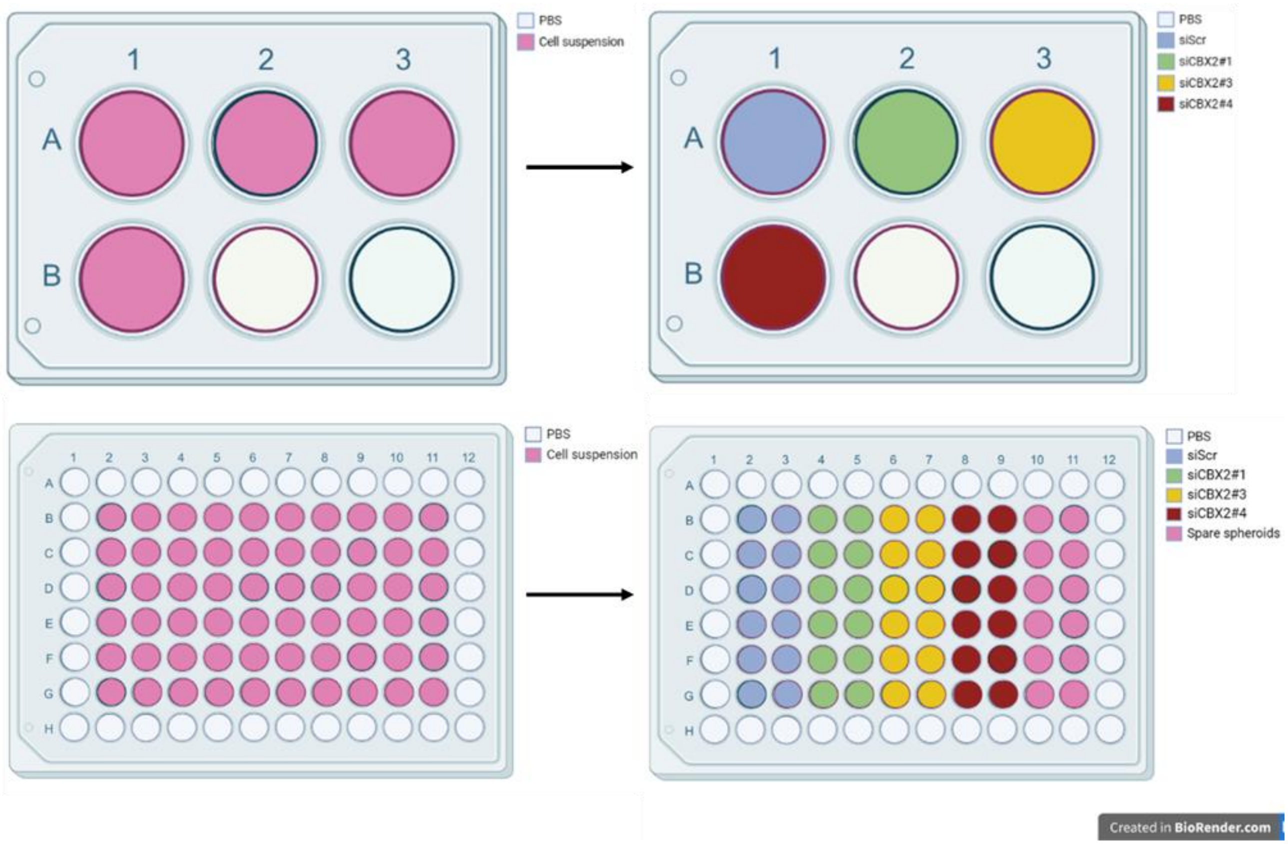

Figure 2.4. Visual representation of the loading pattern for the siRNA knockdown experiments. (Top Left) Loading pattern of cell suspension for 2D siRNA, in which 4 wells were loaded with the required cells/ml, using a 6-well RNase free plate. (Top right) Loading pattern for siRNA variations in 2D siRNA experiments. (Bottom left) Loading pattern of cell suspension for 3D siRNA, in which 60 wells were loading with the required cells/well as required by each cell line, using a ULA 96-well plate (Corning). (Bottom right) Loading pattern for siRNA variations in 3D experiments. Figure produced using Biorender.

Images were taken of the 2D cells 72 hours post-seeding, prior to collection. Images of the spheroids were taken after 48 and 96 hours (and after 168 hours in some cases), using a Gelcount (Oxford Optronix, UK) and processed using ImageJ (Version 1.53M). The 2D cells were incubated for 72 hours following transfection before the cells were collected and cell counts were performed as per 2.1.2. Following the cell counts, cells were pelleted using a GenFuge 24D minicentrifuge (Progen, UK) and the media removed; to ensure all media was removed, the cells were washed with the addition of PBS, and then centrifuged again before the PBS was also removed. The cells were lysed using a solution of RIPA buffer and Pierce™ Protease Inhibitor Mini Tablets (Cat no. #A32955, Thermo Scientific™, UK); one mini tablet dissolved in 10ml of RIPA buffer (Table 2.3.). The cell pellets were lysed in 60µl of RIPA buffer and protease inhibitor solution, centrifuged using a 5804 R Centrifuge (Eppendorf, UK) for 15 minutes at 10,000 revolutions per minute (RPM) at 4˚C, and the supernatant retained and frozen at -20˚C for analysis.

Table 2.3. Components used for RIPA buffer.

Ingredients for RIPA buffer solution	
▪ **ddH$_2$O (to dilute)**	▪ **NaCl, 150 mM**
▪ **25mM Tris-HCl, pH 7.6**	▪ **Sodium dodecyl sulphate, 0.1% (w/v)**
▪ **Sodium deoxycholate, 1% (w/v)**	
▪ **Nonidet NP-40, 1% (v/v)**	

Spheroids were collected 96 hours (168 hours in some cases) following transfection. The media was removed from the spheroids before PBS was added to remove any remaining media; the PBS was then also removed. The U-87 MG spheroids were lysed with 80µl of RIPA buffer and protease inhibitor solution. The SNB-19 spheroids were also collected after 96 hours of incubation - due to their smaller size only 60µl of RIPA buffer and protease inhibitor solution was required for lysing.

Repeat sets of siRNA knockdowns were performed simultaneously, as above, with the cells (2D model) and spheroids (3D model) being used for quantitative Reverse Transcription Polymerase Chain Reaction (RT-qPCR). For this, the cells were allowed to incubate for 72 hours, as mentioned previously, before being collected and centrifuged to produce a pellet for RNA extraction (cells washed with PBS and re-spun, as above). The spheroids were incubated for 96 hours following the addition of the various test siRNA mastermix, after which the spheroids were collected. RNA extraction was performed on the pooled spheroids. The RNA extraction protocol is outlined in Section 2.6.

Additional siRNA experiments were completed using the breast cancer cell lines, T47D, MCF7, and MDA-MB-231, using the methods described above. MDA-MB-231 cells were used for a 2D siRNA knockdown experiment, whereas T47D, MCF7, and MDA-MB-231 were used for 3D siRNA knockdown experiments; spheroids were produced using 20,000 cells/ well. The resulting cell pellets from the 2D and 3D siRNA experiments performed on the breast cancer cells were analysed using western blotting and RT-qPCR, as described for the U87 and SNB-19 cells.

2.3. Overexpression

Overexpression of CBX2 was performed on the U-87 MG and SNB-19 cell lines by transfection of a plasmid containing a full length or a truncated sequence of the CBX2 gene. Customised plasmids were designed for this purpose; the plasmids used were produced by the Kawaguchi et al. (2017) group. Three plasmids were designed, as outlined in Figure 2.5: a pFLAG control plasmid consisting of an empty vector with the FLAG tag present, a full length CBX2 plasmid wildtype (with FLAG tag present, predicted 72kDa), as well as a mutated CBX2 plasmid with missing chromodomain sequence (with FLAG tag present); plasmid stocks generated by Dobrowinski (2022). Transfection of the plasmids was achieved using Lipofectamine™ 3000 Transfection Reagent (Invitrogen, USA). Overexpression of CBX2 was performed on a 2D model of cell lines. Overexpression of CBX2 in breast cancer cells has recently been conducted by Bilton et al. (2022), in which the same transfection method was utilised.

A)

pFLAG plasmid sequence

NNGGGGGCATNAAGCAGAGCTGGGTTTAGTGAACCGTCAGATCCGCTAGCGCTACCGGTCGCCACC**ATGGACTACAAGGACGACGATGACAAG**CCTTCC
GGACTCAGATCTCGAGCTCAAGCTTCGAATTCTGCAGTCGACGGTACCGCGGGCCCGGGATCCACCGGATCTAGATAACTGATCATAATCAGCCATACCACAT
TTGTAGAGGTTTTACTTGCTTTAAAAAACCTCCCACACCTCCCCCTGAACCTGAAACATAAAATGAATGCAATTGTTGTTGTTAACTTGTTTATTGCAGCTTATA
ATGGTTACAAATAAAGCAATAGCATCACAAATTTCACAAATAAAGCATTTTTTTCACTGCATTCTAGTTGTGGTTTGTCCAAACTCATCAATGTATCTTAACGCGT
AAATTGTAAGCGTTAATATTTTGTTAAAATTCGCGTTAAATTTTTGTTAAATCAGCTCATTTTTTAACCAATAGGCCGAAATCGGCAAAATCCCTTATAAATCAAA
AGAATAGACCGAGATAGGGTTGAGTGTTGTTCCAGTTTGGAACAAGAGTCCACTATTAAAGAACGTGGACTCCAACGTCAAAGGGCGAAAAACCGTCTATC
AGGGCGATGGCCCACTACGTGAACCATCACCCTAATCAAGTTTTTTGGGGTCGAGGTGCCGTAAAGCACTAAATCGGAACCCTAAAGGGAGCCCCCGATTTA
GAGCTTGACGGGGAAAGCCGGCGAACGTGGCGAGAAAGGAAGGGAAGAAAGCGAAAGGAGCGGGCGCTAGGGCGCTGGCAAGTGTAGCGGTCACGC
TGCGCGTAACCACCACACCCGCCGCGCTTAATGCGCCGCTACAGGGCGCGTCAGGTGGCACTTTTCGGGGAAATGTGCGCGGAACCCCTATTTGTTTATTTT
TCTAAATACATTCAAATATGTATCCGCTCATGAGACAATAACCCTGATAAATGCTTCAATAATATTGAAAAAGGAAGAGTCCTGAGGCGGAAAGAACCAGCTGT
GGAATGGGTGTCAGTTAGGGGGGGGAAAGTCCCCAGGCTCCCCAGCAGGCAAAAGTAAGCAAAGCATGCTTCTCATTTAGCCGCAACCAGGGGGGGAAA
GTCCCAGGCTCCCCACCAGGCAAANNTTTGCAAAGCTGGCTTCTAATTTATNNAAAAACCAATTTCCCNCCCCTAAATCCCCCCCCCCCCCCTAAAACCNGCC
CNNNTTCCCCCCATTTCTCCCCCCNNGGGGTAAAATTTTTTTTTTTNNNTTAGGAGGGNGAANGCCCCCCCGCGCCTCTGGAAATT

Full Length CBX2 plasmid sequence

NCNNGGGGGCATTTAGCAGAGCTGGTTTAGTGAACCGTCAGATCCGCTAGCGCTACCGGTCGCCACC**ATGGACTACAAGGACGACGATGACAAG**CCTTCC
GGACTCAGATCTCGAGCTCAAGCTTCGAATTCTGCAGTCGACGGTACCGCGGGCCCGGGAT**CTATGGAGGAGCTGAGCAGCGTGGGCGAGCAGGTCTTC**
GCCGCCGAGTGCATCCTGAGCAAGCGGCTCCGCAAGGGCAAGCTGGAGTACCTGGTCAAGTGGCGCGGCTGGTCCTCCAAACATAACAGCTGGGAGCC
GGAGGAGAACATCCTGGACCCGAGGCTGCTCCTGGCCTTCCAGAAGAAGGAACATGAGAAGGAGGTGCAGAACCGGAAGAGAGGCAAGAGGCCGAG
AGGCCGGCCAAGGAAGCTCACTGCCATGTCCTCCTGCAGCCGGCGCTCCAAGCTCAAGGAACCCGATGCTCCCTCCAAATCCAAGTCCAGCAGTTCCTCCTC
TTCCTCCACGTCATCCTCCTCTTCCTCAGATGAAGAGGATGACAGTGACTTAGATGCTAAGAGGGGTCCCCGGGGCCGCGAGACCCACCCAGTGCCGCAGA
AGAAGGCCCAGATCCTGGTGGCCAAACCCGAGCTGAAGGATCCCATCCGGAAGAAGCGGGGACGAAAGCCCCTGCCCCCAGAGCAAAAGGCAACCCGAA
GACCCGTGAGCCTGGCCAAGGTGCTGAAGACCGCCCGGAAGGATCTGGGGGCCCCGGCCAGCAAGCTGCCCCCTCCACTCAGCGCCCCCGTTGCAGGCCT
GGCAGCTCTGAAGGCCCACGCCAAGGAGGCCTGTGGCGGCCCCAGTGCCATGGCCACCCCAGAGAACCTGGCCAGCCTAATGAAGGGCATGGCCAGTAG
CCCCGGCCGGGGTGGCATCAGCTGGCAGAGCTCCATCGTGCACTACATGAACCGGATGACCCAGAGCCAGGCCCAGGCTGCCAGCAGGTTGGCGCTGAAG
GCCCAGGCCACCAACAAGTGCGGCCTCGGGCTGGACCTGAAAGGGAAGANACAAAAAGGGGAACTGGGAATGACCCCTCCAGGAAGCAAAATCCCAAA
GGCCCCAGCGGTGGGGCNGGGGAACAAAAAGGGGGAAACCAGGGGGCCCCCGCAACCCATGGTGCCAACAGGGGGCCGGGTGGGGGGCCGGGCCCC
CCNNCANCCCCCCCCCNNNGAACTGAAACCCCCGGTTTTGGATTTAAAAGNTAAAAAGGGGGGGCCCGGGGGGGGGTCCCTTGCCCCCCCCCCCNCCCC
CCCAGGGGGTGCGCCNCCCCCCCCCCCCCCGGGGGGGGNCGG

CBX2 plasmid sequence with missing Chromodomain

NNNGGGGCTTTAAGGCAGTAGCTGGTTTAGTGAACCGTCAGATCCGCTAGCGCTACCGGTCGCCACC**ATGGACTACAAGGACGACGATGACAAG**CCTTCC
GGACTCAGATCTGAGAAGGAGGTGCAGAACCGGAAGAGAGGCAAGAGGCCGAGAGGCCGGCCAAGGAAGCTCACTGCCATGTCCTCCTGCAGCCGGCG
CTCCAAGCTCAAGGAACCCGATGCTCCCTCCAAATCCAAGTCCAGCAGTTCCTCCTCTTCCTCCACGTCATCCTCCTCTTCCTCAGATGAAGAGGATGACAGTG
ACTTAGATGCTAAGAGGGGTCCCCGGGGCCGCGAGACCCACCCAGTGCCGCAGAAGAAGGCCCAGATCCTGGTGGCCAAACCCGAGCTGAAGGATCCCAT
CCGGAAGAAGCGGGGACGAAAGCCCCTGCCCCCAGAGCAAAAGGCAACCCGAAGACCCGTGAGCCTGGCCAAGGTGCTGAAGACCGCCCGGAAGGATC
TGGGGGCCCCGGCCAGCAAGCTGCCCCCTCCACTCAGCGCCCCCGTTGCAGGCCTGGCAGCTCTGAAGGCCCACGCCAAGGAGGCCTGTGGCGGCCCCA
GTGCCATGGCCACCCCAGAGAACCTGGCCAGCCTAATGAAGGGCATGGCCAGTAGCCCCGGCCGGGGTGGCATCAGCTGGCAGAGCTCCATCGTGCACTA
CATGAACCGGATGACCCAGAGCCAGGCCCAGGCTGCCAGCAGGTTGGCGCTGAAGGCCCAGGCCACCAACAAGTGCGGCCTCGGGCTGGACCTGAAGGT
GAGGACGCAGAAAGGGGAGCTGGGAATGAGCCCTCCAGGAAGCAAAATCCCGAAGGCCCCCAGCGGTGGGGGCTGTGGAGCAGAAAGTGGGGAACAC
AGGGGGCCCCCGCACACCCATGGTGCCAGCAGGGTGCCTGCTGGGTGCCCAGGCCCCCAGCCAGGCACCCACCCAGGAAGCTGAACCTCCCAGGTCTTG
GAACTTGCAAAAAGGTCAAGAATGGCATGCCCCGGGGTGGGGTTTCCTTGCCCCCCCCCGCCCCCCGCCCCCAAGGGGGGGCCCGGGCCCCCCACCCCCA
CCCCCTGGGGAAAGGGGGCGGGGGAAGGGGGCCCCTTTTGGGGCCCCGGGGGCCCCCCCTCCCCCCCCCAANNNAAAAAAAAGAAAAAAAATGGGTTT
TCAAAAAAAAGGGGGGCCCCCCCCCCTCCCCGTCNNNNAAAAAGGGAGGGGGTTTCGGGGGGGGGGGGGTTCCCCCCCCCGTGGGGGANAGNA

Figure 2.5. Plasmid sequences and schematic representation. A) Plasmid sequences for the three plasmids used for overexpression experiments. The pFLAG region is highlighted in green and the chromodomain region highlighted in blue. (Top) pFLAG plasmid sequence, an empty vector with pFLAG tag present. (Middle) Full length CBX2 plasmid sequence with added pFLAG tag present; chromodomain present within the full length sequence. (Bottom) CBX2 plasmid sequence with missing chromodomain. Sequence map track generated by (Dobrowinski, 2022). B) Schematic representation of the three plasmids used; where AT represents the AT hook and Pc refers to the Pc box.

Having obtained a cell suspension according to Section 2.1.1. a cell count was completed, and a cell suspension of 75,000 cells/ml was prepared. For each plasmid used, 2ml of the cell suspension was added slowly to the side of the well of a CytoOne® RNase free 6-well plates (Starlab); total of 150,000 cells/ well. Once seeded, cells were allowed to grow for 24 hours at 37˚C at 5% CO_2 before each of the plasmids were loaded.

After 24 hours of incubation the plasmids were prepared for addition to the cells. During the preparation, Lipofectamine™ 3000 Transfection Reagent (Invitrogen, USA), P3000 enhancer reagent (Invitrogen, USA), and the plasmids were kept on ice. The plasmid mix was prepared according to Table 2.4; from a 100 ng/µl plasmid stock, the transfection solution was made-up to a final total plasmid quantity of 1µg, which was loaded into each well.

Table 2.4. Reagents used for siRNA overexpression plasmid Mastermix, with concentrations and volumes used.

Reagent	Volume used per sample
Basal Media	125µl
Custom plasmid (100 ng/µl)	10µl
P3000 enhancer reagent	2µl

Having prepared the plasmid mix for each plasmid, Lipofectamine 3000 was diluted with basal media, with the volume used per sample multiplied for the number of wells/ repeats being run, as outlined in Table 2.5.

Table 2.5. Reagents used for dilution of Lipofectamine 3000, ready for addition to plasmids.

Reagent	Volume used per sample	Volume used when preparing 3 plasmids worth of lipofectamine
Basal media	125µl	375µl
Lipofectamine 3000	4µl	12µl

Once the plasmids and lipofectamine mix were prepared, 125µl of the lipofectamine mix was added to each plasmid mix. The contents were homogenised through pipetting and allowed to incubate at room temperature for 15 minutes. After the incubation period, the reagents were mixed again and then loaded into the appropriate wells, with 250µl of each plasmid mastermix added slowly into the corresponding well; Table 2.6. illustrates the contents of the prepared plasmid mix per well. The cells were allowed to incubate at 37˚C at 5% CO_2 for 72 hours after transfection, before samples were collected for analysis.

Table 2.6. Final contents of overexpression plasmid components in each well.

Reagent	Volume used per sample
Basal Media	250µl
Custom plasmid (100 ng/µl)	10µl
P3000 enhancer reagent	2µl
Lipofectamine 3000	4µl

Images were taken of the 2D cells 72 hours after the addition of the plasmids, prior to collection. The cells were then collected, and cell counts were performed as per Section 2.1.2. Following the cell counts, cells were pelleted and lysed using a solution RIPA buffer and Pierce™ Protease Inhibitor Mini Tablets, as outlined in Table 2.3. and according to the protocol outlined in Section 2.2. for 2D cells. Namely, that the cell pellets were lysed in 60µl of RIPA buffer and protease inhibitor solution before centrifugation; protein lysates stored at -20˚C.

Further repeats of the overexpression experiments were performed, with the cell pellets undergoing RNA extraction, for RT-qPCR (RT-qPCR outlined in Section 2.6.).

2.4. Western Blotting

Having produced cell lysates as previously described in Sections 2.2. and 2.3., a Bicinchoninic acid (BCA) assay was performed per the manufacturer's instructions to determine the total protein concentration for each lysate. The BCA assay was read using the Synergy™HT Bio-Tek system (BioTek, USA) and analysed using Gen5 1.08 software. Using the results from the BCA assay, an appropriate volume of sample was used to allow 100µg of protein to be loaded into each well of the precast protein gel, as outlined below; in a total volume of 18µl per sample (PBS was used as the diluent). Following this, western blotting was performed to analyse the presence of CBX2 within each cell line, as detailed below (Bass et al., 2017).

Precision Plus Protein Dual Colour Standards (Bio-Rad, UK) were selected for use as the protein ladder; 7.5µl of the ladder was loaded into the first well. Positive controls used included cell lysates from a breast cancer cell line (MDA-MB-468), as well as a cell lysate made from a confluent flask of U-87 MG cells. The cell lysates were reduced using a 2x Laemmli sample buffer made from a 5x stock. 2x sample buffer was prepared by the addition of 125µl of β-mercaptoethanol (14.3M stock) and 1.5ml of distilled water to 875µl of 5x sample buffer (Bio-Rad). The sample buffer was then added to the prepared samples, with 18µl of the 2x sample buffer added to give a total volume of 36µl. To dissociate the protein samples, they were heated on a digital dry bath (Labnet, USA) for 3 minutes at 95˚C, before being placed on ice for 1 minute. Samples were then briefly centrifuged at 13,000 RPM for 15 seconds, using a GenFuge 24D minicentrifuge. The samples were then placed on ice until being loaded into a 10% Mini-PROTEAN® TGX™ Precast Protein Gel (Bio-Rad) and separated by sodium dodecyl sulphate–polyacrylamide gel electrophoresis (SDS-PAGE). Any empty wells were loaded with 36µl of PBS to prevent samples from diffusing into empty wells. The running buffer used was 1x Tris/Glycine/SDS, which was diluted from a 10x stock (Bio-Rad), prior to use, using dH_20.

SDS-PAGE was run for approximately 1.5 hours at 100V using a PowerPac™ Basic Power Supply (Bio-Rad) to ensure that the ladder and samples moved evenly down the gel. The SDS-PAGE tank (Bio-Rad) was held in a tub of ice to keep the gel cool during protein separation (Figure 2.6).

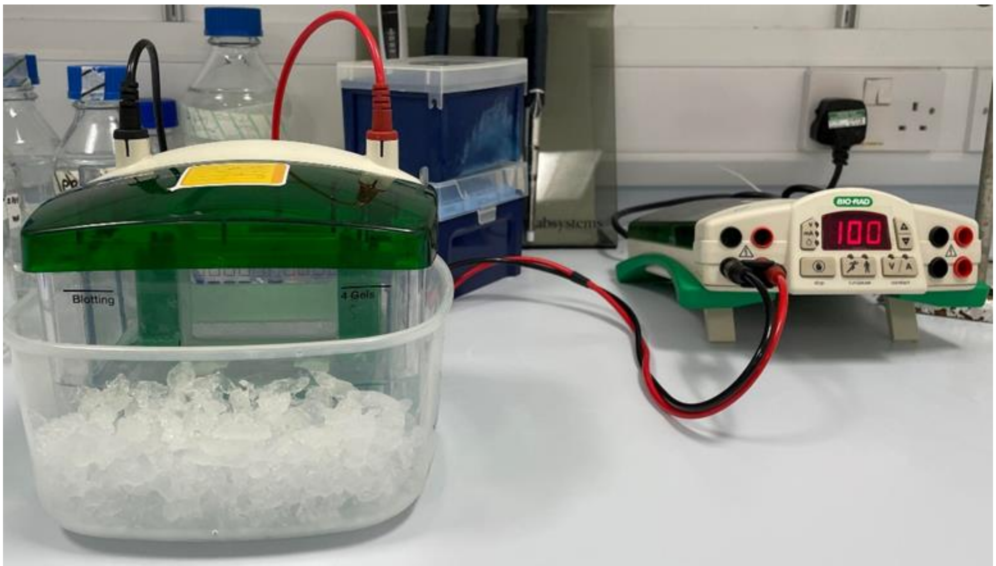

Figure 2.6. Electrophoresis set up. Bio-Rad SDS-PAGE tank connected to a PowerPac™ Basic Power Supply. The samples were loaded into a 10% Mini-PROTEAN® TGX™ Precast Protein Gel. Electrophoresis was run at 100V, with ice added to prevent the gel from overheating.

Following SDS-PAGE, the gel was removed from its cast and transferred to an Immun-Blot® polyvinylidene difluoride (PVDF) membrane (Bio-Rad) for easier handling. A Trans-Blot® Turbo™ Transfer System (Bio-Rad) was used alongside the Trans-Blot Turbo 5x Transfer buffer (Bio-Rad); transfer buffer made-up as per the manufacturer's instructions. Transfer of the western blot was completed in 3 minutes. After successful transfer, the membrane was blocked in 5% (w/v) skimmed milk powder (Marvel, UK) made up in 1x Tris buffered saline with added Tween20 (TBST) (0.1% Tween, Sigma) for an hour before overnight incubation at 4˚C in the primary antibody, CBX2 (1:1000 dilution ratio, Cat. No. ab80044, Abcam, UK). The 10x TBST stock was produced according to Table 2.7; diluted to a working 1x Tris buffer using dH_20. After overnight incubation with the primary antibody, the membrane was washed in 1x TBST to prepare the membrane for the secondary antibody. Subsequent incubation used the secondary antibody, goat anti-rabbit immunoglobulins/HRP (1:2000 dilution ratio, code number: P0448, Dako via Agilent, USA). Following 45 minutes of incubation with the secondary antibody, further washes in 1x TBST were conducted.

Table 2.7. Components used for 10x Tris buffer.

Ingredients for 10x Tris buffer solution	
▪ **dH_2O, initially 800ml, topped up to 1L following pH testing.**	▪ **10ml Tween20**
▪ **24.2g Tris**	▪ **pH = 7.6**
▪ **80g NaCl**	

To image the membranes, Clarity™ Western ECL Substrate (Bio-Rad), an enhanced chemiluminescence (ECL), was used; the Peroxide Reagent was combined with the Luminol/ Enhancer Reagent at a 1:1 ratio. Having added the ECL reagent to the membrane, the membrane was immediately imaged using the ChemiDoc XRS+ System (Bio-Rad) using the software, Imagelab software 6.01. Exposure times varied from 1 to 300 seconds. The image was exported for publication at 600dpi.

2.5. Microfluidics

A microfluidic device setup was employed to demonstrate the effects of a dynamic flow system on the expression of CBX2. The setup consisted of a PHD 2000 Infusion pump (Harvard Apparatus) held within a Perspex box with a removable door for easy access. A heater (Stuart Scientific) was attached to the roof of the box to maintain the temperature at 37˚C. Foil was placed around the box to help maintain a constant internal temperature. Similar continuous perfusion devices have been used successfully by Bower et al. (2017), Algarni et al. (2019), and Collins et al. (2021).

2.5.1. Microfluidic Chips

Microfluidic chips were prepared from Polymethyl methacrylate (PMMA) to the required specifications (Sennett, 2019). Individual sections of the chips were cut using a laser cutter, including the inlet and outlet segments, as well as the tissue chamber and filter (Figure 2.7). The chip design allowed for a hole to be drilled through the centre of each piece, which, when bonded together, ensured that a constant stream of media could pass through the chamber and around any spheroid that had been placed in the central chamber. Both the inlet and outlet pieces were designed with tapered holes allowing push-fit attachment to conventional Luer fittings which would connect the tubing to the chip, i.e., tapered ends facing the inlet and outlet of the chip.

The use of tapered ends ensured a tight seal, reducing/ preventing leaks. The filter piece provided a stoppage point, preventing the sample (in this case, spheroids) from leaving the chip, but allowed for media to flow with minimal resistance. The filter was orientated according to the tapered holes within the filter which were designed to become smaller towards the outlet.

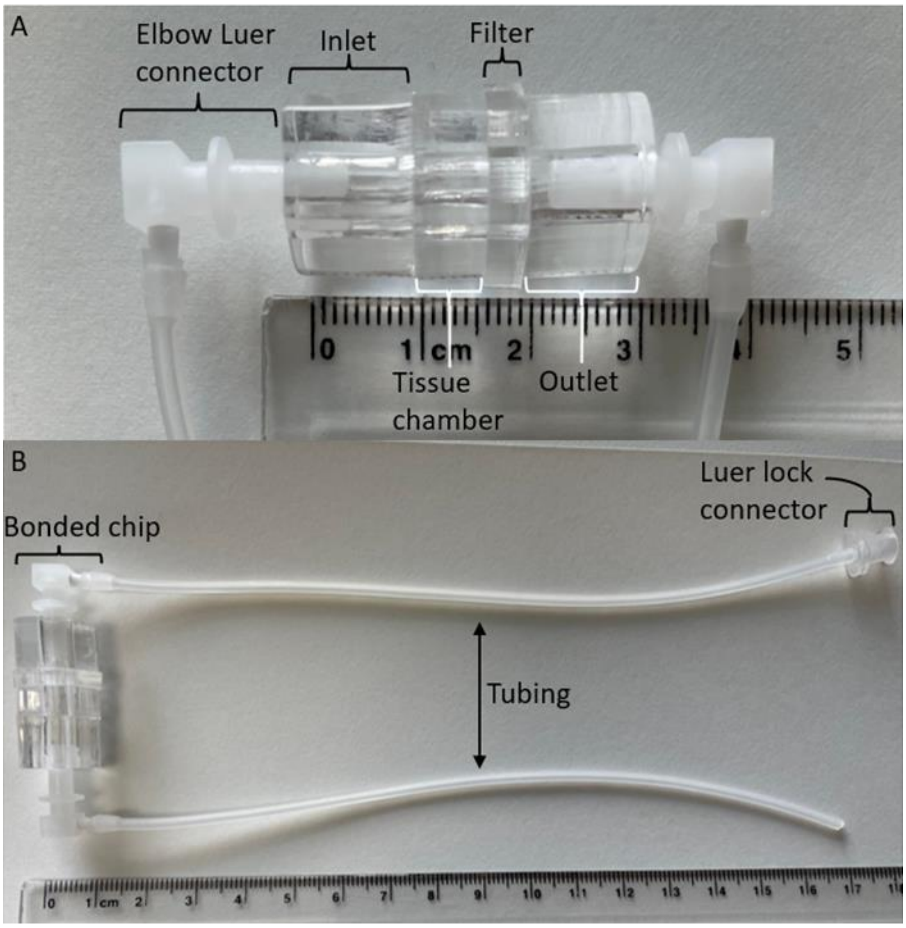

Figure 2.7. Microfluidic chip. (A + B) Bonded microfluidic chip, with components labelled.

Having obtained these sections as individual pieces, they were bonded together using chloroform (Figure 2.7); the bonding process for this chip was developed by Sennett (2019). Bonding of chips took place within a fume cupboard due to the use of chloroform. Using the tapered ends to ensure the pieces were aligned in the correct order, a minimal amount of chloroform was added to the surface of the inlet piece, being careful not to block the inner channel with the solvent. The tissue chamber was then carefully aligned to create the inner channel. The two pieces being bonded together were held in place for a minimum of 60 seconds; additional time or chloroform was required for secure bonding in some cases. This process was repeated until all segments were bonded together to form the assembled chip; extra care was taken to avoid blocking the small filter holes (100µm diameter) when adding chloroform. Finally, a few microlitres of chloroform was pipetted around the outer joints of the chip to reduce the chance of any leaks occurring. To ensure a tight seal, a weight was placed on top of the chips to prevent leaks; the chips were left for up to 72 hours to fully dry.

Silicone inlet and outlet tubes were used which were 1.6mm in diameter (Ibidi, Cat. No: 10842, Germany). To attach the tubing to the chip inlet and outlet segments, elbow Luer connecters (Ibidi, Cat. No: 10802) were used which ensured a tight seal (Figure 2.7).

Prior to use, the chips and tubing were tested for leaks. For this, the chips were assembled with the inlet and outlet tubes attached to the chip via the Luer connectors. The connectors were twisted tightly into place, then, using a 20ml Luer syringe (BD Plastipak™, Ref: 300613), 5ml of ddH_20 was flushed through the system slowly, allowing a steady stream of water to move through the device, to identify any leaks. If any leaks were found, additional chloroform was added to the chip and tested once again after allowing sufficient drying time. More often leaks were seen at the inlet and outlet sites, to prevent this, further tightening of the elbow Luer connector to the chip inlet and outlet ports was required. Once no leaks were detected, 5ml of 70% ethanol, followed by 5ml of ddH_20 was flushed through each chip and allowed to dry before being stored, ready for use.

2.5.2. Microfluidic Device Set-up

U-87 MG spheroids, prepared according to Section 2.1.3, with spheroids of 20,000 cells per/well, were allowed to grow for 72 hours before being placed in the device. The microfluidic chip set-up took place under sterile conditions within a Biological Class II safety cabinet (ESCO). Before the addition of any spheroids, the chips and tubing were again sterilised using ethanol; 5ml of 70% ethanol was rinsed through the chip slowly, again checking for leaks, followed by 5ml of ddH_20. A new syringe was then filled to the maximum level (past the 20ml mark) with fresh media, which had been warmed to 37˚C in a water bath; the media used was prepared for U-87 MG cells according to 2.1.1. The syringe was shaken gently to remove any air bubbles; to prevent bubbles from entering the spheroid chamber during the maintenance, a 0.22µm PES syringe filter (Sartorius) was added to the end of the syringe which was then attached to the inlet tube. To attach the syringe and filter, a Luer lock connector (Ibidi, Cat. No: 10825), suitable for 1.6mm tubing, was fitted to the inlet tubing. Media was then flushed through the chip until the chip and tubes were filled.

Still in a Biological Class II safety cabinet, the spheroids were loaded into the tissue chamber of the chips; 3 spheroids per chip were loaded, with 4 chips used per experiment. To achieve this, the outlet tube was held above the inlet entrance to the chip to prevent media from leaving the system. The inlet tube was then detached from the chip and the spheroids were added one at a time to the chip, using a pipette. To ensure that no/ minimal bubbles entered the system, a drop of media was allowed to hang from the end of the inlet tube, before being reattached to the chip inlet entrance. The inlet tube Luer connector was twisted into the chip inlet entrance tightly so as to create a tight seal (as with the outlet tube Luer connector). The majority of leaks seen were located between the Luer connectors and the chip inlets and outlet channels, and as such, extra care was taken to prevent this when setting up the chip. Media was pushed through the chip slowly until 20ml of media remained in the syringe. This process was repeated until 4 chips were prepared. Collection tubes were then prepared using 50ml screw cap tubes; a hole was punched through the screw cap of each tube using metal forceps, wide enough to allow the outlet tube to be pushed through.

Once the spheroids were placed in the microfluidic device and the Luer connectors in place the spheroids can be classed as being held within an enclosed system. As such, the microfluidic device could be removed from the sterile hood whilst the spheroids remained in a sterile environment within the chips. The syringes were then loaded onto the pump located within the incubated cabinet and locked into place. The chips were secured in the correct orientation, with the inlet at the top and the outlet at the bottom to help with the flow of media through the chip. The outlet tubes were placed in the collection tubes, enabling the perfused media to be collected. The perfusion rate of the media was set to 2µl/ minute on the syringe pump (Riley et al., 2021). Once set-up was complete (Figure 2.8), the pump was set to infuse, and the microfluidic experiment was run for 96 hours.

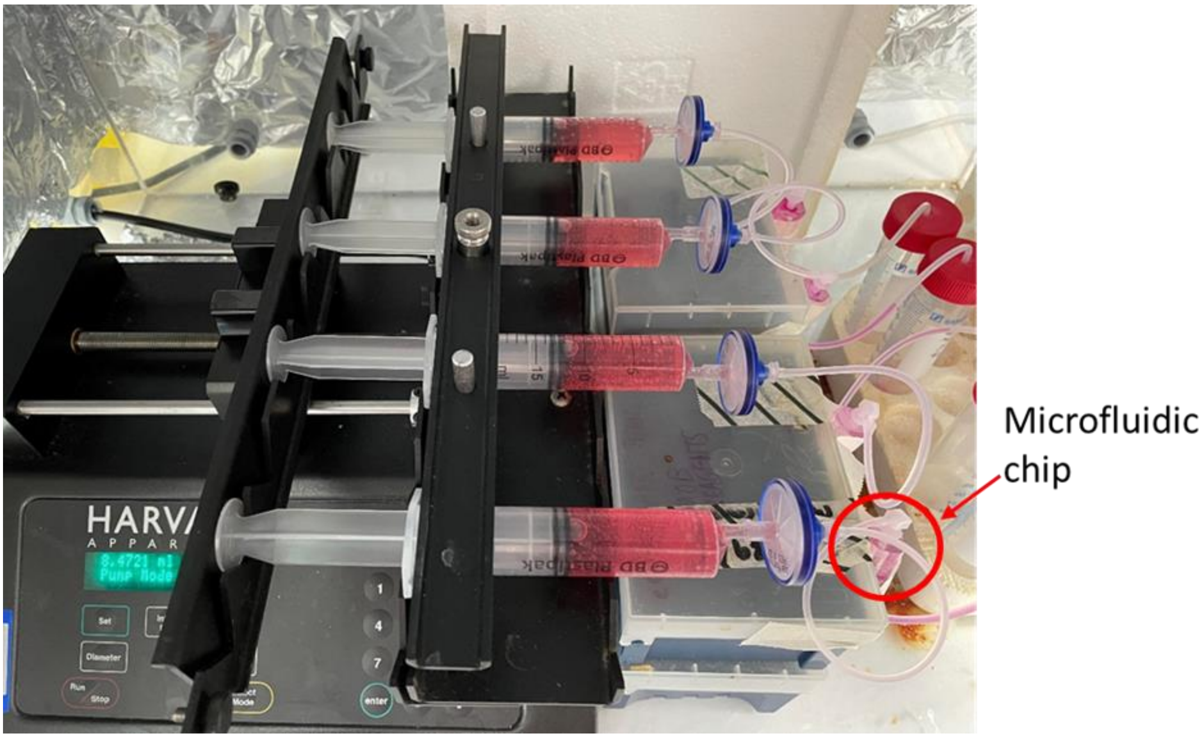

Figure 2.8. ***Microfluidic device set-up. Prepared media held in syringes being perfused across the microfluidic chips at 2 µl/minute. Perfused media collected in 50ml tubes. Microfluidic chip highlighted.***

Following the 96 hour run period, the microfluidic chips were removed from the box and placed back in the Class II cabinet for disassembly and collection. The spheroids from all 4 chips were collected and placed in the same 1.5ml Eppendorf tube. The media was then pipetted out of the Eppendorf collection tubes, leaving only the spheroids. To ensure all the media was removed, PBS was added to the spheroids and used to gently wash the samples before being removed by pipette. The spheroids were then ready for RNA extraction for future analysis using RT-qPCR (as outlined in Section 2.6).

The microfluidic chips and tubes were disinfected in 2% (w/v) Virkon for a minimum of 24 hours before being rinsed with ddH_20, followed by 70% ethanol. The chips were allowed to air dry before being stored for later use.

2.5.3. Static Experiments

Static experiments were completed using U-87 MG spheroids, prepared according to Section 2.1.3, with spheroids of 20,000 cells/ well grown for 72 hours before use. These spheroids remained within the ULA plates for a further 96 hours following the initial 72 hour growth period. Fresh media was added after the first 72 hour incubation, with media changed and replaced with fresh media after another 48 hours. Two static models were used. One static model utilised 1 spheroid per well, with the second model using 3 spheroids per well; the latter was considered a better mimic of the inner chamber conditions of the microfluidic chip. A total of 12 spheroids were maintained and collected for each model, per experiment.

After the 96 hour incubation period, the two sets of spheroids were collected and placed in two separate Eppendorf tubes: 12 spheroids in each tube. The spheroids were then handled as described above for the spheroids collected from the microfluidic chips (Section 2.5.2.), ready for RNA extraction and RT-qPCR analysis.

2.6. RT-qPCR

Following RNA extraction, Reverse Transcription (RT) followed by quantitative Polymerase Chain Reaction (qPCR) was performed so as to determine the mRNA expression of CBX2, RBL2, and Ribosomal protein L13a (RPL13A) in a variety of 2D and 3D experiments. Previous work in the laboratory of one of the supervisors has shown that RBL2 is increased when CBX2 expression is deceased, thus showing the downstream effects of CBX2, similarly RPL13A was used as a reference gene (Bilton et al., 2022). Including, following siRNA knockdown and after overexpression in static culture, as well as following static vs. microfluidic experiments. Two-step RT-qPCR was utilised in which RT was conducted separately from qPCR. RT was employed in order to reverse transcribe RNA into complementary DNA (cDNA). The cDNA generated was then used in RT-qPCR.

2.6.1. RNA Extraction

The 2D cells and spheroids collected from siRNA knockdown, overexpression, and microfluidic experiments were taken for RNA extraction. RNA extraction was performed using a RNeasy Mini Kit (Qiagen, UK), as per the manufacturer's instructions; the same RNA extraction kit was used previously by Stangegaard et al. (2006) and Kauther et al. (2010) to the same effect.

As per the instructions provided with the kit, the appropriate volume of Buffer RT was added to the cell pellet or spheroids. For samples with less than 5×10^6 of cells, 350µl of Buffer RT was added, if more than 1×10^7 cells were present, 600µl of Buffer RT was used. All samples used in this project required the addition of 350µl of Buffer RT; this buffer lysed the cells prior to RNA isolation. Once homogenised by pipetting, the samples were centrifuged at maximum speed for 3 minutes in a GenFuge 24D minicentrifuge (Progen, UK) at room temperature; all steps which required centrifugation used the GenFuge 24D minicentrifuge. Following centrifugation, the supernatant was removed and retained, and the pellet discarded. To the supernatant, an equal volume of 70% ethanol was added and homogenised (350µl). Once homogenised, 700µl of the sample was loaded into the spin columns provided with the RNeasy Mini Kit, and then centrifuged at 8000 x g for 15 seconds. The flow-through was discarded and 700µl of Buffer RW1 was then loaded into the spin column before the column was centrifuged again at 8000 x g for 15 seconds; Buffer RW1 was used for the purpose of washing the membrane-bound RNA. Once the flow-through was discarded, 500µl of Buffer RPE was added to the spin column before the sample was centrifuged at 8000 x g for 15 seconds, after which any flow-through was also discarded; Buffer RPE was used to further wash the membrane-bound RNA. An additional 500µl of Buffer RPE was added to the spin columns before they were centrifuged for 1 minute at 8000 x g. The spin column was then placed in a new Eppendorf collection tube and 50µl of RNase free water was added before centrifugation at 8000 x g for 1 minute. Once RNA was eluted from the column on the final run in the minicentrifuge, the RNA was placed on ice.

The RNA concentration of each sample was verified immediately following isolation using a NanoDrop™ 2000 Spectrophotometer (Thermofisher, UK), with the data produced analysed using NanoDrop 2000/ 2000c software, 2009 - 2014 (Thermofisher, UK); analysis was performed prior to freezing to improve the accuracy of RNA concentration readings. Using molecular grade water as the blank, 1.5µl of the RNA samples were loaded onto the Nanodrop for analysis; RNA concentration results were given as ng/µl. The purity of the samples can also be observed through the 260/280 ratio; the absorbance of the sample is measured at 260nm and 280nm to determine the RNA purity. The desired purity ratio should be within the range, 1.8-2.2, with a ~2.0 ratio considered to be 'pure' RNA (Thermo-Scientific, 2012).

For short term storage, of less than 2 weeks, RNA samples were stored at -20˚C; for long-term storage of more than 2 weeks, RNA samples were stored at -80˚C.

2.6.2. Reverse Transcription

Once RNA had been isolated from the cell pellet, RT was performed as part of the first step of the Two-step RT-qPCR process. cDNA was obtained from the mRNA samples; for use in the second part of RT-qPCR.

Using the results obtained from the NanoDrop following RNA extraction, the volume of sample required to generate 1µg of cDNA was calculated (example below).

Formula:

$$\frac{1000ng}{x\ ng/\mu l} = \cdots\ \mu l\ (volume\ of\ mRNA\ sample\ required\ to\ give\ 1\mu g\ of\ cDNA)$$

Example:

If the sample concentration is $104.7 ng/\mu l$

$$\frac{1000}{104.7ng/\mu l} = 9.55\ \mu l\ (of\ mRNA\ needed)$$

When making cDNA from RNA, the RNA samples were collected from -80˚C stores, allowed to thaw on ice, and vortexed. The volume of sample required, calculated using the equation above, was pipetted into a fresh 1.5ml Eppendorf, and made up with molecular grade water to 12.7µl. To this, the RT mastermix was then added. The mastermix employed for RT contained 5x buffer (Promega, UK), dNTP (10mM stock, Thermo Scientific), oligodT (50µM stock, Invitrogen), and Reverse Transcriptase (Promega), see Table 2.8. for volumes used. Once prepared, 7.3µl of the mastermix was then added to each 12.7µl sample, to give a total of 20µl, and pipetted gently to mix. Samples were then incubated at 37˚C for 1 hour using a digital dry bath (Labnet, USA) – Eppendorf tubes were sealed with Parafilm to prevent evaporation of samples.

Table 2.8. Reagents used for RT with concentrations and volumes used.

Reagent	Volume used per sample
5x buffer	4µl
4mM dNTP	2µl
10µM oligodT	1µl
Reverse Transcriptase (200µ/µl)	0.3µl

Following incubation, the samples were then held on a heat-block for 5 minutes at 90-100˚C to stop the reaction. To ensure that no sample was lost, sample tubes were briefly centrifuged to collect any sample that had condensed in the lid during incubation. To the samples, 180µl of molecular grade water was added to give a total of 200µl. After which, the cDNA samples were ready for use in the second step of the RT-qPCR reaction. If being used immediately, the cDNA samples were kept on ice, however, for long term storage, cDNA samples were stored at -20˚C.

2.6.3. qPCR

Using the cDNA produced following RT of RNA samples, the second step of RT-qPCR was conducted. When preparing RT-qPCR, all samples and reagents were kept on ice. A new mastermix was prepared for qPCR, with the reagents used including, SYBR® Green JumpStart™ Taq ReadyMix™, with Taq polymerase added (Merck, Germany), ROX dye (as the reference dye) (Merck), and specific forward and reverse primers. The volumes of reagents used in the mastermix are shown in Table 2.9, and the primer sequences displayed in Table 2.10. The primers used were specific for RPL13A as the reference sequence, CBX2, and RBL2; the effectiveness of RPL13A as a reference gene has previously been analysed in relation to GBM (Aithal & Rajeswari, 2015).

Table 2.9. Reagents used for qPCR Mastermix with volumes used.

Reagent	Volume used per sample
SYBR green with Taq polymerase	5µl
ROX dye (reference dye)	0.1µl
Molecular grade water	2.1µl
Forward primer	0.4µl
Reverse primer	0.4µl

Table 2.10. mRNA Primer forward and reverse sequences.

Primer	Primer Sequences, 5’ – 3’		Purchased from
	Forward	Reverse	
RPL13A	CCTGGAGGAGAAGAGGAAAGAGA	TTGAGGACCTCTGTGTATTTGTCAA	Sigma-Aldrich®, UK
CBX2	GCTCCAAAGCCAGACTAACA	CAGGGACAGACATCCTCATTTC	Integrated DNA Technologies (IDT), Belgium
RBL2	CCTAGTTTTGGAAGCAAAGG	AAAACTCTCTCCAAAGTTCC	Merck

Reagents were added to a MicroAmp™ Fast Optical 96-Well Reaction Plate (Applied Biosystems™, UK). Through pipetting, 8µl of each prepared Mastermix was loaded into the bottom of the designated wells. The cDNA samples were defrosted on ice and vortexed prior to use; 2µl of cDNA sample was loaded onto the side of each well. A control sample, dH$_2$0, was also used in addition to the cDNA samples. Three wells of each sample per primer set were prepared. The loading pattern for each MicroAmp™ plate can be seen in Figure 2.9. The plate was then secured using a MicroAmp™ Optical Adhesive Film (Applied Biosystems™, UK), after which, the plate was briefly centrifuged at a maximum speed of 2,500 RPM/ 500 x g using a MPS 1000 Compact Mini Plate Spinner Centrifuge (Labnet, USA). The plate was then ready for RT-qPCR analysis.

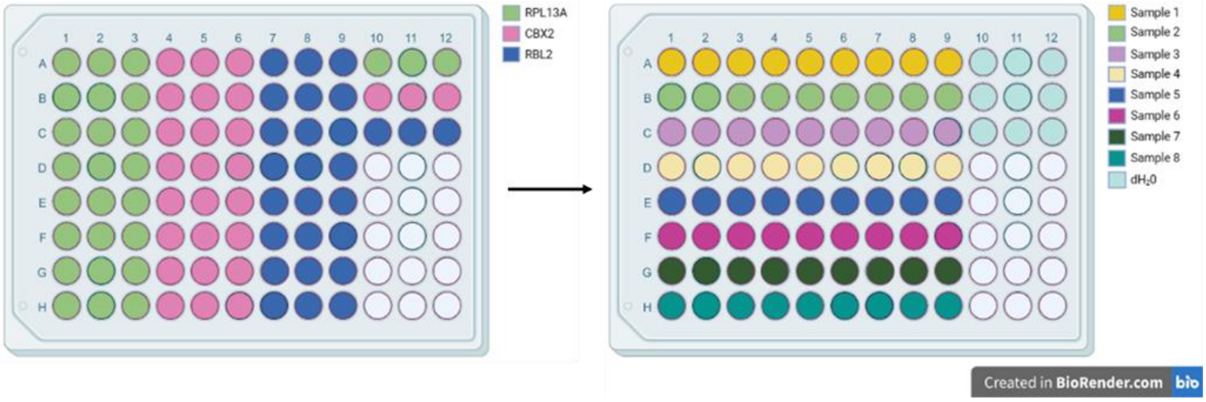

Figure 2.9. Visual representation of the loading pattern for the RT-qPCR analysis when analysing 8 samples. (Left) Loading pattern for the three primer Mastermix's used: RPL13A, CBX2, and RBL2. Primers loaded in triplicate. (Right) Loading pattern for the cDNA samples, when 8 samples were used. In addition to the 8 samples of cDNA, a control sample of dH$_2$0 was also used. Figure produced using Biorender.

The software, StepOne software v2.0 was used in conjunction with the StepOne Plus Real-time system from Applied Biosystems as the mechanism for which RT-qPCR was conducted. System set-up for running: Quantitation-comparative Ct (Delta-Delta Ct; ΔΔCt), SYBR green reagents (with melt curve), standard 2 hour ramp speed, as well as cDNA Two-step RT-qPCR. Additionally, the sample size was selected at 10µl. Following this, the plate setup option was selected to add identifiers to each well to allocate the names of the primers and samples used, as modelled in Figure 2.9. Once setup was completed and the plate added to the machine, the experiment was run for the programmed 2 hours as per the PCR cycle set-up (Table 2.11.). Once the experiment run was finished, the results of each well were observed. The 3 repeats of each sample were analysed, with any anomalous results omitted. These results were then exported to an Excel spreadsheet, and the Ct mean results used to calculate the expression fold change of the genes after siRNA knockdown, overexpression, and growth in static and microfluidic and environments to identify if gene expression has been altered. For this, the housekeeping gene, RPL13A, was used to normalise cDNA levels between samples. Following this step, all expression fold change results were then calculated relative to the siScr sample for the siRNA knockdown experiments, or relative to the pFLAG sample for the overexpression experiments, or indeed to the static (1 spheroid/ well) sample for the static vs. microfluidic experiments. From which the expression fold change can be calculated.

Table 2.11. PCR cycle.

PCR cycle step		Temperature	Time
Holding stage		95°C	10 minutes
Cycling stage; 40 cycles.	**1. Denaturation**	95°C	15 seconds
	2. Annealing	60°C	1 minute
	3. Elongation	72°C	1 minute
Melt curve stage		95°C 60°C 95°C	15 seconds 1 minute 15 seconds

The following calculations were used to calculate the expression fold change of experimental samples when compared to the control. Where ‘Control’ refers to siScr, for example.

$$\begin{aligned}\Delta\Delta Ct = {} & (\Delta Ct(sample) - \Delta Ct(control)) \\ & - (\Delta Ct(RPL13A\ of\ sample) - \Delta Ct(RPL13A\ of\ control))\end{aligned}$$

$$Expression\ fold\ change = 2^\wedge(-\Delta\Delta Ct)$$

Example of calculation for expression fold change of siCBX2 #1 against siScr, results rounded at the end:

$$\begin{aligned}\Delta\Delta Ct = {} & (31.31735039 - 31.41731071) - (19.45707703 - 19.15807343) \\ = {} & -0.398963928\end{aligned}$$

$$Expression\ fold\ change = 2^\wedge(- - 0.398963928) = 1.318560646 = 1.31\ (2\text{dp})$$

As shown above, 1.31 refers to the expression fold change of mRNA levels of CBX2 of siCBX2 #1 treated samples compared to the siScr control following siRNA CBX2-targeted knockdown, where expression of siScr is 1.

Chapter 3: Results

3.1. siRNA Knockdown

3.1.1. 2D Model

During the investigation of the role of CBX2 on GBM cell lines, the morphological effects on the cells was analysed following siRNA knockdown of the mRNA for this gene in a 2D model. The effects of siRNA knockdown on U-87 MG cells can be seen in Figure 3.1, testing three different siRNA sequences specific for CBX2 alongside a scrambled control siRNA. Microscopic images were taken after 72 hours of incubation and prior to collection of the cells. Visually, the siRNA which had the most effect were siCBX2 #3 and #4, with siCBX2 #4 showing the greatest reduction in cell number. A second observation was that the cells treated with the control, scrambled siRNA, as well as cells treated with siCBX2 #1 formed discernible cell clusters (Figure 3.1). Cells transfected with siCBX2 #3 and #4 did not show these clusters, with larger gaps being observed between the cells treated with siCBX2 #4.

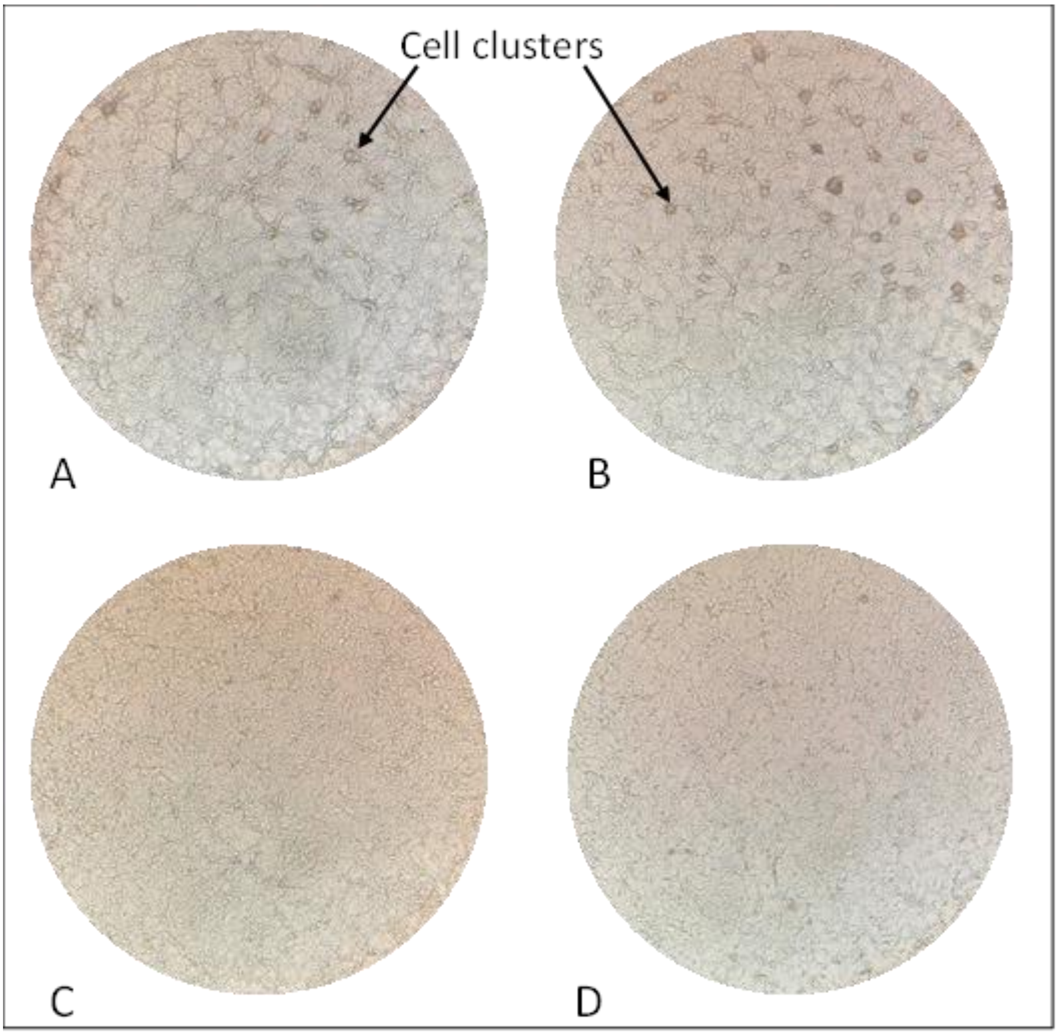

Figure 3.1. Microscopic images taken of U-87 MG cells which have undergone transfection. Using the siRNA knockdown agents, siScr, and siCBX2 #1, 3, and 4, in the 2D model. Images taken 72 hours post-setup at 10x magnification, prior to collection. A) siScr, B) siCBX2 #1, C) siCBX2 #3, D) siCBX2 #4. Cell clusters highlighted using arrows. (n=6; 6 independent experiments).

Similar microscopic images were taken of the SNB-19 cell line following 2D siRNA knockdown, after 72 hours incubation (Figure 3.2). The morphological effects of CBX2 knockdown were less apparent in the SNB-19 cell line, compared with the U-87 MG cell line. The cells appeared to grow evenly and were packed tightly in all wells, however there were small gaps between the siCBX2 #4 transfected cells. There was a visual increase in the number of dead cells for both U-87 MG and SNB-19 cells with siCBX2 #4, with the SNB-19 cells showing the greatest number of dead cells floating in the media.

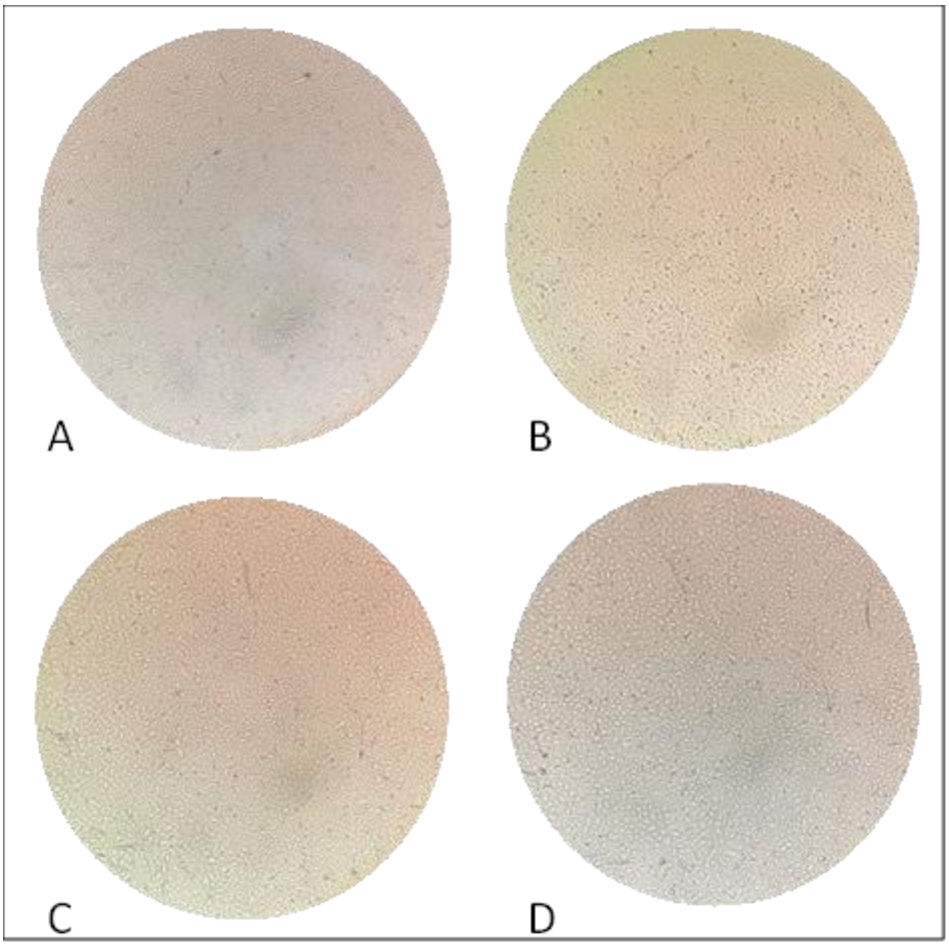

Figure 3.2. Microscopic images taken of SNB-19 cells which have undergone transfection. Using the siRNA knockdown agents, siScr, and siCBX2 #1, 3, and 4, in the 2D model. Images taken 72 hours post-setup at 10x magnification, prior to collection. A) siScr, B) siCBX2 #1, C) siCBX2 #3, D) siCBX2 #4. (n=6; 6 independent experiments).

In addition to microscopic images, cells were counted following collection to quantify the effect of CBX2 knockdown on cell growth and number. Cells were counted for each siRNA agent across each repeat experiment; the cell count averages for the siRNA transfections for U-87 MG and SNB-19 are shown in Figure 3.3.A and Figure 3.3.B, respectively. In both cell lines, the siCBX2 caused a reduction in cell number, when compared to the siScr treated cells, with siCBX2 #4 providing the greatest reduction in cell number for both cell lines, with a *p-value* of *0.0049* for the change in cell number.

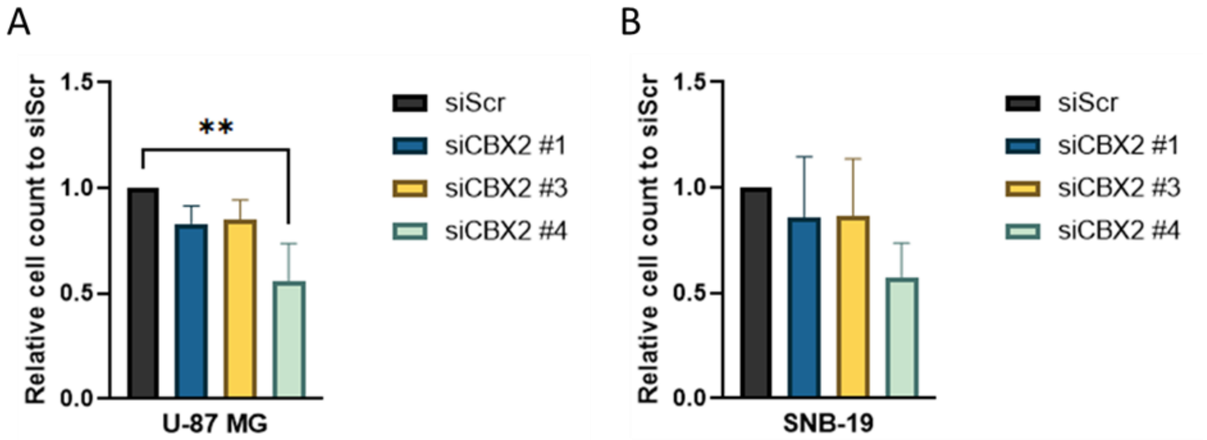

Figure 3.3. Average cell count observed for each siRNA used following 2D siRNA knockdown on U-87 MG and SNB-19 cells. The cell counts of siScr and siCBX2 #1, 3, and 4 each made relative to the siScr transfected cells. (A) Cell count of U-87 MG cells following siRNA knockdown. (B) Cell count of SNB-19 cells following siRNA knockdown. Mean calculated from repeats, n=3; refers to 3 independent experiments for each cell line. Error bars show the standard deviation. Ordinary one-way ANOVA was performed. Unless stated otherwise, p-values were determined by Tukey's multiple comparisons test for all graphs (**denotes $p < 0.01$).

The effect of CBX2 siRNA knockdown on U-87 MG and SNB-19 protein expression in a 2D model was analysed using western blotting (Figure 3.4). For this, cells were lysed, and the protein concentration of samples determined through a BCA assay (Section 2.4); 100µg of protein was loaded into the well for each cell lysate. The ladder, Precision Plus Protein Dual Color Standard, was used to identify the molecular weight (MW) of each band, for each sample. A polyclonal anti-CBX2 specific antibody was used to visualise the bands and compare CBX2 expression between the lysates (Section 2.4). Despite multiple repeats of the 2D siRNA knockdowns on both the U-87 MG and SNB-19 cell lines, the resulting western blots, despite using fresh reagents, different equipment, and fresh samples and antibodies, showed no bands for any of the siRNA transfected cells. Consequently, the results, as seen in Figure 3.4, could not be repeated in the 2D model.

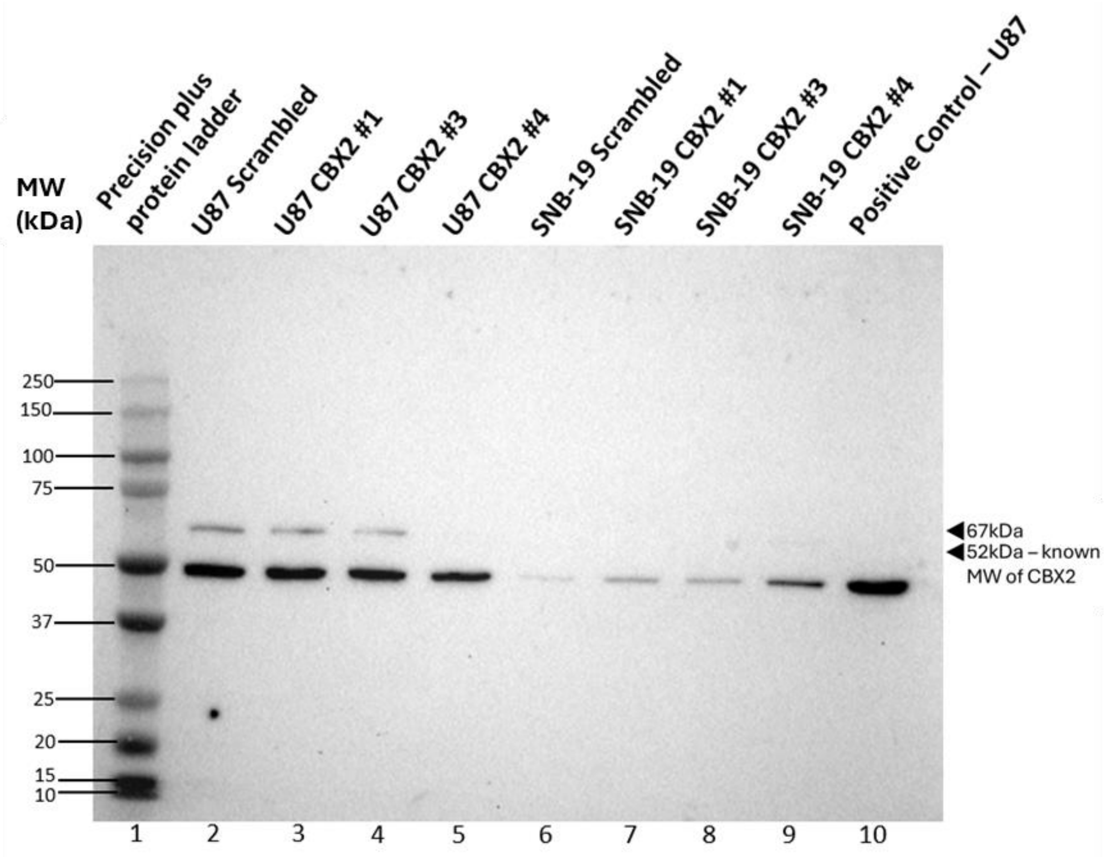

Figure 3.4. Western blot of U-87 MG and SNB-19 cell protein lysates collected from 2D siRNA knockdown experiments, incubated with CBX2 antibody. Cells transfected with the siRNA's, siScr, siCBX2 #1, 3, and 4. The bands produced are representative of CBX2 expression within each lysate following transfection. The ladder used was the Precision Plus Protein Dual Color Standard; molecular weight (MW) of bands measured in kilodaltons (kDa). A U-87 MG lysate was loaded into well 10 for comparison between gels as a positive control and was loaded at the same protein concentration as the samples analysed, 100µg. All western blots used the same protein ladder as well as the same positive control. (n=1).

The same western blot, loaded with U-87 MG and SNB-19 2D siRNA knockdown lysates, was also incubated with Glyceraldehyde 3-phosphate dehydrogenase (GAPDH) to check for protein expression (Figure 3.5) and to enable densitometry analysis. Crucially, GAPDH protein expression was shown to be easily reproducible and consistent across many experimental repeats.

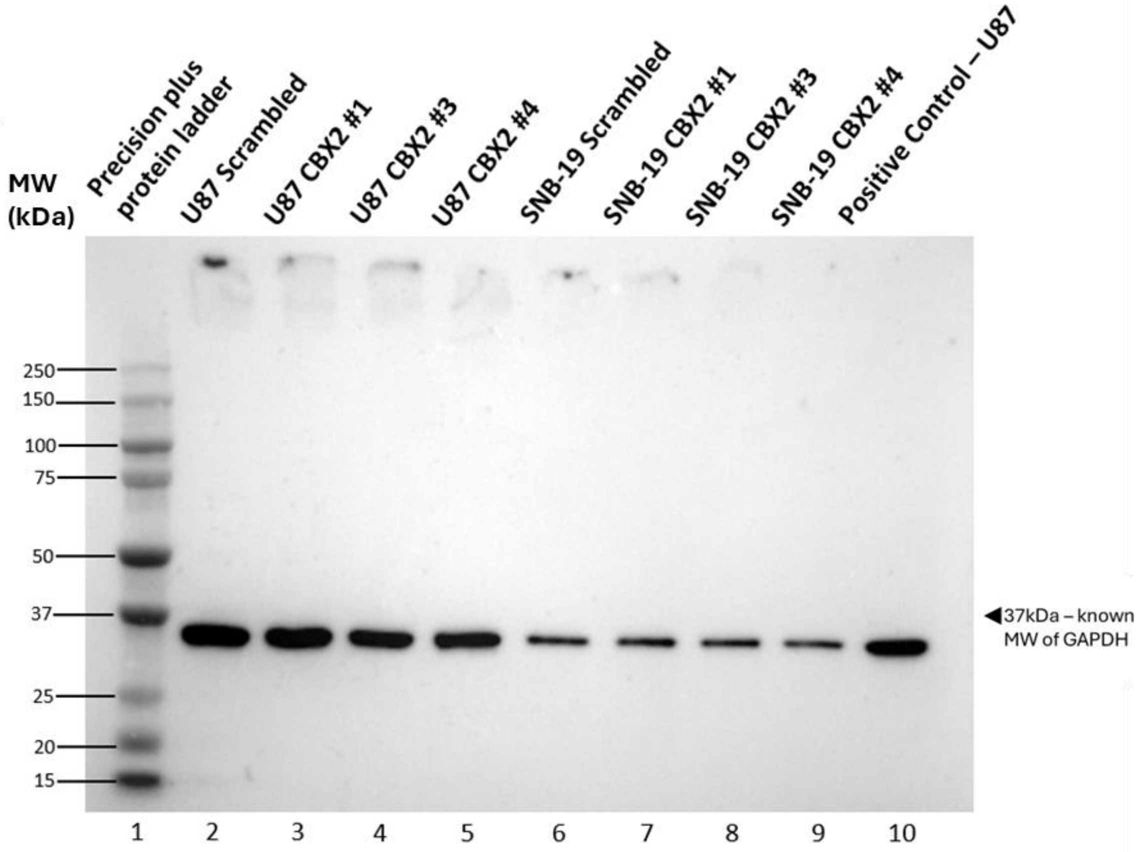

Figure 3.5. Western blot of U-87 MG and SNB-19 cell protein lysates collected from 2D siRNA knockdown experiments, incubated with GAPDH antibody. Cells transfected with the siRNA's, siScr, siCBX2 #1, 3, and 4. A U-87 MG lysate was loaded into well 10 for comparison between gels as a positive control. The bands present are representative of GAPDH expression within each lysate following transfection (n>6).

The densitometry of the bands was calculated from the CBX2 and GAPDH incubated western blots to compare CBX2 protein expression (Figure 3.6.A for U-87 MG densitometry and Figure 3.6.B for SNB-19 densitometry). There was a slight decrease in band density between siScr and siCBX2 #4 for the U-87 MG cells. As illustrated in the western blot (Figure 3.4), the band density for the SNB-19 cells increased from the siScr treated cells to the siCBX2 transfected cells, with siCBX2 #4 showing the greatest increase in band density when analysed through densitometry (Figure 3.6.B).

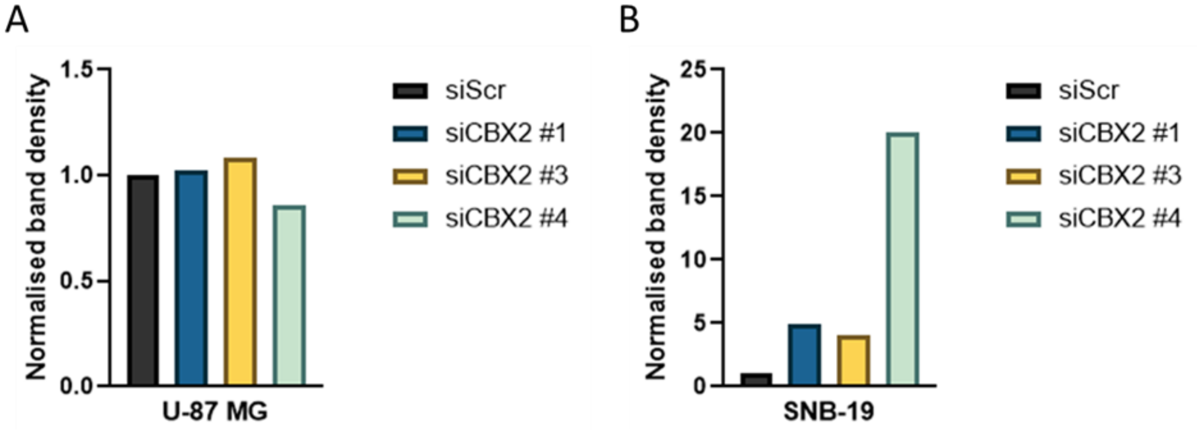

Figure 3.6. Densitometry results from U-87 MG and SNB-19 2D siRNA knockdown western blot. Band density of CBX2 was normalised against the control. GAPDH incubated western blot bands were used as the control. (A) Normalised band density of U-87 MG cells following 2D siRNA knockdown. (B) Normalised band density of SNB-19 cells following 2D siRNA knockdown. (n=1).

CBX2 expression of the cells which had undergone 2D siRNA knockdown was also analysed using RT-qPCR, following RNA extraction (RNA extraction and RT-qPCR outlined in Section 2.6). RT-qPCR was performed using CBX2, RBL2, and RPL13A primers; RPL13A was used as the control/ housekeeping gene, to which CBX2 and RBL2 expression was compared. The expression of RBL2 was analysed due to hypothesised links between CBX2 and RBL2. As CBX2 takes part in histone modification, causing gene silencing, it is thought that one of the targets for this silencing is tumour suppressors, such as RBL2.

The greatest reduction in expression of CBX2 in the U-87 MG cell line was with the siCBX2 #4 siRNA (Figure 3.7.A), with siCBX2 #1 apparently causing an increase in CBX2 expression levels. The expression of RBL2 in the 2D siRNA knockdown of the U-87 MG cell line was seen to increase in all siCBX2 variants, with siCBX2 #1 showing the greatest increase in expression fold change at 1.87 when made relative to siScr (Figure 3.7.B).

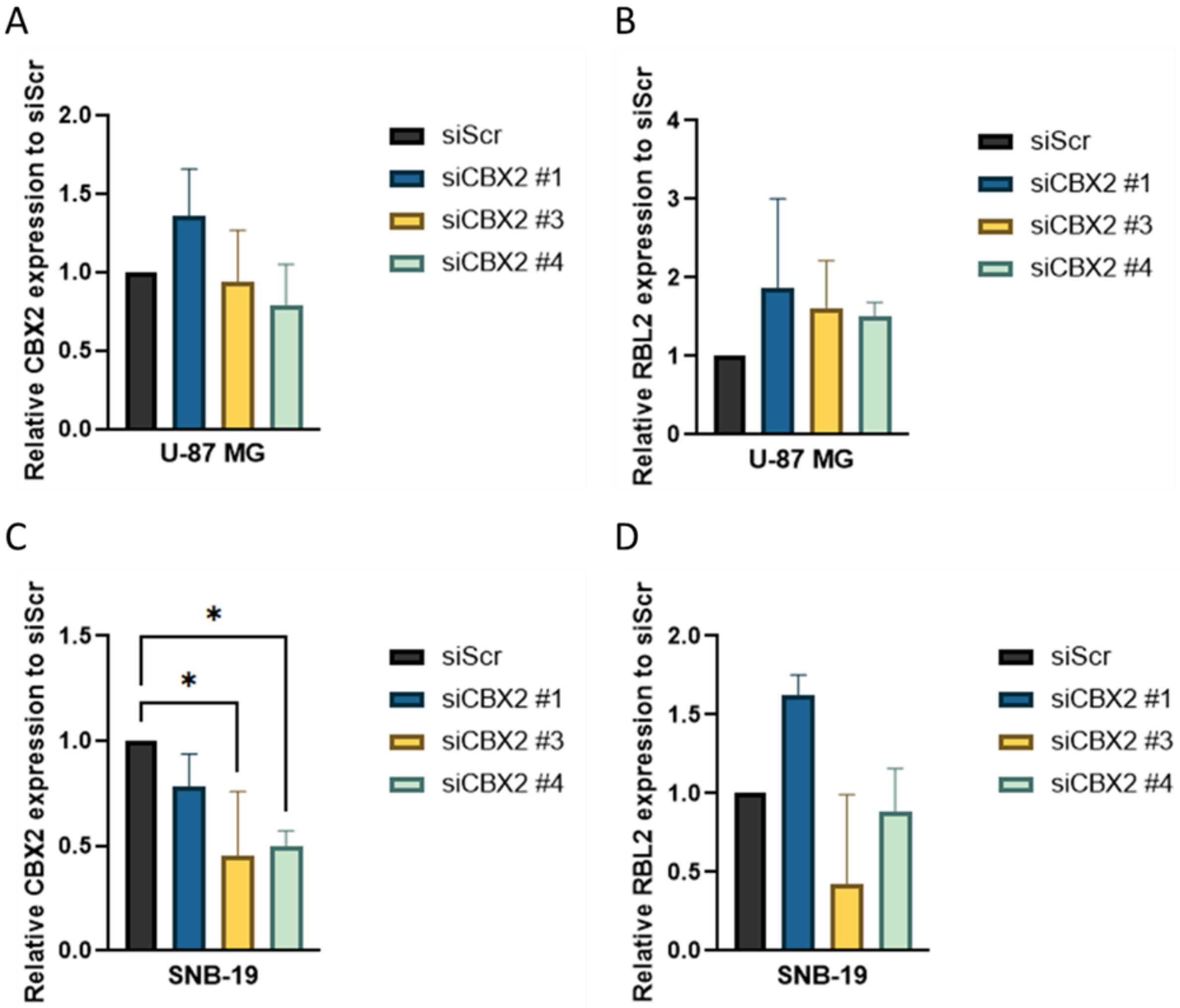

Figure 3.7. RT-qPCR results of 2D siRNA knockdown of U-87 MG and SNB-19 cells. Analysing the expression of CBX2 and RBL2 following transfection of siScr, siCBX2 #1, 3, and 4. Expression fold change was against RPL13A as the control gene. Expression fold change of siCBX2 #1, 3, and 4 were each made relative to siScr. (A) CBX2 expression in U-87 MG. B) RBL2 expression in U-87 MG. C) CBX2 expression in SNB-19. D) RBL2 expression in SNB-19. Mean calculated from repeats, n=3 for all except graph D, for which one outlier was discounted and therefore n=2. Error bars show the standard deviation. Ordinary one-way ANOVA performed (*denotes $p < 0.05$).

The expression fold change of the SNB-19 cell line following RT-qPCR of 2D siRNA knockdown samples exhibited a decrease in CBX2 expression in all types of siCBX2 used when compared to siScr, with siCBX2 #3 showing the greatest reduction on average (Figure 3.7.C). The change in RBL2 expression between the different siCBX2 agents used was variable, when applied to SNB-19 cells; although not statistically significant, siCBX2 #1 initiated an increase in RBL2 expression following transfection, whereas siCBX2 #3 and 4 reduced RBL2 expression (Figure 3.7.D).

Due to an outlier identified with one of the repeat sets for the 2D siRNA knockdown in the SNB-19 cell line with the RBL2 primer, one set of results was discounted from the average: Figure 3.8 shows the RT-qPCR results for this experiment with the outlier results included within the average expression fold change.

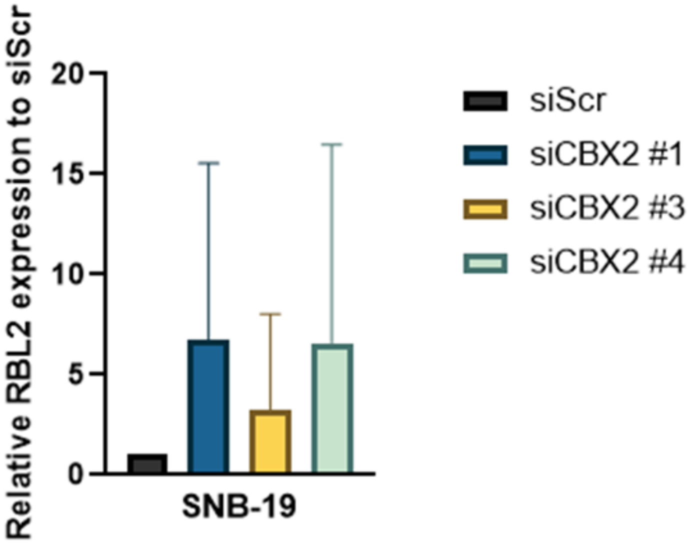

Figure 3.8. RT-qPCR results of 2D siRNA knockdown on SNB-19 cells analysing RBL2 expression. Expression fold change was calculated against RPL13A as the control. Expression fold change of siCBX2 #1, 3, and 4 were each made relative to siScr. Illustrates RBL2 expression fold change in SNB-19 cells with n=3, including the outlier repeat set. Mean calculated from repeats. Error bars show the standard deviation. Ordinary one-way ANOVA performed.

3.1.2. 3D Model

Continuing the investigation of the role of CBX2 on GBM cell lines, the effects of siRNA knockdown on U-87 MG and SNB-19 cells was also explored in a 3D model, namely, spheroids. The morphological effects of siRNA knockdown on U-87 MG spheroids can be seen in Figure 3.9. Images were taken after 96 hours of incubation and prior to collection, using a Gelcount.

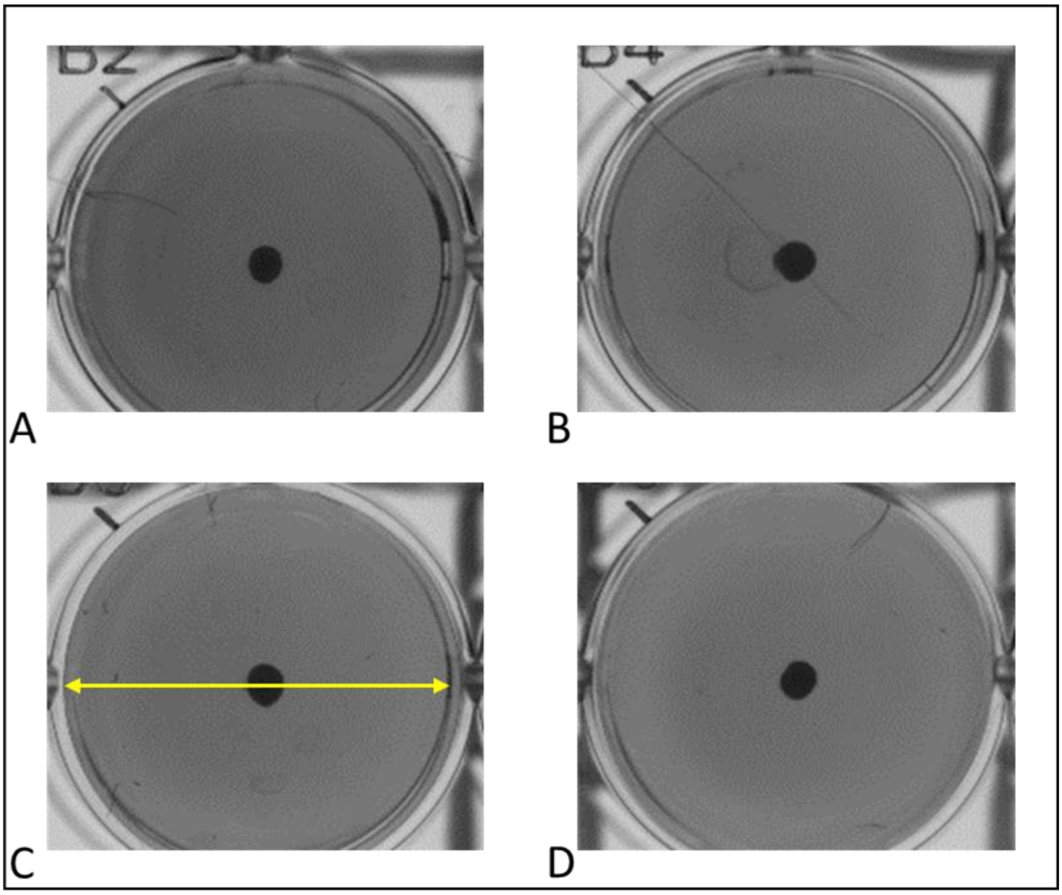

Figure 3.9. Images taken of U-87 MG spheroids which have undergone transfection. Using the siRNA knockdown agents, siScr, and siCBX2 #1, 3, and 4. Images taken 96 hours post-setup, prior to collection using a Gelcount. The yellow arrow indicates the diameter of each well, which is 6.8mm, which was used as the scale for which the spheroids were measured against. U-87 MG spheroids ranging in diameter from 0.59mm to 0.85mm. A) siScr, B) siCBX2 #1, C) siCBX2 #3, D) siCBX2 #4. (n=72; 6 independent experiments, with 12 spheroids imaged per siRNA agent for each run).

The same images were taken of the SNB-19 cell line following 3D siRNA knockdown, after 96 hours of incubation (Figure 3.10).

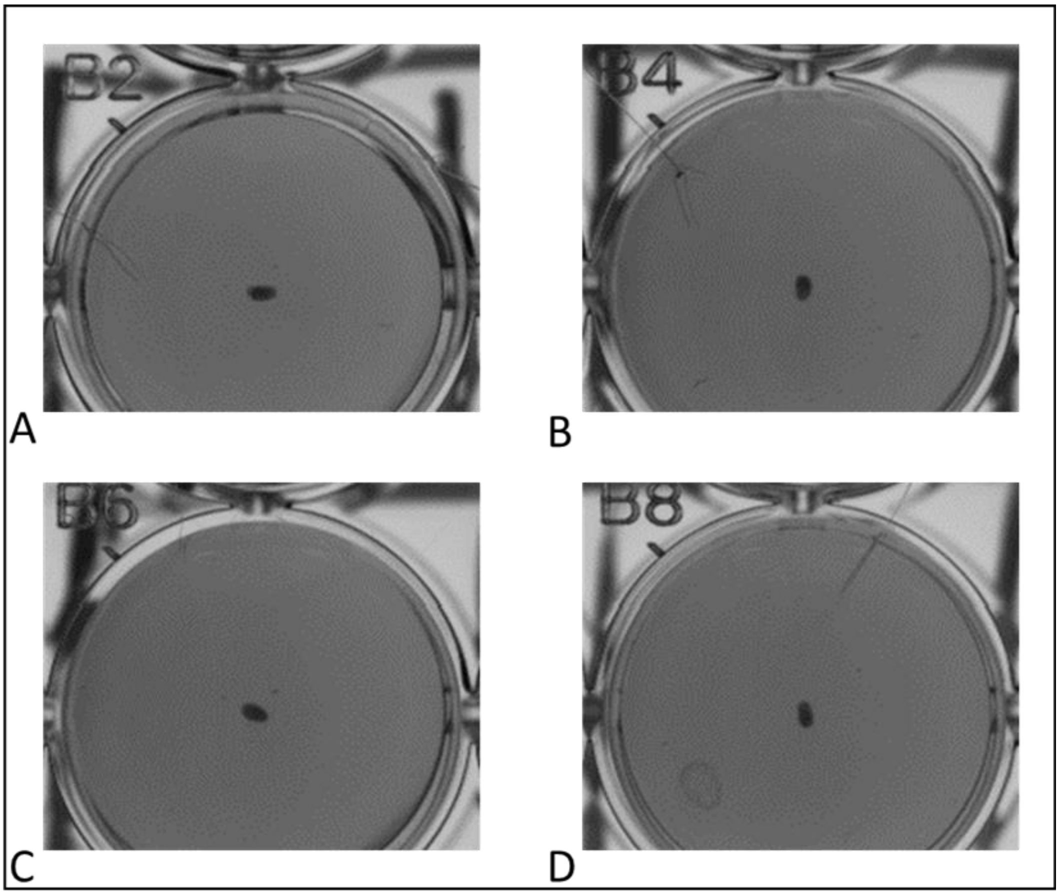

Figure 3.10. Images taken of SNB-19 spheroids which have undergone transfection. Using the siRNA knockdown agents, siScr, and siCBX2 #1, 3, and 4. Images were taken 96 hours post-setup, prior to collection using a Gelcount. SNB-19 spheroids ranging in diameter from 0.37mm to 0.55mm. A) siScr, B) siCBX2 #1, C) siCBX2 #3, D) siCBX2 #4. (n=72; 6 independent experiments, with 12 spheroids imaged per siRNA agent for each run).

Whilst the effects of siRNA transfection are not as apparent as in the 2D model, spheroid diameter analysis was completed in the place of cell counting, to determine the effect on cell growth after the addition of each siRNA; the spheroid diameter averages for the siRNA transfections for U-87 MG and SNB-19 are shown in Figure 3.11.A and Figure 3.11.B, respectively. Transfection with CBX2 targeting siRNA's did not significantly change the diameter of the spheroids compared to the scrambled siRNA. For the U-87 MG spheroids, the largest reduction observed was seen following 168 hours of siRNA incubation with siCBX2 #4. Whereas in the SNB-19 cell line, there was a greater decrease in spheroid diameter, although not statistically significant, after only 48 and 96 hours, with siCBX2 #4 instigating the greatest observable reduction in growth. It is worth noting that the SNB-19 spheroids grew more irregularly shaped spheroids than the U-87 MG spheroids.

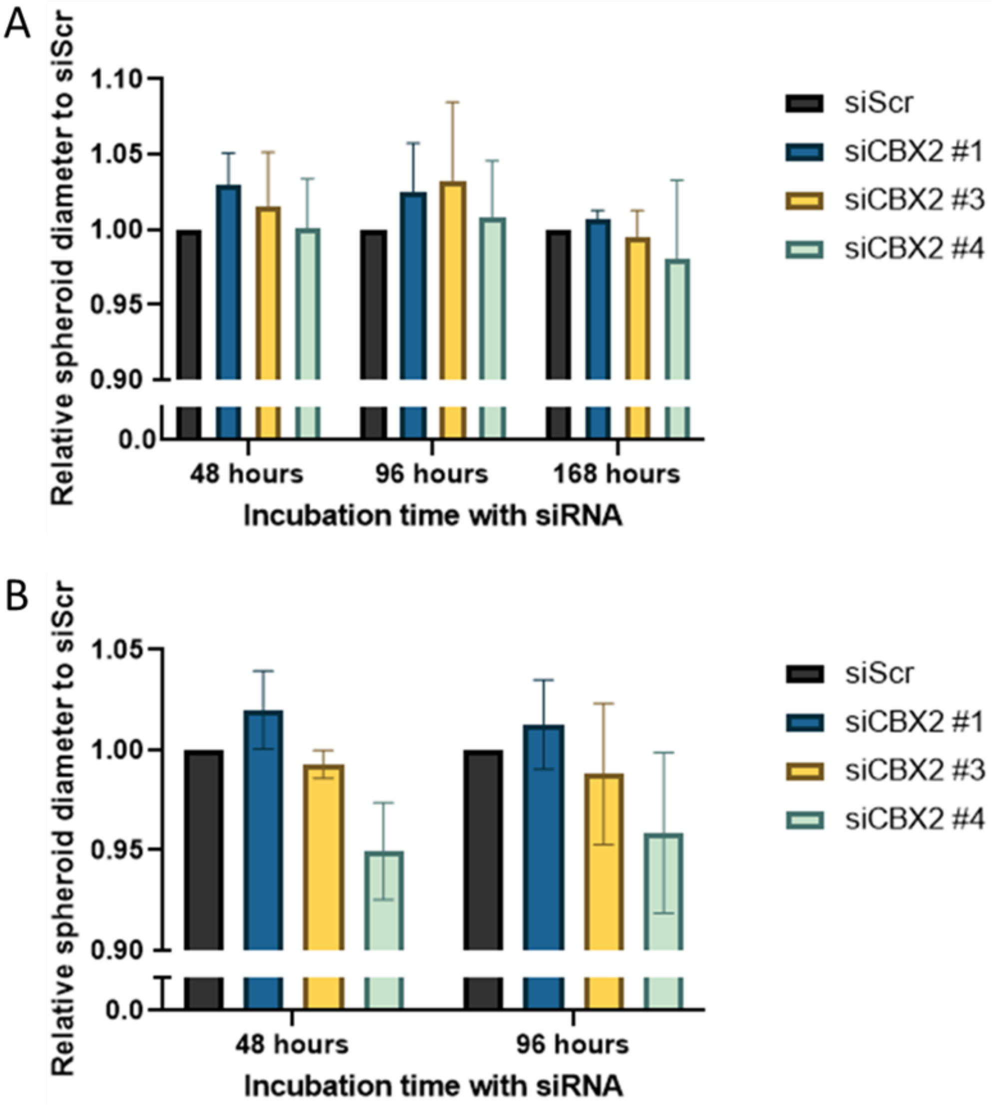

Figure 3.11. Average diameter for each siRNA used following 3D siRNA knockdown on U-87 MG and SNB-19 spheroids. The spheroid diameter of siScr and siCBX2 #1, 3, and 4 each made relative to the siScr transfected cells. (A) Spheroid diameter of U-87 MG cells following siRNA knockdown. (B) Spheroid diameter of SNB-19 cells following siRNA knockdown. Mean calculated from repeats, n=3; refers to 3 individual runs/ experiments for each cell line, totalling 36 wells per siRNA used, per cell line. Error bars show the standard deviation. Ordinary one-way ANOVA performed.

The effect of CBX2 siRNA knockdown on protein expression was analysed using western blots. Western blot analysis of 3D siRNA knockdown on U-87 MG spheroids when incubated with the CBX2 antibody can be seen in Figure 3.12.

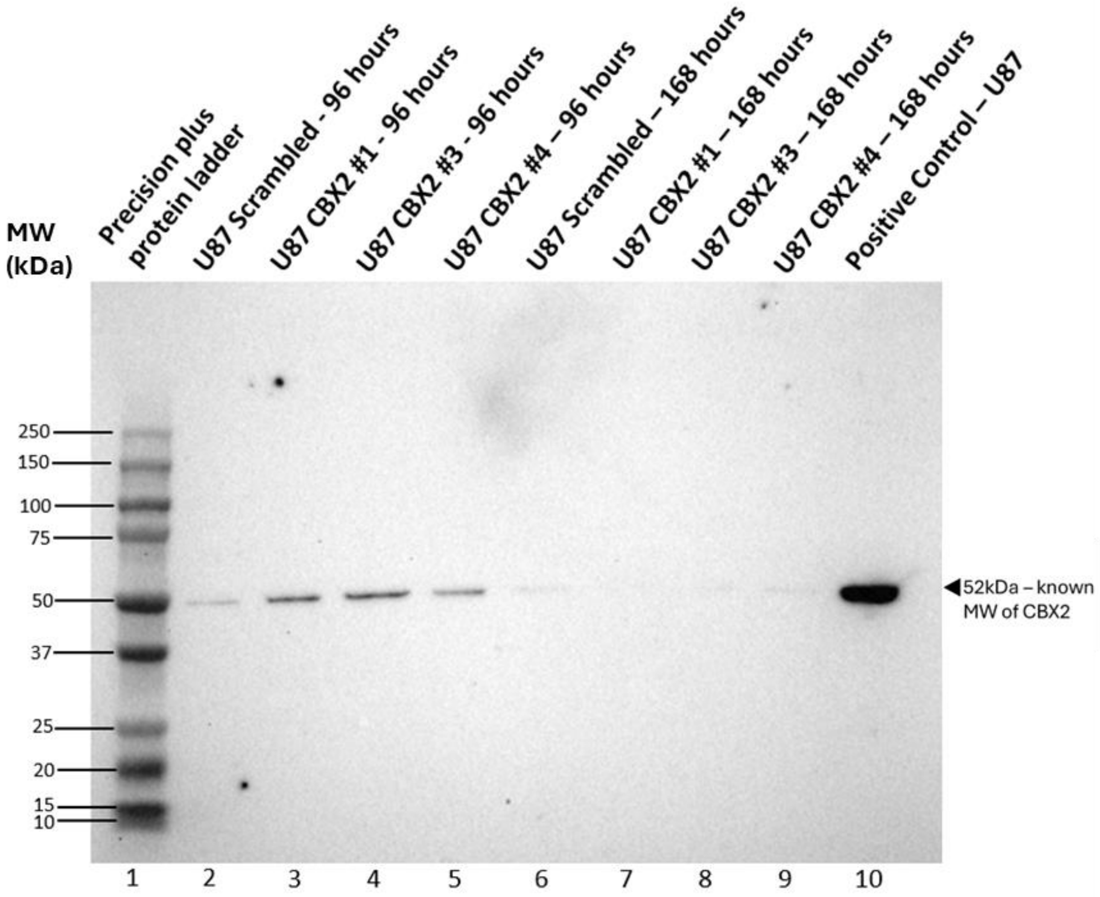

Figure 3.12. Western blot of U-87 MG cell protein lysates collected from 3D siRNA knockdown experiments, incubated with CBX2 antibody. Cells transfected with the siRNA's, siScr, siCBX2 #1, 3, and 4. A U-87 MG lysate was loaded into well 10 for comparison between gels as a positive control. Half the samples were collected after 96 hours of incubation, with the other half being collected after 168 hours of incubation. The bands produced are representative of CBX2 expression within each lysate following transfection. (n=1).

The same western blot, loaded with U-87 MG 3D siRNA knockdown lysates, was also incubated with GAPDH to check for protein expression (Figure 3.13) and for densitometry analysis (Figure 3.14).

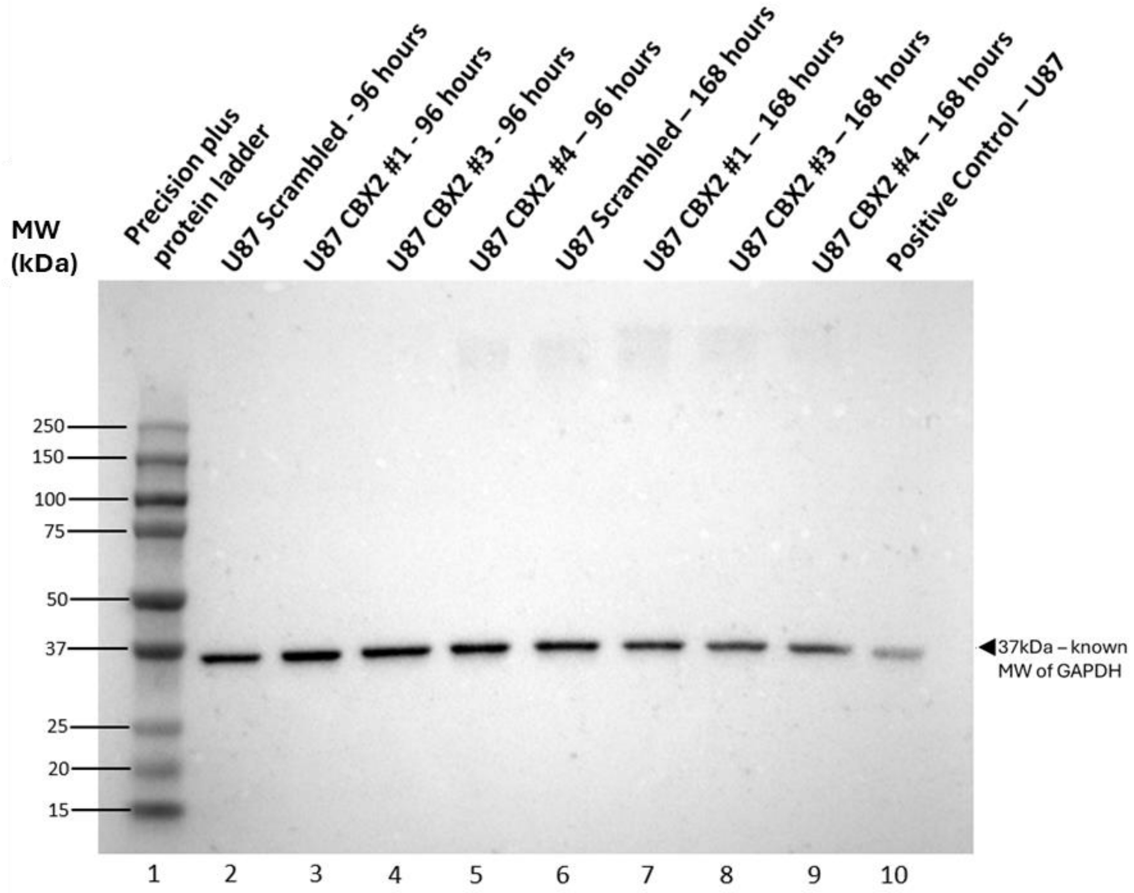

Figure 3.13. Western blot of U-87 MG cell protein lysates collected from 3D siRNA knockdown experiments, incubated with GAPDH antibody. Cells transfected with the siRNA's, siScr, siCBX2 #1, 3, and 4. A U-87 MG lysate was loaded into well 10 for comparison between gels as a positive control. The bands present are representative of GAPDH expression within each lysate following transfection.

Despite multiple repeats of the 3D siRNA knockdowns on the U-87 MG spheroids, the resulting western blots,, which despite using fresh reagents, different equipment, and fresh samples and antibodies, showed no bands for any of the siRNA transfected cells. Consequently, the results, as seen in Figure 3.12 could not be repeated in the 3D model. Multiple repeats of siRNA knockdown were also performed on the SNB-19 cell line in the spheroid model, however, no bands were ever observed on the western blots when incubated with the CBX2 antibody.

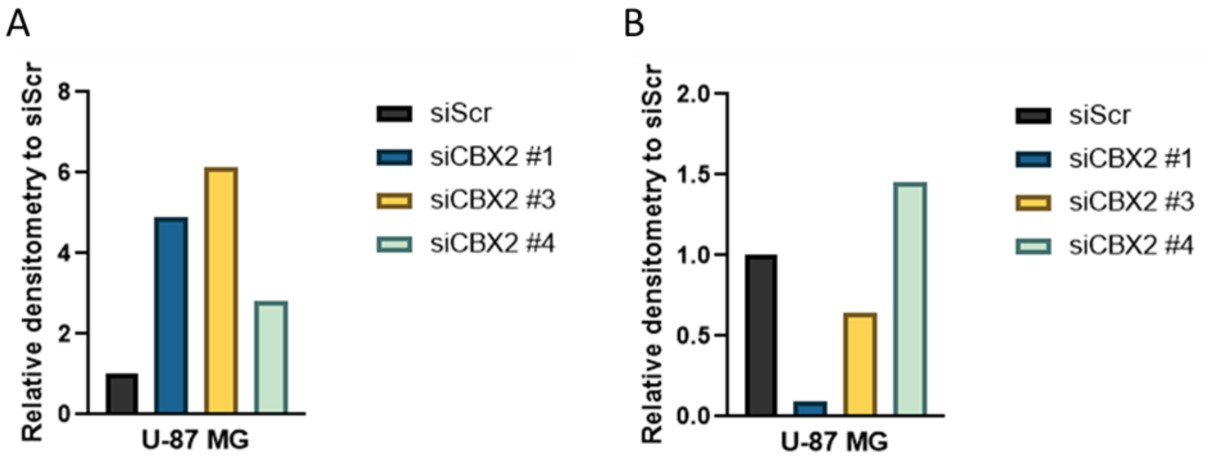

Figure 3.14. Densitometry results from U-87 MG 3D siRNA knockdown western blot. Band density of CBX2 normalised against the control. GAPDH incubated western blot bands were used as the control. (A) Normalised band density of U-87 MG spheroids, after 96 hours of incubation. (B) Normalised band density of U-87 MG spheroids, after 168 hours of incubation. (n=1).

Expression of CBX2 in the 3D model, following siRNA knockdown, was also analysed using RT-qPCR. Both siCBX2 #3 and 4 caused a reduction in CBX2 expression in the U-87 MG spheroid model, with an expression fold change of 0.9, when made relative to the control (Figure 3.15.A). The expression of RBL2 in the 3D siRNA knockdown of the U-87 MG cell line was seen to decrease in all siCBX2 variants, with siCBX2 #4 showing the greatest reduction in expression when made relative to siScr (Figure 3.15.B).

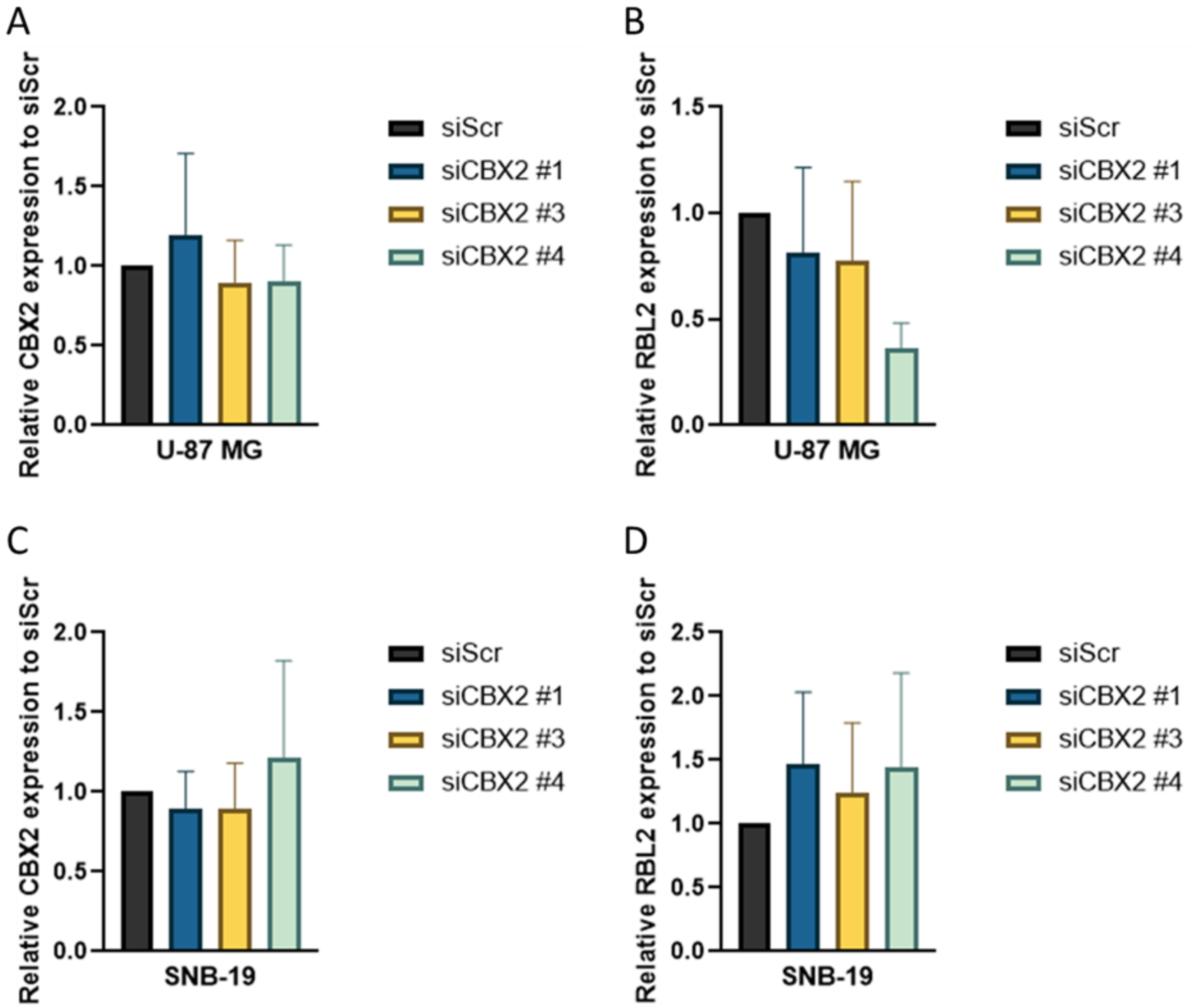

Figure 3.15. RT-qPCR results of 3D siRNA knockdown of U-87 MG and SNB-19 spheroids. Analysing the change in expression of CBX2 and RBL2. Expression fold change was calculated against RPL13A as the control gene. Expression fold change of siCBX2 #1, 3, and 4 were each made relative to siScr. (A) CBX2 expression in U-87 MG. B) RBL2 expression in U-87 MG. C) CBX2 expression in SNB-19. D) RBL2 expression in SNB-19. Mean calculated from repeats, n=3. Error bars show the standard deviation. Ordinary one-way ANOVA performed.

The expression fold change of the SNB-19 cell line following RT-qPCR of 3D siRNA knockdown samples exhibited a decrease in CBX2 expression in both siCBX2 #1 and 3, whereas siCBX2 #4 caused an increase in CBX2 expression, when compared to siScr (Figure 3.15.C). RBL2 expression in the SNB-19 spheroids showed an increase in expression fold change following incubation with the siCBX2 transfection agents when compared to siScr for all siCBX2 variants used (Figure 3.15.D). Statistical analysis in both cell lines for the change in expression of both CBX2 and RBL2 showed no significant changes following siRNA knockdown within the 3D model.

3.1.3. Breast Cancer Cells

Due to issues with reliably detecting CBX2 in brain tumour cells, an investigation into the expression in three breast cancer cell lines, that have been shown to previously express CBX2, was conducted for comparison. The morphological effects observed following siRNA knockdown of CBX2 were analysed in a 2D model using the MDA-MB-231 cell line, the effects of which can be seen in Figure 3.16. Microscopic images were taken prior to collection, after 72 hours of incubation. Visually, the CBX2 transfection agents applied all had an effect in reducing cell density within the well, with siCBX2 #4 inducing the cells to have larger gaps between them than the other siRNA used.

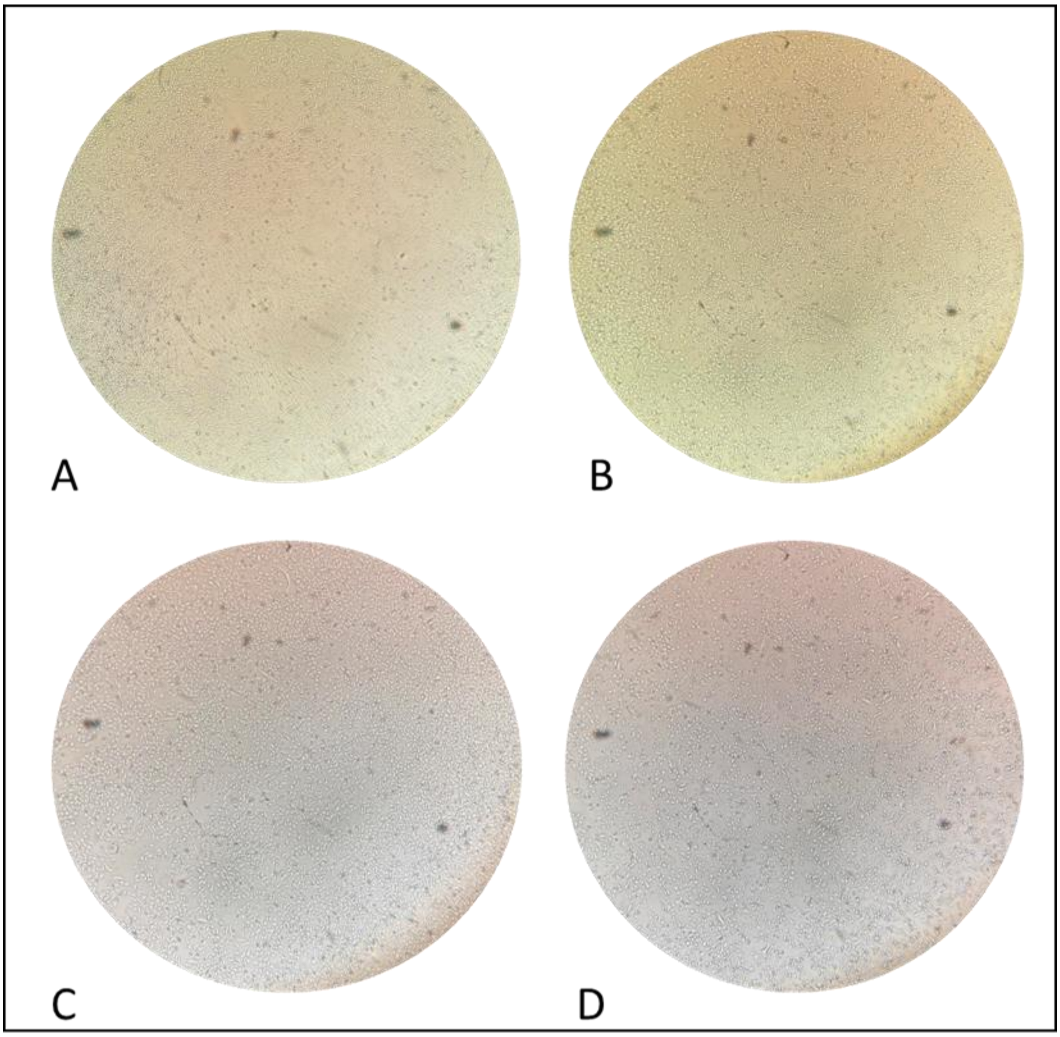

Figure 3.16. Microscopic images taken of MDA-MB-231 cells which have undergone transfection. Using the siRNA knockdown agents, siScr, and siCBX2 #1, 3, and 4, in the 2D model. Images taken 72 hours post-setup at 10x magnification, prior to collection. A) siScr, B) siCBX2 #1, C) siCBX2 #3, D) siCBX2 #4. (n=2; 2 independent experiments).

Further to microscopic analysis, the MDA-MB-231 cells were counted following collection to observe the effect of CBX2 on cell growth and number (Figure 3.17). Although there was time for only a single experiment, the overall trend demonstrated that the transfection of all CBX2 targeting siRNA caused a reduction in cell number, when compared to the siScr treated cells, with siCBX2 #3 providing the greatest reduction in cell number for the MDA-MB-231 cells.

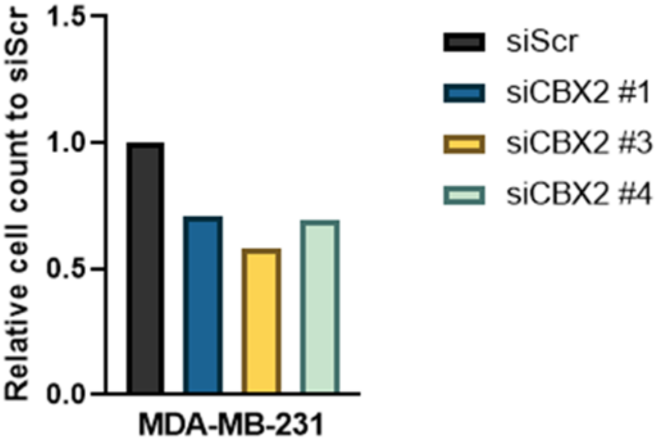

Figure 3.17. Cell count observed for each siRNA used following 2D siRNA knockdown on MDA-MB-231 cells. Cell count of siScr and siCBX2 #1, 3, and 4 each made relative to the siScr transfected cells. (n=1).

To further the investigation into CBX2 expression within breast cancer cells, 3D siRNA experiments were completed using spheroids from MDA-MB-231, MCF-7, and T47D cell lines. The morphological effects of siRNA knockdown on the breast cancer spheroids can be seen in Figure 3.18. Images were taken after 96 hours of incubation and prior to collection, using a Gelcount.

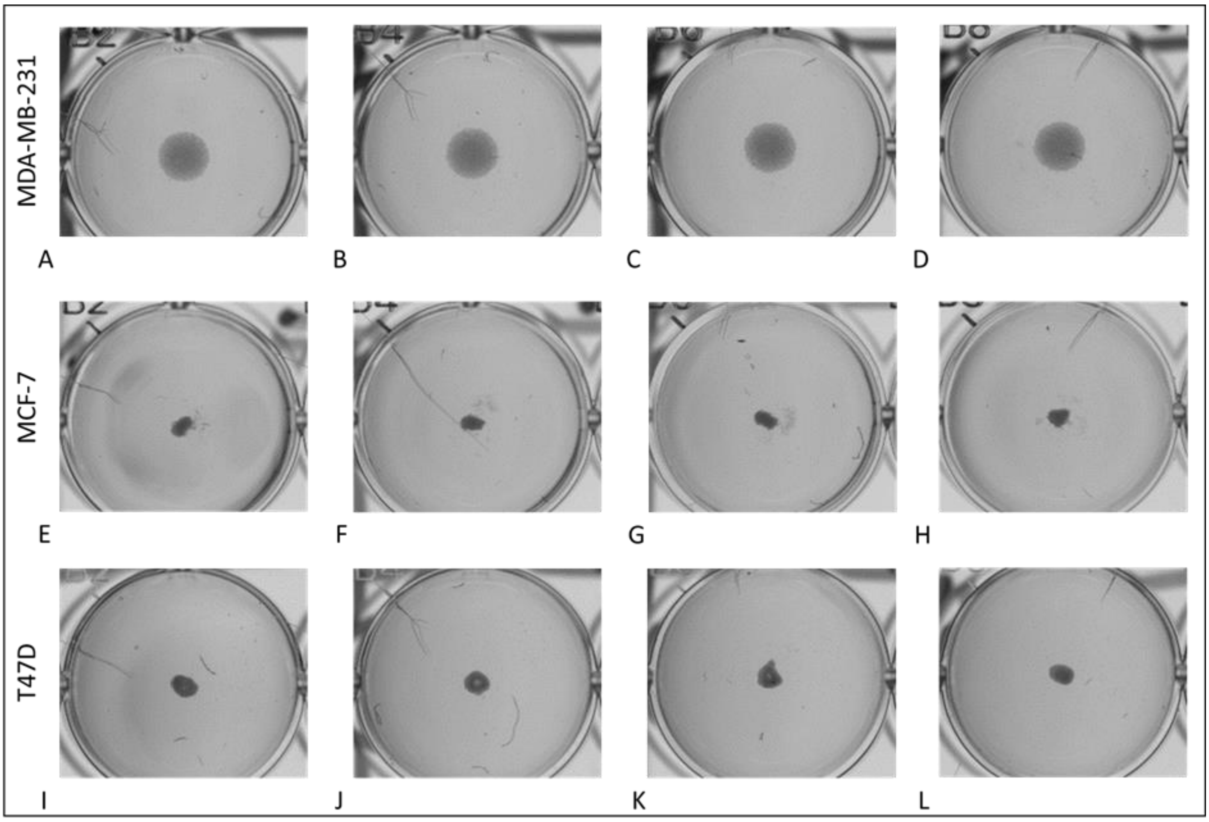

Figure 3.18. Images taken of MDA-MB-231, MCF-7, and T47D spheroids which have undergone transfection. Using the siRNA knockdown agents, siScr, and siCBX2 #1, 3, and 4. Images taken 96 hours post-setup, prior to collection using a Gelcount. MDA-MD-231 spheroids ranging in diameter from 1.29mm to 1.44mm. MCF-7 spheroids ranging in diameter from 0.36mm to 0.53mm. T47D spheroids ranging in diameter from 0.52mm to 0.7mm. MDA-MB-231: A) siScr, B) siCBX2 #1, C) siCBX2 #3, D) siCBX2 #4. MCF-7: E) siScr, F) siCBX2 #1, G) siCBX2 #3, H) siCBX2 #4. T47D: I) siScr, J) siCBX2 #1, K) siCBX2 #3, L) siCBX2 #4. (n=24; 6 independent experiments, 2 for each cell line used, with 12 spheroids imaged per siRNA agent for each run).

Spheroid diameter analysis was completed to determine the effect on cell growth after the addition of each siRNA; the spheroid diameter averages for the siRNA transfections for MDA-MB-231 (Figure 3.19.A), MCF-7 (Figure 3.19.B), and T47D (Figure 3.19.C) can be seen below. The addition of the transfection agents was variable across cell lines, and although only undertaken once, the trend demonstrates that siCBX2 #4 had the greatest effect overall, particularly on the MCF-7 and T47D spheroids. It was noted that the other siRNA’s used appeared to have little to no effect on spheroid diameter.

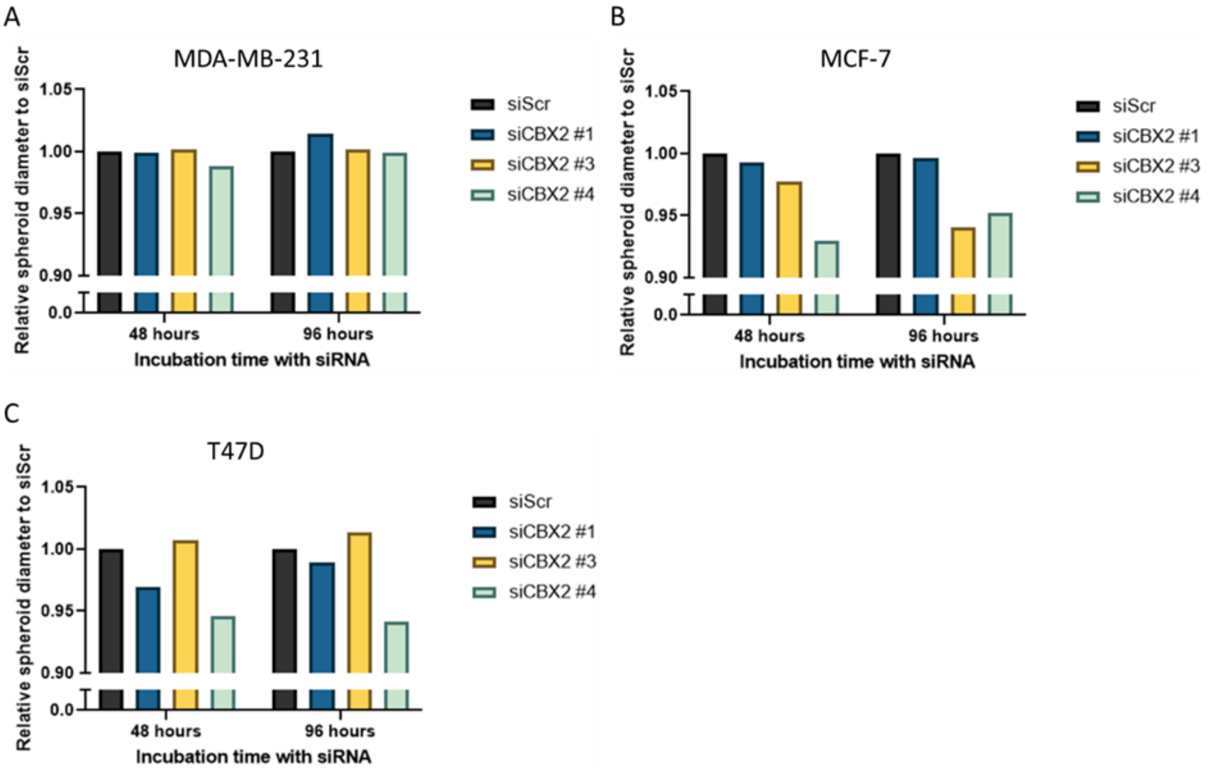

Figure 3.19. Average diameter for each siRNA used following 3D siRNA knockdown on MDA-MB-231, MCF-7, and T47D spheroids. The spheroid diameter of siScr and siCBX2 #1, 3, and 4 each made relative to the siScr transfected cells. (A) Spheroid diameter of MDA-MB-231 cells following siRNA knockdown. (B) Spheroid diameter of MCF-7 cells following siRNA knockdown. (C) Spheroid diameter of T47D cells following siRNA knockdown. n=1; 12 wells per siRNA, per cell line.

Western blots were performed on the 2D, and 3D siRNA knockdowns completed for the breast cancer cell lines, MDA-MB-231, MCF-7, and T47D. However, no bands were present following incubation with the CBX2 antibody. For all samples analysed, correctly sized bands were present when tested for GAPDH expression.

Expression of CBX2 and RBL2 was analysed using RT-qPCR, with the cells which had undergone 2D and 3D siRNA knockdown with siCBX2 agents. As before, the RPL13A gene was used as the control, to which CBX2 and RBL2 expression was compared. With a single experiment completed, the trend observed showed that the greatest reduction in expression of CBX2 in the MDA-MB-231 cell line, using a 2D model, was with siCBX2 #4 (Figure 3.20.A). The expression of RBL2 in the 2D siRNA knockdown of the MDA-MB-231 cell line was seen to increase in all siCBX2 conditions, with siCBX2 #1 showing the greatest increase in expression fold change, with 4.78

(Figure 3.20.B). Again, for RBL2, only a single experiment was completed, and therefore, no statistical analysis was performed.

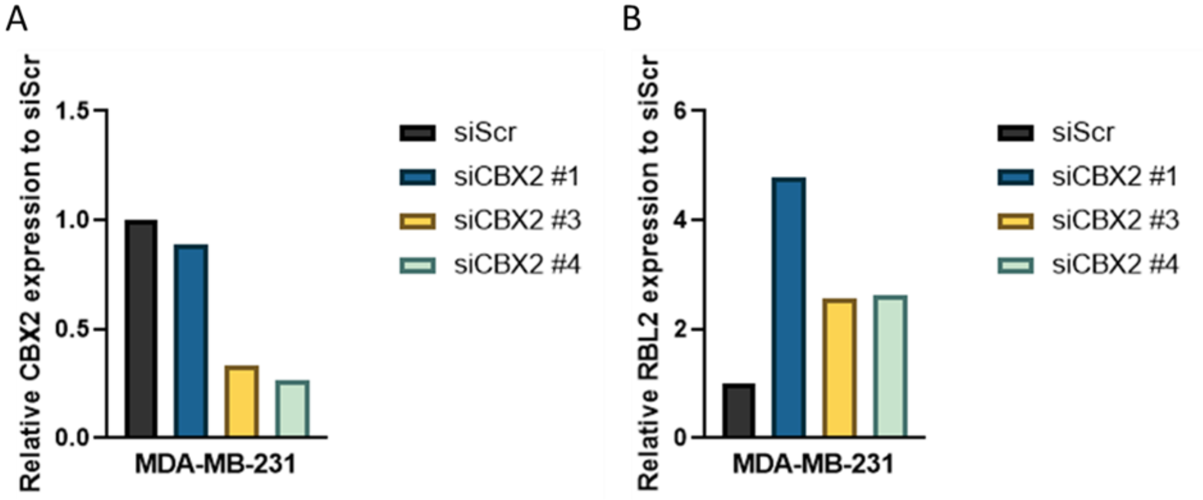

Figure 3.20. RT-qPCR results of 2D siRNA knockdown on MDA-MB-231 cells. Analysing CBX2 and RBL2 expression. Expression fold change calculated against RPL13A as the control. Expression fold change of siCBX2 #1, 3, and 4 each made relative to siScr. (A) CBX2 expression in MDA-MB-231. (B) RBL2 expression in MDA-MB-231. (n=1).

Expression of CBX2 and RBL2 was also analysed using RT-qPCR in the 3D spheroid models of MDA-MB-231, T47D, and MCF7 spheroids which had undergone siRNA knockdown, as outlined in Figure 3.21.

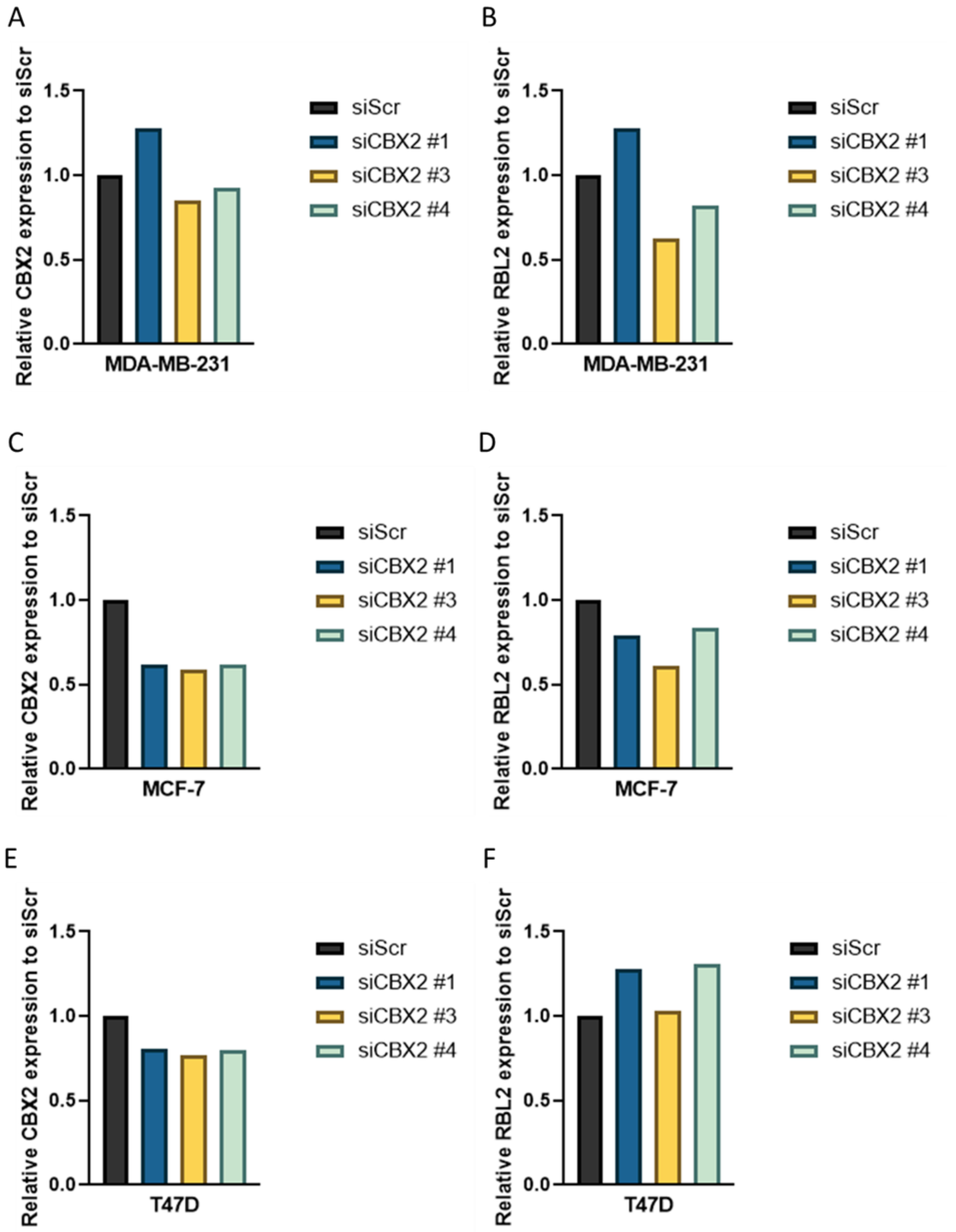

Figure 3.21. RT-qPCR results of 3D siRNA knockdown of MDA-MB-231, MCF-7, and T47D spheroids. Analysing the change in CBX2 and RBL2 expression. Expression fold change was calculated against RPL13A as the control. Expression fold change of siCBX2 #1, 3, and 4 were each made relative to siScr. (A) CBX2 expression in MDA-MB-231. (B) RBL2 expression in MDA-MB-231. (C) CBX2 expression in MCF-7. (D) RBL2 expression in MCF-7. (E) CBX2 expression in T47D. (F) RBL2 expression in T47D. (n=1).

For all RT-qPCR experiments for the three breast cancer cell lines used, a single experiment was completed, and so all results observed are trends, with no statistical analysis possible. With that in mind, in the 3D model, the greatest reduction in expression of CBX2 in the MDA-MB-231 cell line was with siCBX2 #3 (Figure 3.21.A), with siCBX2 #1 apparently causing an increase in CBX2 expression levels. The expression of RBL2 in MDA-MB-231 cells was seen to only increase in siCBX2 #1, with siCBX2 #3 and #4 decreasing in RBL2 expression, when made relative to siScr (Figure 3.21.B). CBX2 and RBL2 expression was seen to decrease in all siCBX2 types in the MCF-7 cells (Figure 3.21 C and D), with siCBX2 #3 showing the largest decrease in expression with both primers (CBX2 and RBL2), when compared to RPL13A. CBX2 expression decreased in all types of siCBX2 in the T47D cell line, with siCBX2 #3 showing the greatest decrease in expression (Figure 3.21.E). RBL2 expression was seen to increase in all siCBX2 used when compared to the control, with siCBX2 #4 exhibiting the greatest increase (Figure 3.21.F).

3.1.4. Full Flask Lysate Analysis

Due to many repeats of samples which did not produce CBX2 bands on the western blots, protein lysates of confluent, full flasks (T75) of each of the cell lines, U-87 MG, SNB-19, MDA-MB-231, MCF-7, and T47D were collected, and a western blot was performed (Figure 3.22); to check the presence of CBX2 and verify the molecular weight. Western blot analysis demonstrated that although band density differed between the cell line lysates, the molecular weight of CBX2 within all five cell lines was consistently observed at 52kDa.

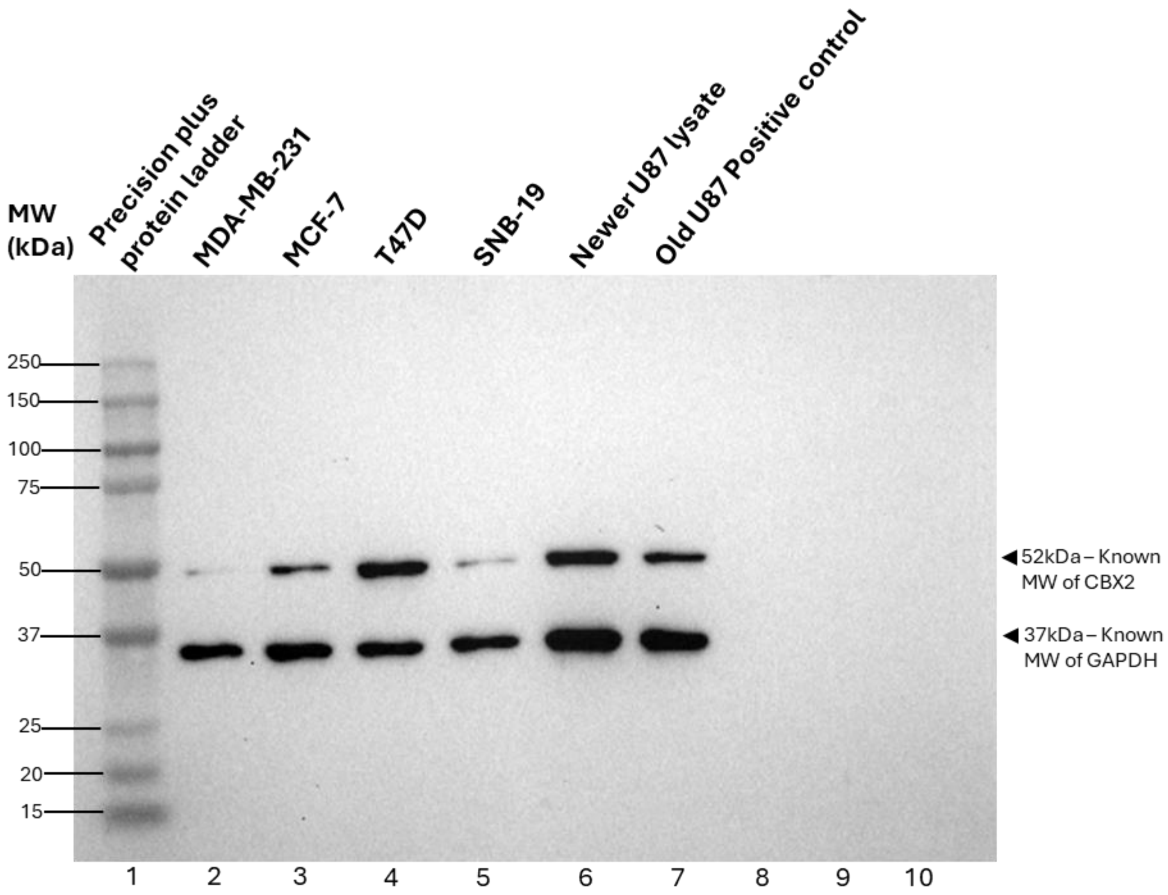

Figure 3.22. Western blot of U-87 MG, SNB-19, MDA-MB-231, MCF-7, and T47D full flask cell protein lysates incubated with GAPDH and then the CBX2 antibody. A U-87 MG lysate was loaded into well 7 for comparison between gels as a positive control, The bands produced are representative of GAPDH and CBX2 expression within each lysate following transfection, as labelled.

3.2. Overexpression of CBX2

To further investigate the role of CBX2 on GBM cell lines, the morphological effects on the cells was analysed following overexpression of CBX2 in a 2D model, using plasmids (Section 2.3). The effects of overexpression on U-87 MG cells can be seen in Figure 3.23. Microscopic images were taken after 72 hours of incubation with the plasmids, and prior to collection. Visually, expression of the pFLAG-tagged gene produced discernible cell clusters (Figure 3.23), however large gaps were also present between the cells and clusters within the well. The full length CBX2 plasmid (with chromodomain present) showed more cells present overall. The cells transfected with the ‘missing chromodomain’ plasmid appeared visually to have the least number of cells present.

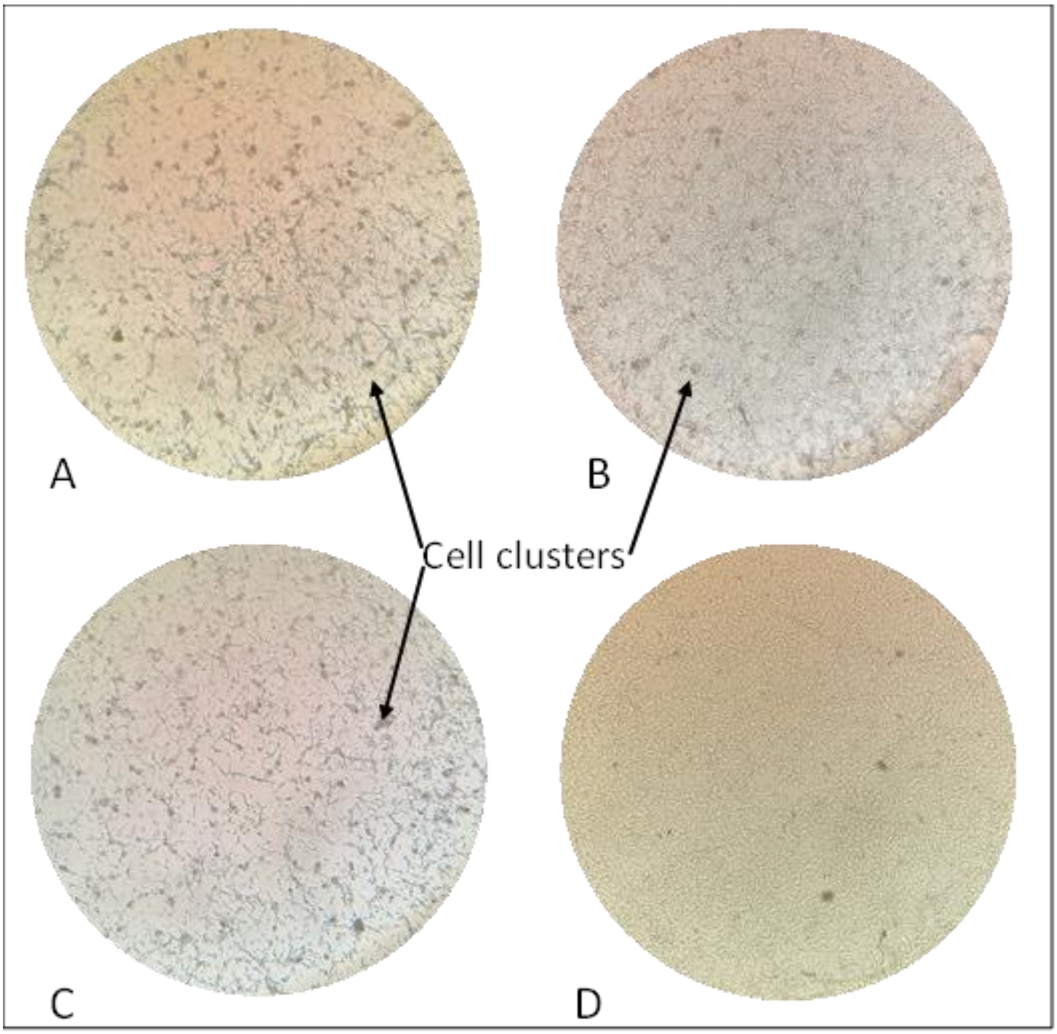

Figure 3.23. Microscopic images taken of U-87 MG cells which have undergone transfection. Using the plasmids containing: pFLAG alone (control), full length CBX2-pFLAG tagged, and CBX2 minus the chromodomain. Cells receiving no plasmid treatment were grown and imaged as another control. Images were taken 72 hours post-setup at 10x magnification, prior to collection. A) pFLAG alone, B) Full length CBX2-pFLAG tagged, C) CBX2 with missing chromodomain-pFLAG tagged, D) Cells alone (no plasmid treatment received). Cell clusters highlighted using arrows. (n=6; 6 independent experiments).

Microscopic images were also taken of the SNB-19 cell line following overexpression of CBX2, after 72 hours of incubation (Figure 3.24). The morphological effects of CBX2 overexpression were not as obvious in the SNB-19 cell line, compared with the U-87 MG cell line. Visually, the pFLAG control plasmid produced lots of cells, however there were small gaps seen between them. The full length CBX2 plasmid resulted in a dense and uniform distribution of cells, displaying the most cells present; no gaps were seen. The CBX2 plasmid missing the chromodomain construct produced the least number of cells, which were also more spread out.

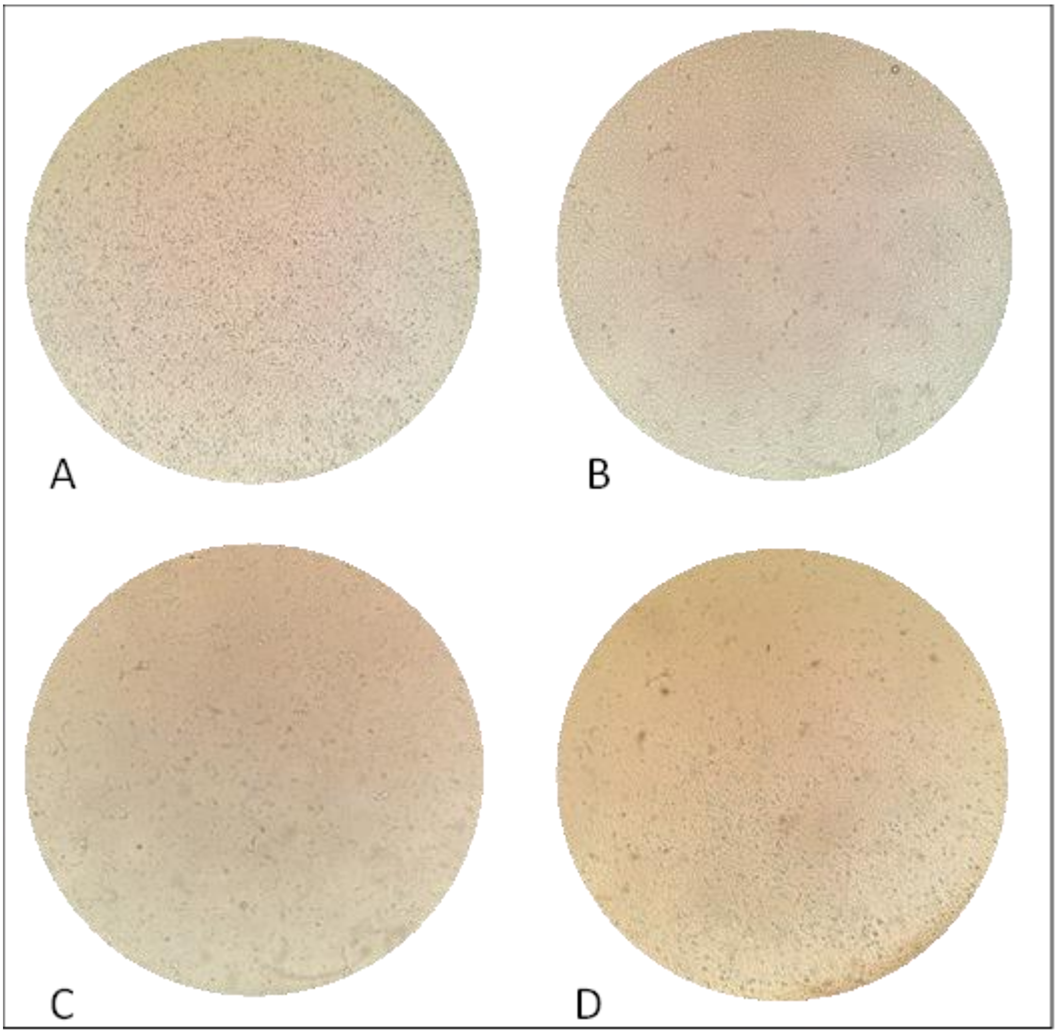

Figure 3.24. Microscopic images taken of SNB-19 cells which have undergone transfection. Using the plasmids containing: pFLAG alone (control), full length CBX2-pFLAG tagged, and CBX2 minus the chromodomain. Cells receiving no plasmid treatment were grown and imaged as another control. Images were taken 72 hours post-setup, prior to collection at 10x magnification. A) pFLAG alone, B) Full length CBX2-pFLAG tagged, C) CBX2 with missing chromodomain-pFLAG tagged, D) Cells alone (no plasmid treatment received). (n=2; 2 independent experiments).

Following this, the cells were harvested and counted to observe the effects of CBX2 overexpression on cell growth and number, caused by the three plasmid constructs used. Cells were counted for each plasmid across each repeat experiment. The cell count average for the 2D overexpression transfections for U-87 MG and SNB-19 can be found in Figure 3.25.A and Figure 3.25.B, respectively. In the U-87 MG cell line, the full-length CBX2 plasmid induced an increase in cell number, when compared to the pFLAG alone, control plasmid, whereas the CBX2 with missing chromodomain construct caused a decrease in cell number. As expected, when compared to the plasmid altered cells, the control cells receiving no treatment increased in cell number.

In comparison, when observing the SNB-19 cells, both the full length and missing chromodomain CBX2 plasmids initiated a reduction in cell number compared to the pFLAG alone construct. Again, the control cells undergoing no plasmid treatment, increased in cell number, as expected. The observations outlined are based on trends seen, as statistical analysis showed no significant change in cell counts between the pFLAG (control) treated cells and the full length CBX2, missing chromodomain, and 'normal'/ untreated cells.

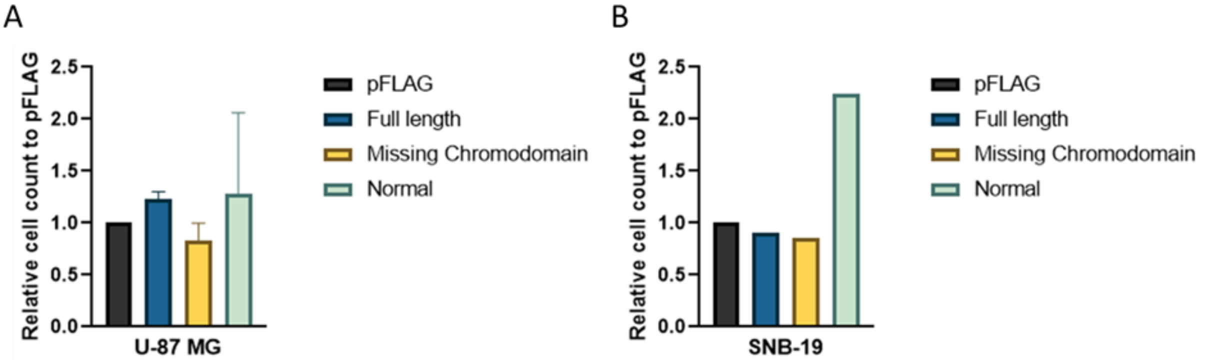

Figure 3.25. Average cell count observed for each plasmid used following 2D overexpression on U-87 MG and SNB-19 cells. The cell counts of the pFLAG alone, full length CBX2, CBX2 with missing chromodomain, and untreated control cells, were each made relative to the pFLAG alone transfected cells. (A) Average cell count observed following 2D overexpression on U-87 MG cells. (B) Cell count observed for each plasmid following 2D overexpression of SNB-19 cells. Mean calculated from repeats, n=3 for A, and n=1 for B. Error bars show the standard deviation. Ordinary one-way ANOVA performed on graph A.

The effect of CBX2 overexpression on protein expression was analysed using western blots. As described above, the cells were lysed, and the protein concentration of samples determined through a BCA assay (Section 2.4); 100µg of protein was loaded into the gel for each cell lysate. A polyclonal CBX2 specific antibody was used to visualise the bands and compare CBX2 expression between the lysates (Section 2.4). Western blot analysis of CBX2 overexpression on U-87 MG cells (2D cell model) when incubated with CBX2 antibody can be seen in Figure 3.26. Overexpression of the CBX2 protein using constructed plasmids was seen to alter the expression of CBX2 through detection at the protein level using western blots. A number of different bands were detected. First a 72kDa band was seen in lane 3, with a 66kDa band also observed in lane 4 for the chromodomain-deleted transfected cells. Similar breakdown products were seen between the full-length and missing chromodomain plasmid products. The 72 kDa and 66 kDa bands are what the reported molecular weight would be for these plasmids as outlined by Kawaguchi et al. (2017).

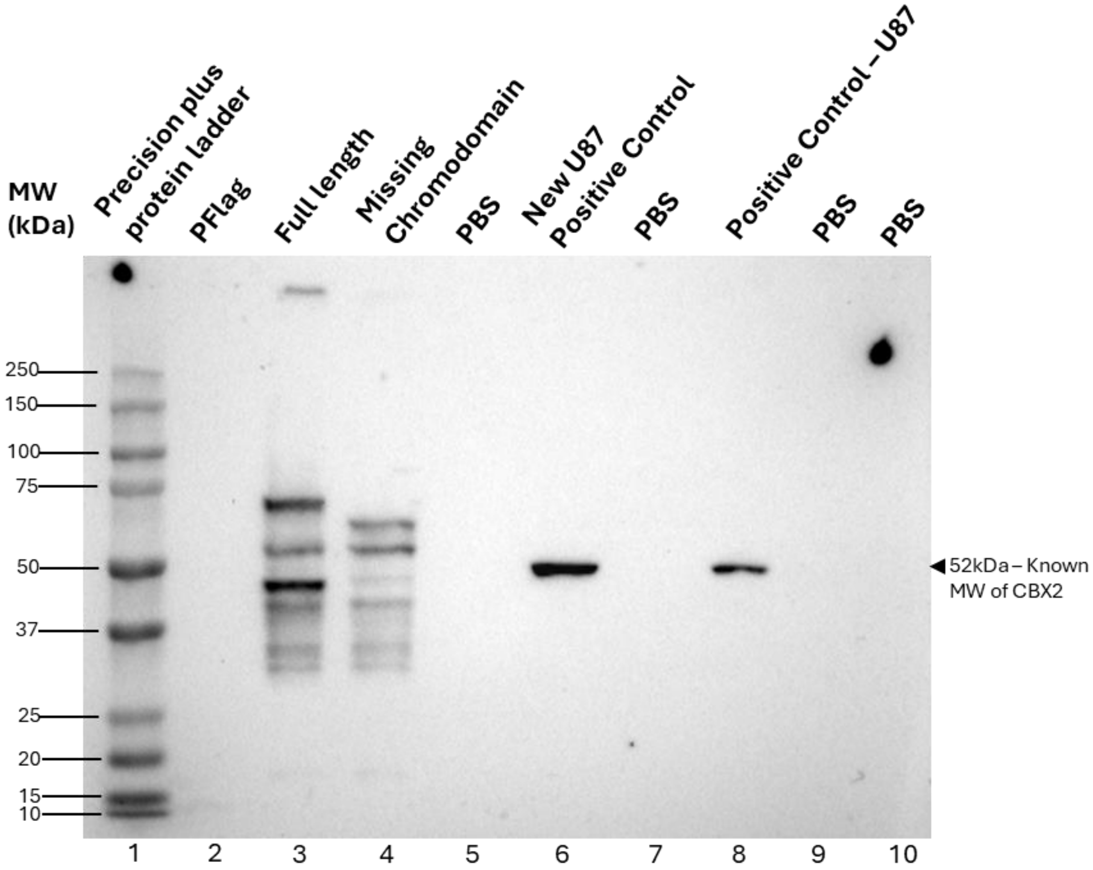

Figure 3.26. Western blot of U-87 MG cell protein lysates collected from 2D overexpression experiments, incubated with CBX2 antibody. Cells transfected with the plasmids: a pFLAG control plasmid consisting of an empty vector with the FLAG tag present, a full length CBX2 plasmid wildtype (with FLAG tag and chromodomain present), as well as a mutated CBX2 plasmid with missing chromodomain sequence (with FLAG tag present). The bands produced are representative of CBX2 expression within each lysate following transfection. A U-87 MG lysate was loaded into well 8 for comparison between gels as a positive control. (n=3; repeat samples 2 and 3 present on the same blot).

The same western blot, loaded with U-87 MG overexpression plasmid lysates, was also incubated with GAPDH to allow for comparison of protein expression (Figure 3.27).

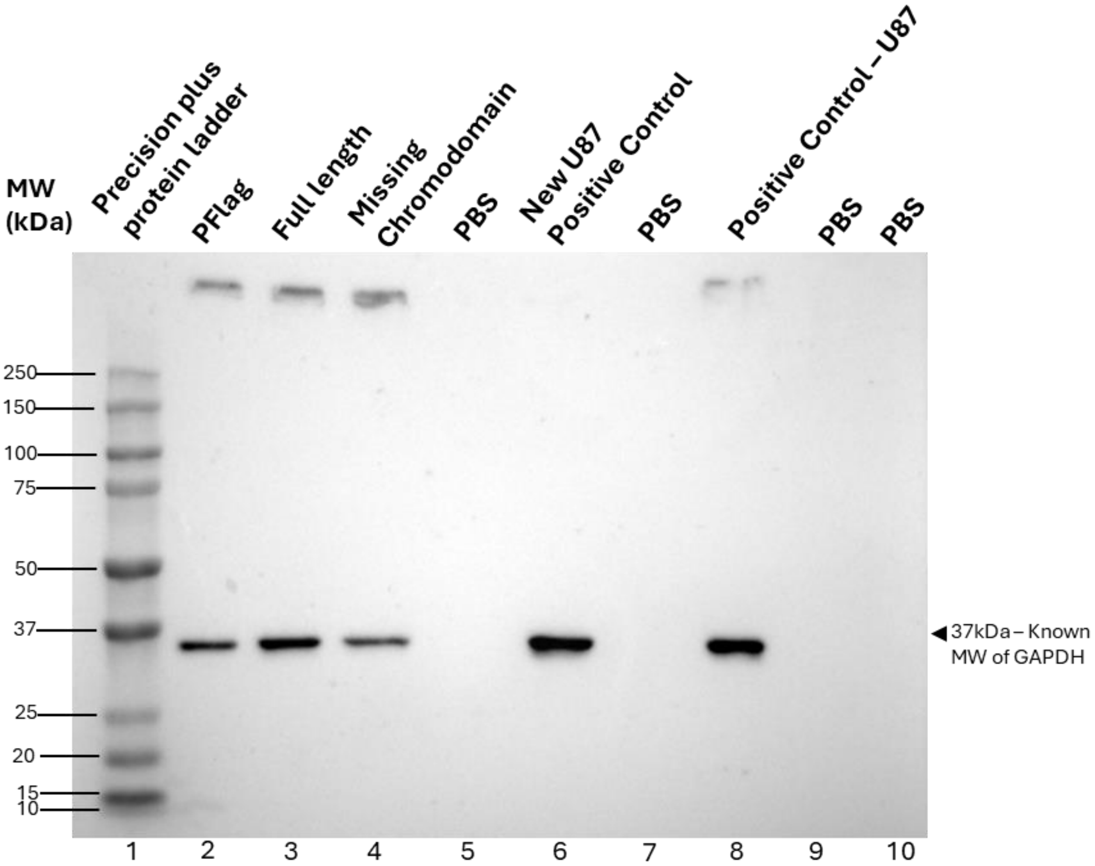

Figure 3.27. Western blot of U-87 MG cell protein lysates collected from 2D overexpression experiments, incubated with GAPDH antibody. Cells transfected with a pFLAG control plasmid, a full length CBX2 plasmid wildtype, as well as a mutated CBX2 plasmid with missing chromodomain. The bands present are representative of GAPDH expression within each lysate following transfection. A U-87 MG lysate was loaded into well 8 for comparison between gels as a positive control. (n=3).

Western blot analysis of 2D overexpression on SNB-19 was also completed; incubation with the CBX2 antibody can be seen in Figure 3.28. Similar bands were observed in the SNB-19 lysates, compared to the U-87 MG cells when transfected with the full-length and missing chromodomain plasmid constructs.

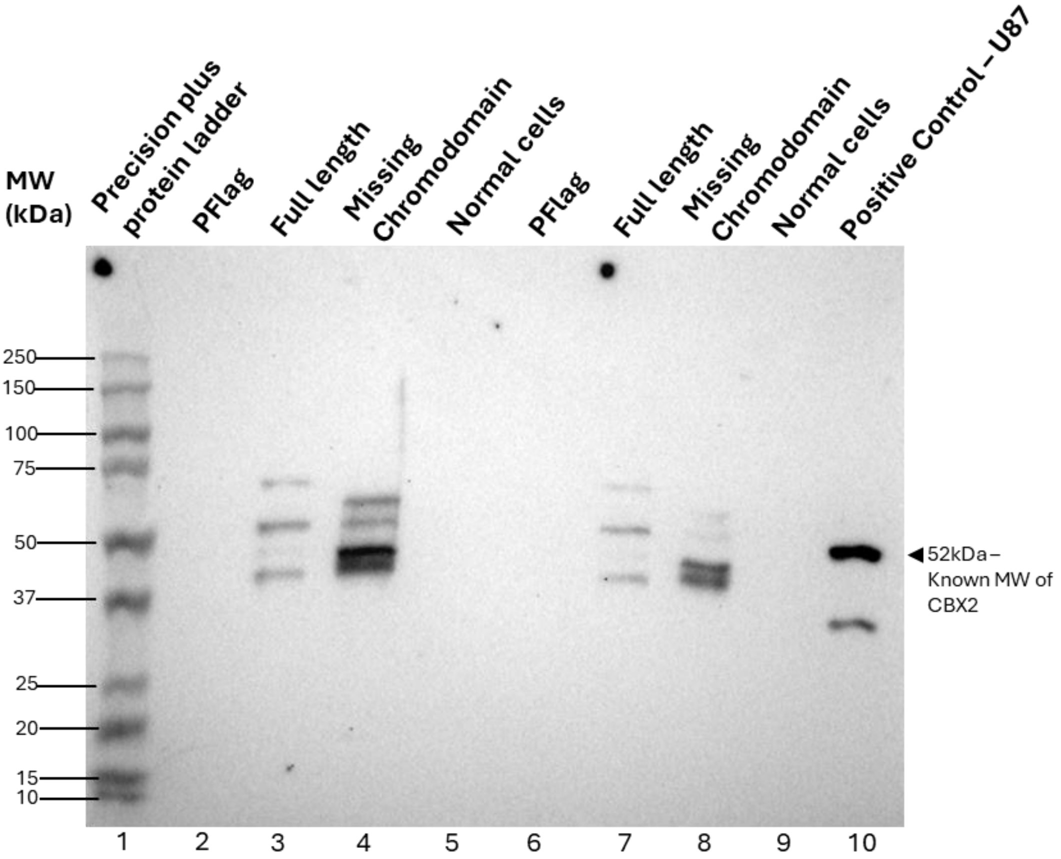

Figure 3.28. Western blot of SNB-19 cell protein lysates collected from 2D overexpression experiments, incubated with CBX2 antibody. Cells transfected with the plasmids: a pFLAG control plasmid consisting of an empty vector with the FLAG tag present, a full length CBX2 plasmid wildtype (with FLAG tag and chromodomain present), as well as a mutated CBX2 plasmid with missing chromodomain sequence (with FLAG tag present). The 'normal' cells refer to SNB-19 cells which were not transfected with any plasmids. The bands produced are representative of CBX2 expression within each lysate following transfection. For comparison, 100µg of protein was loaded into wells 2, 3, 4, 5, and 10, with 75µg of protein loaded into wells 6, 7, 8, and 9. A U-87 MG lysate was loaded into well 10 for comparison between gels as a positive control. (n=1).

The same western blot, loaded with SNB-19 overexpression plasmid lysates, was also incubated with GAPDH to check for protein expression (Figure 3.29).

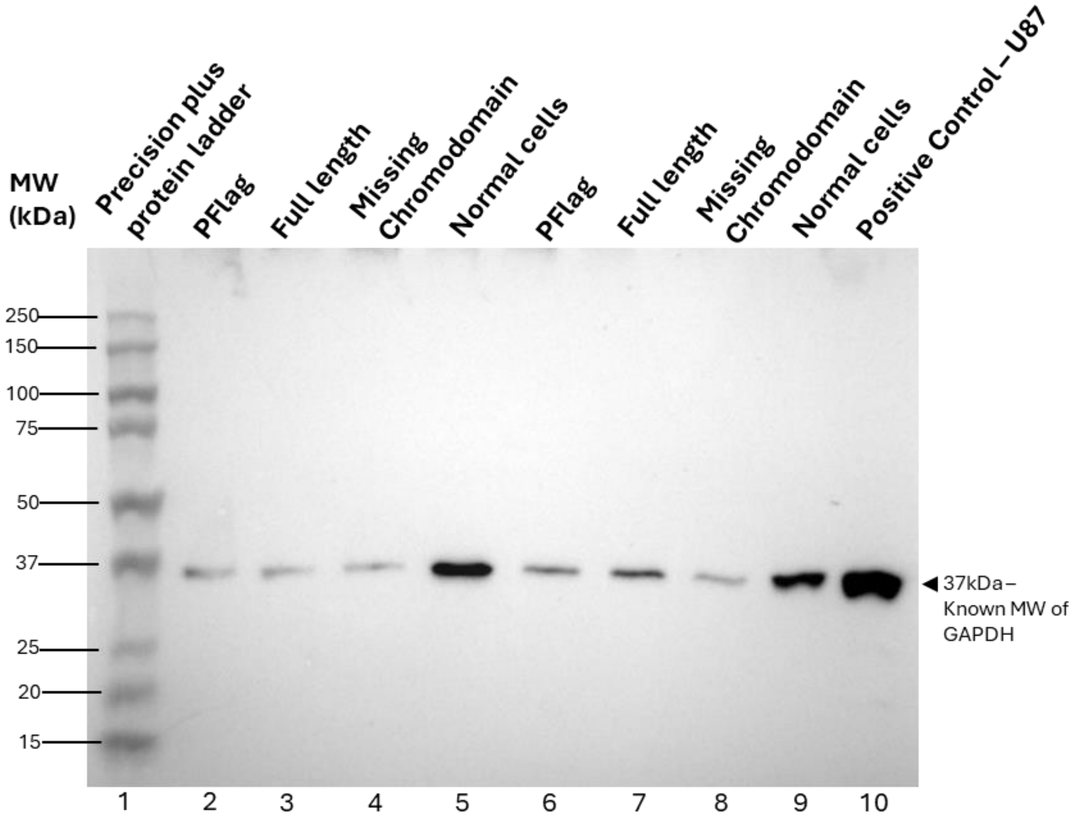

Figure 3.29. Western blot of SNB-19 cell protein lysates collected from 2D overexpression experiments, incubated with GAPDH antibody. Cells transfected with a pFLAG control plasmid, a full length CBX2 plasmid wildtype, as well as a mutated CBX2 plasmid with missing chromodomain. The 'normal' cells refer to SNB-19 cells which were not transfected with any plasmids. The bands present are representative of GAPDH expression within each lysate following transfection. For comparison, 100µg of protein was loaded into wells 2, 3, 4, 5, and 10, with 75µg of protein loaded into wells 6, 7, 8, and 9. A U-87 MG lysate was loaded into well 8 for comparison between gels as a positive control. (n=1).

Expression of CBX2 following overexpression with plasmids was also analysed using RT-qPCR, which was performed following RT, with CBX2, RBL2, and RPL13A primers; RPL13A was used as the control, against which CBX2 and RBL2 expression were compared. The expression of CBX2 in the U-87 MG cell line was seen to reduce in all samples when compared to the pFLAG alone plasmid (Figure 3.30.A), however there was an increase in CBX2 expression in the full length sample, compared to the normal cells. The expression of RBL2 in the U-87 MG cell line was seen to increase only in the normal cells, whereas the full length CBX2 and CBX2 with missing chromodomain samples demonstrated a reduction in RBL2 expression (Figure 3.30.B). Statistical analysis was performed, however all *p-values* observed were $p>0.05$, and therefore no significant results were seen.

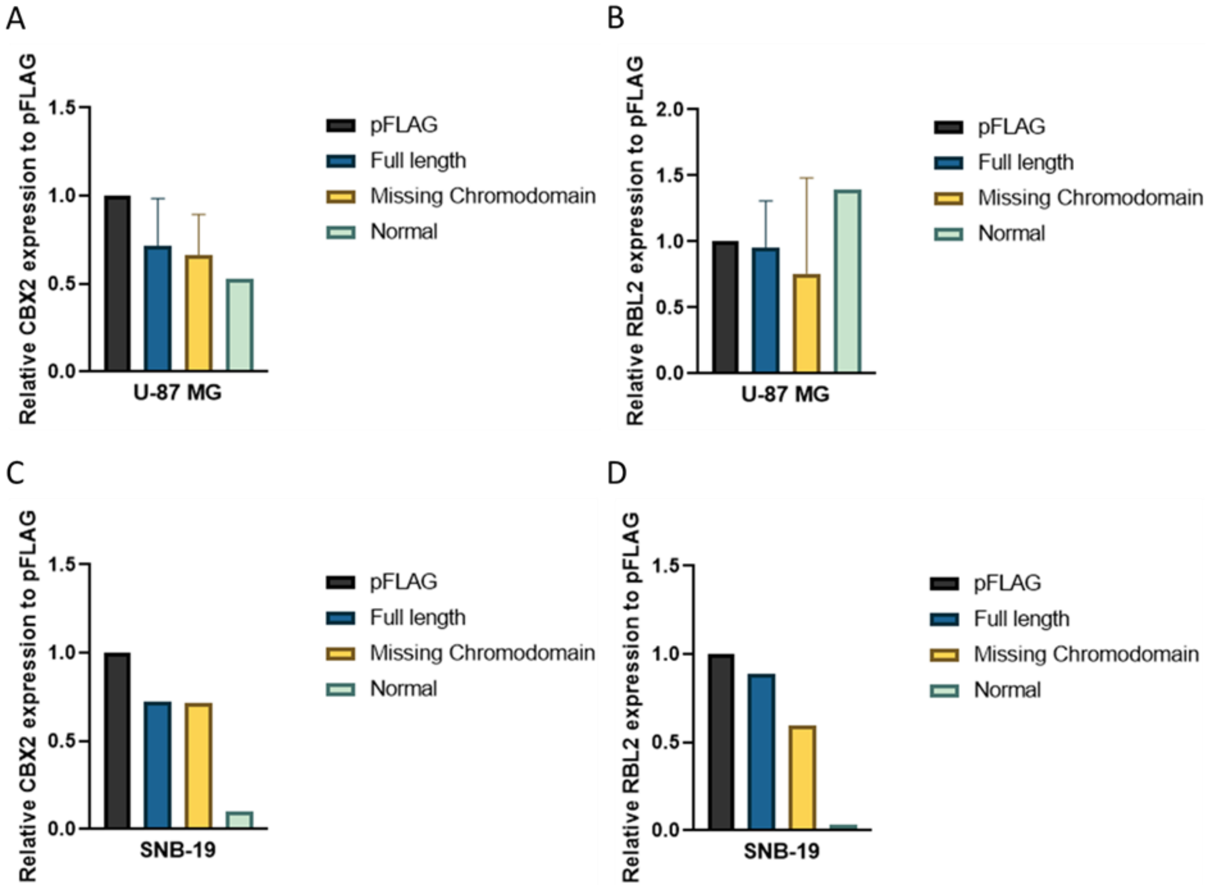

Figure 3.30. RT-qPCR results of 2D overexpression experiments on U-87 MG and SNB-19 cells. Analysing the expression of CBX2 and RBL2 following transfection of various plasmids. Expression fold change was calculated against RPL13A as the control. Expression fold change of full length CBX2, CBX2 with missing chromodomain, and untreated, 'normal' samples were each made relative to the pFLAG alone cells. (A) CBX2 expression in U-87 MG. (B) RBL2 expression in U-87 MG. (C) CBX2 expression in SNB-19. (D) RBL2 expression in SNB-19. Mean calculated from repeats were applicable; n=3 for A and B, and n=1 for C and D. However, only n=1 for all 'normal, control' samples. Error bars show the standard deviation. Ordinary one-way ANOVA performed.

The expression of CBX2 in the SNB-19 cell line was seen to reduce in all samples when compared to the pFLAG plasmid (Figure 3.30.C), however there was an increase in CBX2 expression in the full length sample, compared to the normal cells. Further to this, RBL2 expression was also seen to be reduced in the full length, missing chromodomain, and normal cells when made relative to the pFLAG plasmid cells, with the normal cells exhibiting the greatest reduction, at 0.03 (Figure 3.30.D).

3.3. Effect of Microfluidic Incubation on Protein Expression

The effect of microfluidic incubation on CBX2 (and RBL2) expression was analysed using both static and microfluidic models for comparison. RT-qPCR was performed on the samples collected (Figure 3.31).

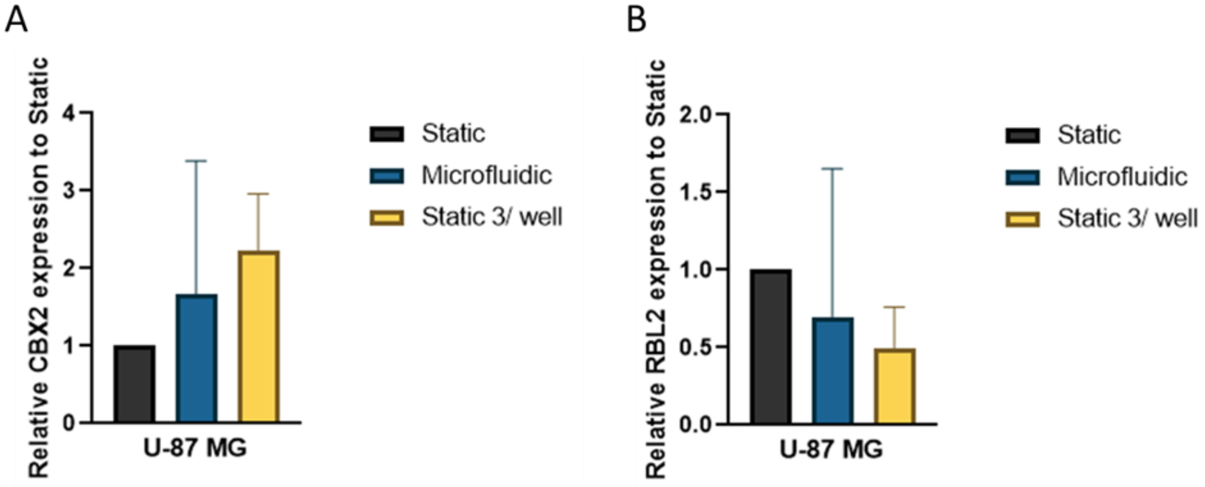

Figure 3.31. RT-qPCR analysis of U-87 MG spheroids incubated in either a static, microfluidic, or a static with 3 spheroids per well model. Expression fold change against the primer, RPL13A as the control. Expression fold change of the microfluidic and static 3 spheroids/ well samples were each made relative to the static samples. (A) RT-qPCR of RNA samples collected from U-87 MG static vs. microfluidic experiments using CBX2 as the primer. (B) RT-qPCR of RNA samples collected from U-87 MG static vs. microfluidic experiments using RBL2 as the primer. Mean calculated from repeats, n=3 for A, n=2 for B (3 repeats performed, one set of static results was an outlier set and was discounted). Error bars show the standard deviation. Ordinary one-way ANOVA performed.

CBX2 expression was seen to increase in the microfluidic spheroid model when made relative to the static model, with the microfluidic incubated spheroids increasing CBX2 expression 1.66-fold (Figure 3.31.A). The incubation of U-87 MG spheroids in a static model was analysed with both 1 spheroid per well and 3 spheroids per well, the latter condition mirroring the microfluidic experiments where 3 spheroids were maintained in each device. By increasing the number of spheroids in each ULA plate well to 3, the expression of CBX2 was seen to increase 2.33-fold. Following incubation in a microfluidic device, the U-87 MG spheroids were seen to reduce in RBL2 expression when compared to the static spheroids (Figure 3.31.B). In addition to this, in the static model, incubating 3 spheroids per well reduced RBL2 expression by half.

Due to an outlier identified with one of the repeat sets for the static vs. microfluidic experiment in the U-87 MG cell line with the RBL2 primer, one set of results was discounted from the average. Figure 3.32 shows the RT-qPCR results for this experiment with the outlier results included within the average expression fold change.

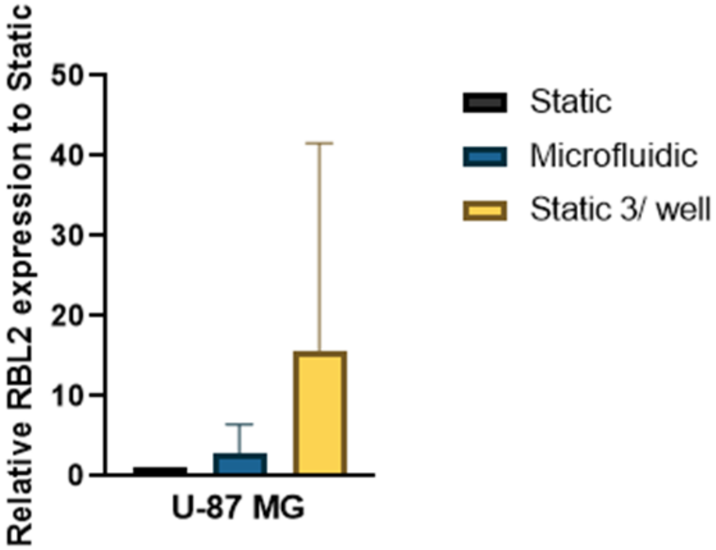

Figure 3.32. RT-qPCR analysis of U-87 MG spheroids incubated in either a static, microfluidic, or a static with 3 spheroids per well model, analysing RBL2 expression. Expression fold change against the primer, RPL13A as the control. Expression fold change of the microfluidic and static 3 spheroids/ well samples were each made relative to the static samples. Illustrates RBL2 expression fold change in U-87 MG cells with n=3, including the outlier repeat set. Error bars show the standard deviation. Ordinary one-way ANOVA performed.

Microscopic images were taken of the spheroids maintained in a static model with 3 spheroids/ well following incubation (Figure 3.33). The images demonstrated the effect of spheroids being maintained together, with the spheroids merging together after 72 hours of incubation within the same well.

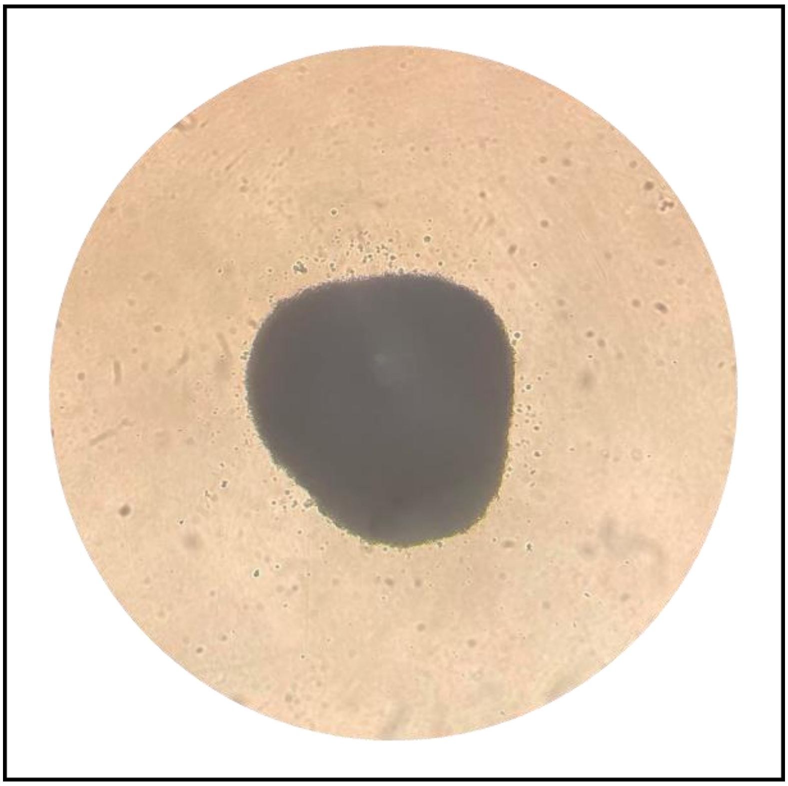

Figure 3.33. Microscopic images of 3, U-87 MG spheroids which have been maintained together in a static model, in a ULA plate. Following maintenance together for 96 hours, the 3 spheroids merged together to form a single structure. Images taken at 10x magnification, prior to collection for RT-qPCR.

Chapter 4. Discussion

The aim of this study was to determine the role of CBX2 in GBM, using RNA interference (RNAi) and overexpression techniques to alter the expression of the protein within the cells. The morphological effects of CBX2 depletion and overexpression were observed through microscopy, cell counts, and spheroid diameter analysis, with the expression of CBX2 seen to correlate with levels of cell growth.

Using two GBM cell lines, the effects of reducing CBX2 expression, through transfection of siRNA, were analysed in both 2D monolayer and 3D spheroid cell culture models. Three siRNA sequences specific for CBX2 knockdown were used in order to identify the most effective at gene knockdown. The effects were assessed using morphological observations, cell counts, spheroid diameter analysis, as well as western blotting to quantify CBX2 at the protein level, with RT-qPCR assessing changes at the mRNA level. This study utilised an existing microfluidic chip platform to analyse U-87 MG spheroids in a flowing system, over an extended period, so as to determine the effect of a static vs. dynamic model on CBX2 expression.

In addition to measuring CBX2 mRNA levels, RBL2 was also studied. It is reported that as a tumour suppressor, RBL2 may increase in expression when CBX2 expression is reduced. Evidence of RBL2 expression being regulated by the presence of CBX2 was explored in the Bilton et al. (2022) study, in which CBX2 expression was altered in breast cancer models through siRNA knockdown. Since CBX2 is classically associated with chromatin compaction, it is hypothesised that CBX2 may act as a repressor of tumour suppressors, enabling an increase in cell growth and proliferation; epigenetic regulation shown to drive cancer progression through the targeting of tumour suppressor gene expression (Papale et al., 2018). As such, RBL2 mRNA levels were also analysed following CBX2 knockdown.

Although the 2D models employed provided some insight into the effects of CBX2 in GBM cells, the limitations of such models in accurately replicating the TME require a more complex and representative model to better understand the role of CBX2 in GBM. The limitations of 2D models are fully outlined in Section 1.1.8.1. As such, spheroids were also employed to add key morphological features of the tumour, as seen *in vivo*, with steps towards microfluidic analysis also being taken. By using a spheroid model, key features of the TME can be represented, most importantly, the development of layers, including an outer proliferating layer and a necrotic core (Nath & Devi, 2016); also, this 3D model is capable of developing the different concentration gradients of oxygen and nutrients experienced within a tumour, with areas of hypoxia observed. Additionally, the spheroid model is able to better replicate the interaction between the tumour cells and the ECM, accepting the limitation that it is comprised of a single cell type (Aihara et al., 2016; Neufeld et al., 2021). However, it is worth noting that the spheroid model does fail to replicate the multiple different cell-cell interactions present *in vivo*, as well as the communication and interactions with immune cells.

Recently, a number of microfluidic devices capable of maintaining both U-87 MG spheroids and GBM tissue on a chip have been described (Sennett, 2019; Olubajo et al., 2020). However, no investigations into the effects of CBX2 using spheroids or tissue within a microfluidic model have been undertaken. Therefore, the current study provides a baseline from which CBX2 epigenetic alteration could be undertaken within a microfluidic model to determine the effect of CBX2 expression reduction and overexpression on cell growth within a dynamic model. For this purpose, 3D models (spheroids) were initially used, however the ultimate aim is to analyse resected tumour tissue within a microfluidic device.

4.1. Overview of Results

The current study investigated the effect of both the reduction and overexpression of CBX2 in the GBM cell lines, U-87 MG and SNB-19. The effects of which were observed through the altered growth of cells in a 2D model, and as spheroids for a 3D model. U-87 MG cells were also grown as spheroids and then maintained within a microfluidic device as part of the initial stages of development towards an siRNA knockdown or overexpression based experiment of spheroids (or even tissue) maintained within a microfluidic device.

Morphological observation and cell counting showed a reduction in cell density following siRNA knockdown in a 2D model of GBM, using U-87 MG cells, with siCBX2 #4 proving the most efficient in reducing cell number (cell count data). Results displayed in 2D models demonstrated that a reduction of CBX2 expression led to a reduction in cell growth. As such it was discerned that the presence of CBX2 within established GBM cell lines (through a 2D model) promotes tumour growth and proliferation. This was further confirmed through RT-qPCR analysis, with a key result being a significant reduction of CBX2 within the SNB-19 2D model with two of the siRNA sequences. However, when analysing siRNA knockdown within the 3D model, no significant reduction in cell growth, through measuring of the spheroid diameters, was detected, suggesting an issue with siRNA uptake/ transfection efficiency. Western blotting of siRNA knockdown samples were variable in their results, and as such, it was not possible to reproduce the initial 2D and 3D western bands in either GBM cell line at the protein level. Further to this, preliminary analysis of the breast cancer cell lines, MDA-MB-231, MCF-7, and T47D, in 2D and 3D models following siRNA knockdown also failed to show protein expression following western blotting.

As there was a concern that the U-87 MG and SNB-19 cell lines had a relatively low abundance of CBX2, due to the lack of protein detected in repeat experiments, overexpression of CBX2 using plasmids was performed. Transfection of the plasmids, full length CBX2 (72 kDa) and a CBX2 variant, missing the chromodomain (Kawaguchi et al., 2017), produced appropriately sized bands, with additional lower molecular weight breakdown or splice products also identified. These bands were of different molecular weights to those observed in siRNA knockdown experiments and in the U-87 MG positive control, when using the same anti-CBX2 monoclonal antibody. Additional CBX2 overexpression experiments are required to elucidate the origin and significance of these lower molecular weight bands.

Although morphological observation and cell counting showed an increase in cell density following CBX2 overexpression in a 2D model within a GBM model, changes in cell count were non-significant when comparing the pFLAG control plasmid to the cells transfected with the CBX2 full length construct. The data shows that there was an effect on the growth of cells, and therefore further optimisation of the protocol may be required to confirm observations; however, it may just be that there is no effect on cell growth following overexpression with the full length CBX2 construct.

Incubation of U-87 MG spheroids in a static and microfluidic model did not significantly alter the expression of CBX2 when analysed using RT-qPCR. However, there appeared to be a general increase in CBX2 expression within the microfluidic model compared to the static samples which had been maintained as 1 spheroid per well. Further to this, there was an increase (although not significant) within the static model of 3 spheroids per well, when compared to the microfluidic model. RBL2 expression mirrored CBX2 expression, with RBL2 expression decreasing in the microfluidic model compared to the static samples. It is thought the CBX2 acts as a suppressor of tumour suppressors, including RBL2. These results demonstrate that when CBX2 expression is increased, RBL2 expression is decreased, suggesting this is the case. Further analysis is required to confirm this.

4.2. CBX2 Expression in Cell lines

A key factor of this investigation was the identification of CBX2 bands through western blotting. Despite trouble in replicating initial western results, a CBX2 band was observed consistently with a molecular weight of approximately 52 kDa. The molecular weight of 52 kDa was seen in all siRNA knockdown experiments, as well as in the full flask lysates of two GBM (U-87 MG and SNB-19) and three breast cancer cell lines (MDA-MB-231, MCF-7, and T47D), which correlates with the predicted molecular weight recognised by the antibody used (ab80044, Abcam). The only occasion where the molecular weight of the observed CBX2 band was altered, were in the lysates which had been transfected with plasmids containing full length or chromodomain-deleted CBX2 constructs. Following the addition of this full length CBX2 containing plasmid, the resulting western blot indicated a higher molecular weight band at 72 kDa in two GBM cell lines.

In the literature, considerable variation has been observed regarding the observed molecular weight for CBX2, with different groups reporting contradictory findings. A summary of key studies which have observed CBX2 at the protein level through western blots can be seen in Table 4.1.

Table 4.1. Summary of key studies using a CBX2 antibody for analysis at the protein level.

Tumour type	Cell lines used	Antibody used	Predicted and observed MW by supplier	Observed molecular weight in study	Experimental study
Breast cancer	MDA-MB-231 MDA-MB-468 Hs578T	Anti-CBX2 antibody (ab80044).	Predicted MW = 56 kDa Observed MW = 52 kDa	70 kDa	Bilton et al. (2022)
Colorectal cancer	HCT116 HT29	Anti-CBX2 antibody (ab80044).	Predicted MW = 56 kDa Observed MW = 52 kDa	52 kDa	Zhou et al. (2021)
Glioma	U87 U251 LN229	Anti-CBX2 antibody (ab235305).	Predicted MW = 56 kDa	37 kDa	Wang et al. (2021)
Gastric cancer	GES-1 MFC (murine) HGC-27 AGS MKN-45	Anti-CBX2 antibody (ab235305).	Predicted MW = 56 kDa	Not stated	Zeng et al. (2021)
Ovarian cancer	SKOV3 OVCAR3	Anti-CBX2 antibody (ab80044).	Predicted MW = 56 kDa Observed MW = 52 kDa	Not specified	Dou et al. (2020)
Breast cancer	MDA-MB-231 MCF-7	Anti-CBX2 rabbit monoclonal antibody from the Proteintech Group, unspecified.	Available CBX2 monoclonal antibody from Proteintech Group - Cat no. 68244-1-Ig Predicted MW = 56 kDa Observed MW = between 65-70 kDa	56 kDa	Zheng et al. (2019)
Human embryonic kidney	293T	Anti-CBX2 antibody (ab80044).	Predicted MW = 56 kDa Observed MW = 52 kDa	73 kDa	Kawaguchi et al. (2017)

The closest study to the knockdown of CBX2 in brain tumour cells is seen in the work of Wang et al. (2021) who used shRNA to knockdown the expression of CBX2, using a 2D and murine model; the murine model consisted of the injection of cells which had been transfected with CBX2-shRNA into the brains of mice. An interesting point to note is the reported molecular weight of CBX2 following shRNA knockdown, with a protein of 37 kDa seen. Other groups have reported CBX2 to have a molecular weight between 52-56 kDa, or approximately 70 kDa (Table 4.1). The 37 kDa CBX2 band seen by Wang et al. (2021) was detected using the anti-CBX2 antibody, ab235305, purchased from Abcam. However, this differs from the predicted band size highlighted by Abcam, with a molecular weight of 56 kDa predicted for CBX2 when using this antibody.

It is clear that there is variation in the molecular weight both predicted and observed when investigating CBX2 at the protein level, with different studies reporting various findings. It is possible that different antibody clones pick up different forms of CBX2, which may account for the differing band sizes observed between studies. Additionally, there is the possibility that different splice variants are observed, further adding to the disparity between studies. There are two main isoforms of CBX2, one with a nucleotide length of 4628, and a shorter one at only 1107 nucleotides long; it is possible that different variants of the CBX2 protein are observed (NCBI). A further consideration to be made is whether the CBX2 variant observed is different between tumour types. A comprehensive study of multiple tumour types using multiple CBX2 antibodies would provide a complete understanding of what molecular weight is typically observed in different tumours. This would aid in future epigenetic alteration experiments in which the expression of CBX2 is observed at the protein level.

As demonstrated in Figure 3.22, the molecular weight of CBX2 was seen at 52 kDa for each cell line within the current study. This corresponds with the observed molecular weight for the Abcam antibody used; anti-CBX2 antibody ab80044. A molecular weight of 52 kDa using the anti-CBX2 antibody, ab80044, was also observed within the Zhou et al. (2021) study, in which CBX2 was detected within colorectal cancer.

Interestingly, for all three breast cancer cell lines observed, a band at 52 kDa was seen, which is in contrast to that observed by Bilton et al. (2022) who observed CBX2 at 70 kDa, whilst using the same antibody and cell line, MDA-MB-231. Kawaguchi et al. (2017) also observed CBX2 at a higher molecular weight of 73 kDa using the same antibody, but with a human embryonic kidney cell line (293T). A deeper look into the possible reason for the differing molecular weights is required.

4.3. Knockdown of CBX2

Knockdown of CBX2 expression was facilitated by the addition of CBX2-targeting siRNA's within this study. Alternatively, shRNA have been used for the same effect, with the Wang et al. (2021) group using shRNA to reduce the expression of CBX2 within the U-87 MG cell line. The mRNA level of CBX2 in a 2D U-87 MG model, compared to the control, was seen to be significantly reduced following transfection. They also demonstrated that a reduction in CBX2 led to a decrease in cell proliferation. The findings of the current study are in agreement with previous work, as a decrease in cell growth and proliferation following the addition of a knockdown agent (in this case siRNA) was observed by cell counting. Visual inspection of the cells also confirmed this.

Although knockdown of CBX2 within three breast cancer cell lines (MDA-MB-231, MCF-7, and T47D) was attempted for this investigation, visualisation of CBX2 expression at the protein level could not be achieved, most likely due to issues of low CBX2 expression. However, notably the Bilton et al. (2022) study was able to significantly reduce the cell count of MDA-MB-231, MDA-MB-468, and Hs578T breast cancer cells, and therefore cell growth in a 2D model. This study used three CBX2 targeting siRNA to reduce the expression of CBX2 within the cells. As with the current study, Bilton and colleagues also used Lipofectamine RNAiMAX to facilitate the introduction of siRNA into the cells. A marked reduction in CBX2 expression was observed in the test conditions when compared to the non-silencing, siScr control in all three breast cancer cell lines. However, this study did not explore the capabilities of siRNA in reducing CBX2 expression in a 3D model.

The current study highlighted a possible problem in the efficiency of the knockdown process. Although siRNA knockdown proved successful with siCBX2 #4 in the U-87 MG cell line, the other two siRNA products used did not significantly reduce cell numbers following transfection and incubation. Observation of CBX2 at the mRNA level through RT-qPCR highlighted only two instances of successful reduction in CBX2 expression. Specifically, a reduction in CBX2 following siRNA knockdown using siCBX2 #3 and 4 within the SNB-19 2D model. However, for all other siRNA knockdown experiments at the mRNA level, in both 2D and 3D models, RT-qPCR was unable to detect any significant changes in CBX2 expression between the siScr control and the siRNA knockdown products used.

Notably, no such significant reduction in spheroid diameter (equated to cell growth), or CBX2 expression was identified in any 3D model. Consequently, this may highlight a problem in siRNA knockdown efficiency specifically within the spheroid model, with the transfection agent not able to fully interact with all the cells. This observation was also seen by Morgan et al. (2018) who identified that siRNA uptake was limited in 3D models, specifically spheroids, and that an improved transfection method was necessary; this group looked to alter serum levels within the transfection media to aid in uptake.

The observation of reduced knockdown efficiency within the spheroids may be a more accurate representation of how a tumour may react to the addition of siRNA, due to the reduced surface: volume ratio. It is well known that the core of a spheroid represents the necrotic areas of the tumour which are unlikely to be affected by siRNA. Therefore, further optimisation of the siRNA knockdown protocol and alternative methods of transfection may prove more successful in reducing the expression of the CBX2 protein in GBM. Initial steps should look to transfecting a higher concentration of siRNA products into the cells to instil a greater response. Additionally, longer incubation times or adding supplementary siRNA reagents during incubation may improve RNA interference of CBX2 at the protein and mRNA level.

Alternative knockdown methods, including the use of shRNA, as opposed to siRNA may improve knockdown efficiency. Further to this, the construction of alternative CBX2-targeting siRNA for testing, or the use of different transfection reagents may improve transfection efficiency. One possible gene silencing route would be through the use of an Accell siRNA reagent, which has been reported as an effective RNA interference mechanism against difficult to transfect cells. Crucially, Accell siRNA does not require the use of a transfection agent such as lipofectamine, which may be the cause for inefficient siRNA uptake in GBM cell lines (Chong et al., 2013). Studies have shown that Accell siRNA induced gene silencing is capable of significantly reducing expression at both the protein and mRNA level (Ruigrok et al., 2018; Taniguchi et al., 2020). In particular, Ruigrok et al. (2018) demonstrated the efficiency of Accell siRNA within a tissue slice model, showing a possible avenue for future work in GBM tissue siRNA knockdown.

A key feature of CBX2 knockdown is the consequential increase in RBL2 expression at the mRNA level. Although not significant, perhaps due to knockdown efficiency, the initial observations with the 2D siRNA knockdown of the U-87 MG cell line indicates that when CBX2 expression is reduced, RBL2 expression is elevated. This correlates with the observations seen by Bilton et al. (2022), and as such further suggests a link between CBX2 and its role as a suppressor of tumour suppressor genes, which enables the promotion of tumour proliferation and growth.

4.4. Overexpression of CBX2

Overexpression of CBX2 within the GBM cell lines, U-87 MG and SNB-19 has not been performed previously. The current study was able to demonstrate that the introduction of CBX2 under a strong promotor alters expression at the protein level. Most importantly, the same pattern of CBX2 expression was observed in both the U-87 MG and SNB-19 cell lines when visualised through western blotting with an anti-

CBX2 antibody (Figures 3.26 and 3.28). Although not significant when compared to the pFLAG control, cell number was altered following addition of a full length CBX2 sequence or a CBX2 molecule missing the chromobox domain. The lack of significant increase in CBX2 expression at the mRNA level may be due to the efficiency of the plasmid uptake process. Further to this, the version of CBX2 which was encouraged to be produced by the cells by the plasmids may have competed with the native CBX2, preventing complete overexpression. The plasmids used to initiate an increase in CBX2 expression were provided by Kawaguchi et al. (2017). Incidentally, the Kawaguchi et al. (2017) group also looked to decrease the expression of CBX2, and were able to successfully do so, as seen at the protein level.

CBX2 overexpression was performed previously by Wang et al. (2021) using the LN229 (GBM) cell line. Following transfection, they observed an increase in cell number, with western blotting revealing a slight increase in CBX2 expression; however, the molecular weight of the 'CBX2 band' was only 37 kDa. Furthermore, unlike the current study, Wang et al. (2021) did not see any breakdown products or splice variants.

4.5. Microfluidic Application

This study outlines initial exploration of how CBX2 expression is affected by a continuous flow system, as opposed to a static system using a 3D, spheroid model. It was observed that there was no significant difference in CBX2 and RBL2 expression between static and dynamic systems. This is promising for future work, as it suggests that 3D static and 3D microfluidic siRNA knockdown experiments can be utilised. However further investigation into this is required to determine the effect of a dynamic continuous flow system on the expression of CBX2, as well as related proteins, within spheroids and tissue samples.

Interestingly, the spheroids maintained as three spheroids per well in the static model merged together to form one structure following incubation, more accurately replicating the events which occurred on-chip (Figure 3.33); it was noted that in some cases the spheroids maintained within the microfluidic chips also bonded together. However such spheroids did sometimes separate during extraction from the chips during collection; these observations were also seen in the study by Marsh (2022). The merging of the spheroids within the chip may account for the slight change in CBX2 expression at the mRNA level.

4.6. Limitations of Current Study

4.6.1. Cell Lines

It was important to verify the effects of CBX2 knockdown on multiple cell lines to ensure that the addition of siRNA to alter expression was not a cell line specific effect. The use of additional GBM cell lines would strengthen conclusions from the work, i.e., Li et al. (2017) reported that the U-251 cell line may express proteins differently when compared to U-87 MG cells. Other cell lines such as LN229, used as part of the Wang et al. (2021) study to CBX2 overexpression, could be analysed. Additionally, Wang et al. (2021) also used U-87 MG cells to form xenografts within immunocompromised mice; further work using other GBM cell lines to form xenografts would improve the understanding of CBX2 RNAi within a murine model. However, the limitations of established cell lines are well known, with it being accepted that primary cell lines would greatly benefit future studies in the development of new therapeutic methods (Gillet et al., 2011). Crucially, primary cell lines preserve more of the key morphological features seen *in vivo*, and as such provide greater accuracy in testing.

4.6.2. Western Blot Analysis

Having completed numerous repeats of both the U-87 MG and SNB-19, 2D and 3D siRNA knockdown experiments, the initial western blot with bands present (Figure 3.4), illustrating the presence of CBX2, could not be repeated. It can be said that there may be limitations to the use of the CBX2 antibody purchased, due to the lack of repeat western blots able to be completed with bands present. A possible cause for the lack of bands present in some repeats may be due to low expression of CBX2 within the GBM cell lines analysed. The use of an alternative anti-CBX2 antibody may provide clarity. However, expression of CBX2 within GBM may be generally low; RNA sequencing would need to be used to verify this.

It was noted that CBX2 expression was also too low to be identified at the protein level in the breast cancer cell lines used in this study, showing that the problem was not restricted to GBM.

4.7. Future Direction

There are several possible avenues to further evaluate the possible use of RNAi to reduce CBX2 expression within GBM. These include additional repeat experiments, testing of additional cell lines, particularly moving to primary cell lines, as well as using tissue biopsies. It is also important to target other genes to show the widespread application of the approach.

Due to the variation in CBX2 molecular weight observed between studies, a comprehensive analysis of the predicted and observed molecular weight of CBX2 within a range of cell lines using multiple anti-CBX2 antibodies would provide information as to what bands were recognised in which cells. Additionally, such an investigation would also allow us to improve our understanding of the tumour and target protein biology. The evaluation of CBX2 expression at the protein level in different tumour types would also be interesting to explore.

As noted, there may be an issue with transfection efficiency of the CBX2-targetting siRNA applied to GBM cell lines, and as such further optimisation is required. Key issues include, using different concentrations of siRNA, different incubation times and strategies, as well as exploring different CBX2-targetting siRNA sequences which may be more effective. As seen within the current study, siCBX2 #4 was more effective at eliciting a response than the other siCBX2 versions used. An additional set of experiments to consider would include the transfection of supplementary siRNA 24/48 hours after the initial transfection to take into consideration protein half-life and cell doubling time. For example, based on the growth profile provided by ECACC (n.d) the cell doubling time of U-87 MG cells is approximately 15 hours.

Additional quantification techniques to analyse the effects of siRNA knockdown on spheroids would include the use of a live-dead assay on the spheroid model. This assay could help determine transfection efficiency as well as the effects of reduced CBX2 expression on cell growth and proliferation. The live-dead assay experiments could be run in parallel with spheroid diameter measurements taken using the Gelcount.

Having laid the foundation for testing of GBM spheroid CBX2 expression within a microfluidic model, after assessing the effect of a static versus a dynamic, microfluidic system, testing of GBM cell line spheroids within the microfluidic environment with the addition of a siRNA knockdown component, would allow for a more representative response of GBM to epigenetic regulation of CBX2. Within this model, both a reduction and overexpression of CBX2 within the cells could be applied. The combination of siRNA knockdown of CBX2 and microfluidics could form the part of future projects undertaken on GBM, developing alternative therapeutic approaches. The microfluidic model would allow continuous flow of both fresh media and CBX2-targetting siRNA over the spheroids held within the chip.

Further to this, adaptation or designing of a microfluidic chip capable of maintaining clinical GBM samples, obtained from patients undergoing GBM resection, would provide a more clinically relevant investigation into the effects of epigenetic regulation of key proteins within GBM as a way of reducing growth. Specifically, this model could be used to reduce the expression of CBX2 within GBM tissue whilst also maintaining the tissue on chip for extended periods to better mimic the *in vivo* response. Either tissue lumps or slices (350 - 450μm) could be used to this effect, with tissue slices providing a cross section of the tumour sample. However, tissue slicing requires the use of a vibratome which is time consuming and can affect tissue structure and viability.

Using a microfluidic model, multiple analysis techniques could be used to assess the effects of CBX2 reduction, with analysis of effluent produced during maintenance being a key tool for observing cell viability post-incubation within the microfluidic device. Possible cell death markers which could be used to assess cell viability include that of LDH, released following membrane damage, as well as dead-cell protease (DCP) (Saito et al., 2012; Riley et al., 2019). Both would be suitable markers to measure the effects of CBX2 siRNA knockdown in a microfluidic model. For example, Riley et al. (2019) used LDH and DCP assays to measure cell damage and death by analysing the effluent produced during maintenance, measuring the cell damage markers released from thyroid tumour tissue. These assays, along with an MTS assay, which measures cell metabolism (which can be used to determine cell proliferation), could also be performed on the supernatant present within the 2D and 3D models.

Tissue analysis would further elucidate the role of CBX2 in GBM. Tissue, both pre- and post- maintenance within a microfluidic device with siCBX2 treated media, could be prepared for histological Haematoxylin and Eosin (H&E) staining or immunohistochemistry (IHC) analysis, through paraffin embedding or using fresh-frozen tissue. By analysing the tissue collected, any morphological changes experienced under different conditions can be identified, i.e., following transfection of different siRNA; markers such as Ki67 may also be used as part of IHC to evaluate levels of proliferation between samples (Riley et al., 2019; Joosten et al., 2021).

Chapter 5. Conclusion

For the first time, the role of CBX2 within GBM has been explored using siRNA as a method to alter the gene expression of a molecule involved in epigenetic alteration. The role of CBX2 and its impact on GBM was analysed in two cells lines within a 2D and 3D model, with prospects of a microfluidic element also being analysed. The aim of such a study looked to assess the possibility for CBX2 to become a therapeutic target during the treatment of the highly aggressive and difficult to treat, GBM. Whilst being highly invasive and proliferative, treatment issues surrounding incomplete surgical removal, inter- and intra- heterogeneity, as well as radio- and chemo-resistance are frequently observed. Consequently, the need for new therapeutic methods is keenly sought, with epigenetic alteration of key proteins being explored.

Whilst only in its initial stages, the use of siRNA in the U-87 MG and SNB-19 cell lines, as explored in the 2D and 3D models, does indicate some positive applications of reducing CBX2 within GBM. Most prevalently observed within the morphological analysis of the U-87 MG cells as well as through the cell counts following transfection and incubation with the siCBX2 #4 siRNA, the tests indicate a significant decrease in cell growth when CBX2 expression was also reduced. However, this study does highlight the need for the development of a more robust transfection protocol which can consistently induce the cells to produce less CBX2, as the results displayed following RT-qPCR analysis does not reflect the changes in CBX2 expected following the knockdown process, with a significant reduction of CBX2 at the mRNA level only observed within the SNB-19 cell line in the 2D model.

This investigation also explored for the first time the overexpression of CBX2 in both U-87 MG and SNB-19 cells using constructed plasmids to observe the effect of increasing CBX2 expression on cell growth (both morphologically and through cell counts) within a 2D model. Promising results were observed at the protein level. Although not statistically significant, the cell counts performed on the 2D overexpression experiments on the U-87 MG cell line demonstrated that there was an increase in cell number, and therefore growth following the addition of a plasmid with the full length CBX2 sequence present, when compared to the control plasmid.

Crucially, in the wider context, this suggests that the upregulation of CBX2 within GBM promotes tumour cell growth and progression. This factor is consistent with previous studies which found that CBX2 was upregulated in several tumour types, including, breast cancer, gastric cancer, gliomas, and GBM (Zheng et al., 2019; Zeng et al., 2021; Li et al., 2022). As such, a tentative link can be made towards the presence of CBX2 and the promotion of tumour progression.

Currently, few studies have looked to evaluate the effects of CBX2 on tumour growth, with only one other study thus far being directed towards the relationship between CBX2 and gliomas. Consequently, there is a need to pursue the role of CBX2 as a possible repressor of tumour suppressors within GBM, due to the key observations of reduced cell count and therefore reduced growth occurring when the expression of CBX2 is reduced. Most importantly, if CBX2 can be identified as reducing the effectiveness of tumour suppressors, therapeutic targeting through epigenetic regulation of the protein may be a viable treatment option. However, the need for additional models is necessary for the role of CBX2 to be explored in more detail. Such models include additional established cell lines, primary cell lines, multicellular 3D models, as well as patient tissue maintained for extended periods within a microfluidic device, to better mimic the TME. Future studies should look to expand our understanding of the role of CBX2 within GBM, by what mechanisms this occurs, as well as begin to utilise the therapeutic capabilities of reducing CBX2 expression in the treatment of GBM.

References

Abudurexiti, Y., Gu, Z., Chakma, K., Hata, T., Motoi, F., Unno, M., Horii, A. & Fukushige, S. (2020) Methylation-mediated silencing of the LIM homeobox 6 (LHX6) gene promotes cell proliferation in human pancreatic cancer. *Biochem Biophys Res Commun*, 526(3), 626-632.

Ahir, B. K., Engelhard, H. H. & Lakka, S. S. (2020) Tumor Development and Angiogenesis in Adult Brain Tumor: Glioblastoma. *Mol Neurobiol*, 57(5), 2461-2478.

Aihara, A., Abe, N., Saruhashi, K., Kanaki, T. & Nishino, T. (2016) Novel 3-D cell culture system for in vitro evaluation of anticancer drugs under anchorage-independent conditions. *Cancer Sci*, 107(12), 1858-1866.

Aithal, M. G. & Rajeswari, N. (2015) Validation of housekeeping genes for gene expression analysis in glioblastoma using quantitative real-time polymerase chain reaction. *Brain Tumor Res Treat*, 3(1), 24-9.

Akay, M., Hite, J., Avci, N. G., Fan, Y., Akay, Y., Lu, G. & Zhu, J. J. (2018) Drug Screening of Human GBM Spheroids in Brain Cancer Chip. *Sci Rep*, 8(1), 15423.

Algarni, A., Greenman, J. & Madden, L. A. (2019) Procoagulant tumor microvesicles attach to endothelial cells on biochips under microfluidic flow. *Biomicrofluidics*, 13(6), 064124.

Angelastro, J. M. & Lamé, M. W. (2010) Overexpression of CD133 promotes drug resistance in C6 glioma cells. *Mol Cancer Res*, 8(8), 1105-15.

Aranda, S., Mas, G. & Di Croce, L. (2015) Regulation of gene transcription by Polycomb proteins. *Sci Adv*, 1(11), e1500737.

Atat, O. E., Farzaneh, Z., Pourhamzeh, M., Taki, F., Abi-Habib, R., Vosough, M. & El-Sibai, M. (2022) 3D modeling in cancer studies. *Hum Cell*, 35(1), 23-36.

Audia, J. E. & Campbell, R. M. (2016) Histone Modifications and Cancer. *Cold Spring Harb Perspect Biol*, 8(4), a019521.

Ayuso, J. M., Monge, R., Martínez-González, A., Virumbrales-Muñoz, M., Llamazares, G. A., Berganzo, J., Hernández-Laín, A., Santolaria, J., Doblaré, M., Hubert, C., Rich, J. N., Sánchez-Gómez, P., Pérez-García, V. M., Ochoa, I. & Fernández, L. J. (2017) Glioblastoma on a microfluidic chip: Generating pseudopalisades and enhancing aggressiveness through blood vessel obstruction events. *Neuro Oncol*, 19(4), 503-513.

Bahcecioglu, G., Basara, G., Ellis, B. W., Ren, X. & Zorlutuna, P. (2020) Breast cancer models: Engineering the tumor microenvironment. *Acta Biomater*, 106, 1-21.

Bahmani, P., Schellenberger, E., Klohs, J., Steinbrink, J., Cordell, R., Zille, M., Müller, J., Harhausen, D., Hofstra, L., Reutelingsperger, C., Farr, T. D., Dirnagl, U. & Wunder, A. (2011) Visualization of cell death in mice with focal cerebral ischemia using fluorescent annexin A5, propidium iodide, and TUNEL staining. *J Cereb Blood Flow Metab*, 31(5), 1311-20.

Bao, S., Wu, Q., McLendon, R. E., Hao, Y., Shi, Q., Hjelmeland, A. B., Dewhirst, M. W., Bigner, D. D. & Rich, J. N. (2006) Glioma stem cells promote radioresistance by preferential activation of the DNA damage response. *Nature*, 444(7120), 756-60.

Bar, E. E. (2011) Glioblastoma, cancer stem cells and hypoxia. *Brain Pathol*, 21(2), 119-29.

Baratchian, M., Tiwari, R., Khalighi, S., Chakravarthy, A., Yuan, W., Berk, M., Li, J., Guerinot, A., de Bono, J., Makarov, V., Chan, T. A., Silverman, R. H., Stark, G. R., Varadan, V., De Carvalho, D. D., Chakraborty, A. A. & Sharifi, N. (2022) H3K9 methylation drives resistance to androgen receptor-antagonist therapy in prostate cancer. *Proc Natl Acad Sci U S A*, 119(21), e2114324119.

Barbour, H., Daou, S., Hendzel, M. & Affar, E. B. (2020) Polycomb group-mediated histone H2A monoubiquitination in epigenome regulation and nuclear processes. *Nat Commun*, 11(1), 5947.

Barzegar Behrooz, A., Syahir, A. & Ahmad, S. (2019) CD133: beyond a cancer stem cell biomarker. *J Drug Target*, 27(3), 257-269.

Bass, J. J., Wilkinson, D. J., Rankin, D., Phillips, B. E., Szewczyk, N. J., Smith, K. & Atherton, P. J. (2017) An overview of technical considerations for Western blotting applications to physiological research. *Scand J Med Sci Sports*, 27(1), 4-25.

Becker, A. P., Sells, B. E., Haque, S. J. & Chakravarti, A. (2021) Tumor Heterogeneity in Glioblastomas: From Light Microscopy to Molecular Pathology. *Cancers (Basel)*, 13(4), 761.

Bilton, L. J., Warren, C., Humphries, R. M., Kalsi, S., Waters, E., Francis, T., Dobrowinski, W., Beltran-Alvarez, P. & Wade, M. A. (2022) The Epigenetic Regulatory Protein CBX2 Promotes mTORC1 Signalling and Inhibits DREAM Complex Activity to Drive Breast Cancer Cell Growth. *Cancers (Basel)*, 14(14), 3491.

Biswas, S. & Rao, C. M. (2018) Epigenetic tools (The Writers, The Readers and The Erasers) and their implications in cancer therapy. *Eur J Pharmacol*, 837, 8-24.

Bogliotti, Y. S. & Ross, P. J. (2012) Mechanisms of histone H3 lysine 27 trimethylation remodeling during early mammalian development. *Epigenetics*, 7(9), 976-81.

Bower, R., Green, V. L., Kuvshinova, E., Kuvshinov, D., Karsai, L., Crank, S. T., Stafford, N. D. & Greenman, J. (2017) Maintenance of head and neck tumor on-chip: gateway to personalized treatment? *Future Sci OA*, 3(2), Fso174.

Brancato, V., Oliveira, J. M., Correlo, V. M., Reis, R. L. & Kundu, S. C. (2020) Could 3D models of cancer enhance drug screening? *Biomaterials*, 232, 119744.

Brat, D. J., Aldape, K., Colman, H., Holland, E. C., Louis, D. N., Jenkins, R. B., Kleinschmidt-DeMasters, B. K., Perry, A., Reifenberger, G., Stupp, R., von Deimling, A. & Weller, M. (2018) cIMPACT-NOW update 3: recommended diagnostic criteria for "Diffuse astrocytic glioma, IDH-wildtype, with molecular features of glioblastoma, WHO grade IV". *Acta Neuropathol*, 136(5), 805-810.

Brodbelt, A., Greenberg, D., Winters, T., Williams, M., Vernon, S. & Collins, V. P. (2015) Glioblastoma in England: 2007-2011. *Eur J Cancer*, 51(4), 533-542.

Brüningk, S. C., Rivens, I., Box, C., Oelfke, U. & Ter Haar, G. (2020) 3D tumour spheroids for the prediction of the effects of radiation and hyperthermia treatments. *Sci Rep*, 10(1), 1653.

Bruns, J., Egan, T., Mercier, P. & Zustiak, S. P. (2022) Glioblastoma spheroid growth and chemotherapeutic responses in single and dual-stiffness hydrogels. *Acta Biomater*, S1742-7061(22)00324-5.

Campisi, M., Shin, Y., Osaki, T., Hajal, C., Chiono, V. & Kamm, R. D. (2018) 3D self-organized microvascular model of the human blood-brain barrier with endothelial cells, pericytes and astrocytes. *Biomaterials*, 180, 117-129.

Carr, S. D., Green, V. L., Stafford, N. D. & Greenman, J. (2014) Analysis of radiation-induced cell death in head and neck squamous cell carcinoma and rat liver maintained in microfluidic devices. *Otolaryngol Head Neck Surg*, 150(1), 73-80.

Carvalho, B., Lopes, J. M., Silva, R., Peixoto, J., Leitão, D., Soares, P., Fernandes, A. C., Linhares, P., Vaz, R. & Lima, J. (2021) The role of c-Met and VEGFR2 in glioblastoma resistance to bevacizumab. *Sci Rep*, 11(1), 6067.

Cheah, L. T., Dou, Y. H., Seymour, A. M., Dyer, C. E., Haswell, S. J., Wadhawan, J. D. & Greenman, J. (2010) Microfluidic perfusion system for maintaining viable heart tissue with real-time electrochemical monitoring of reactive oxygen species. *Lab Chip*, 10(20), 2720-6.

Cheah, R., Srivastava, R., Stafford, N. D., Beavis, A. W., Green, V. & Greenman, J. (2017) Measuring the response of human head and neck squamous cell carcinoma to irradiation in a microfluidic model allowing customized therapy. *Int J Oncol*, 51(4), 1227-1238.

Chen, X., Liu, C., Muok, L., Zeng, C. & Li, Y. (2021) Dynamic 3D On-Chip BBB Model Design, Development, and Applications in Neurological Diseases. *Cells*, 10(11), 3183.

Chinot, O. L., Wick, W., Mason, W., Henriksson, R., Saran, F., Nishikawa, R., Carpentier, A. F., Hoang-Xuan, K., Kavan, P., Cernea, D., Brandes, A. A., Hilton, M., Abrey, L. & Cloughesy, T. (2014) Bevacizumab plus radiotherapy-temozolomide for newly diagnosed glioblastoma. *N Engl J Med*, 370(8), 709-22.

Chitturi Suryaprakash, R. T., Kujan, O., Shearston, K. & Farah, C. S. (2020) Three-Dimensional Cell Culture Models to Investigate Oral Carcinogenesis: A Scoping Review. *Int J Mol Sci*, 21(24), 9520.

Chong, R. H., Gonzalez-Gonzalez, E., Lara, M. F., Speaker, T. J., Contag, C. H., Kaspar, R. L., Coulman, S. A., Hargest, R. & Birchall, J. C. (2013) Gene silencing following siRNA delivery to skin via coated steel microneedles: In vitro and in vivo proof-of-concept. *J Control Release*, 166(3), 211-9.

Collins, T., Pyne, E., Christensen, M., Iles, A., Pamme, N. & Pires, I. M. (2021) Spheroid-on-chip microfluidic technology for the evaluation of the impact of continuous flow on metastatic potential in cancer models in vitro. *Biomicrofluidics*, 15(4), 044103.

Compter, I., Eekers, D. B. P., Hoeben, A., Rouschop, K. M. A., Reymen, B., Ackermans, L., Beckervordersantforth, J., Bauer, N. J. C., Anten, M. M., Wesseling, P., Postma, A. A., De Ruysscher, D. & Lambin, P. (2021) Chloroquine combined with concurrent radiotherapy and temozolomide for newly diagnosed glioblastoma: a phase IB trial. *Autophagy*, 17(9), 2604-2612.

Connelly, K. E. & Dykhuizen, E. C. (2017) Compositional and functional diversity of canonical PRC1 complexes in mammals. *Biochim Biophys Acta Gene Regul Mech*, 1860(2), 233-245.

Cuddapah, V. A., Robel, S., Watkins, S. & Sontheimer, H. (2014) A neurocentric perspective on glioma invasion. *Nat Rev Neurosci*, 15(7), 455-65.

Davis, M. E. (2016) Glioblastoma: Overview of Disease and Treatment. *Clin J Oncol Nurs*, 20(5 Suppl), S2-8.

De Francesco, E. M., Lappano, R., Santolla, M. F., Marsico, S., Caruso, A. & Maggiolini, M. (2013) HIF-1α/GPER signaling mediates the expression of VEGF induced by hypoxia in breast cancer associated fibroblasts (CAFs). *Breast Cancer Res*, 15(4), R64.

DeCordova, S., Shastri, A., Tsolaki, A. G., Yasmin, H., Klein, L., Singh, S. K. & Kishore, U. (2020) Molecular Heterogeneity and Immunosuppressive Microenvironment in Glioblastoma. *Front Immunol*, 11, 1402.

DeSantis, C. E., Ma, J., Gaudet, M. M., Newman, L. A., Miller, K. D., Goding Sauer, A., Jemal, A. & Siegel, R. L. (2019) Breast cancer statistics, 2019. *CA Cancer J Clin*, 69(6), 438-451.

Diaz, R. J., Ali, S., Qadir, M. G., De La Fuente, M. I., Ivan, M. E. & Komotar, R. J. (2017) The role of bevacizumab in the treatment of glioblastoma. *J Neurooncol*, 133(3), 455-467.

Dobrowinski, W. (2022) Investigating the importance of CBX2's structural motifs for its chromatin interactions and pro-oncogenic epigenetic regulatory function in triple negative breast cancer, MSc Thesis.

Doctor, A., Seifert, V., Ullrich, M., Hauser, S. & Pietzsch, J. (2020) Three-Dimensional Cell Culture Systems in Radiopharmaceutical Cancer Research. *Cancers (Basel)*, 12(10), 2765.

Doktorova, H., Hrabeta, J., Khalil, M. A. & Eckschlager, T. (2015) Hypoxia-induced chemoresistance in cancer cells: The role of not only HIF-1. *Biomed Pap Med Fac Univ Palacky Olomouc Czech Repub*, 159(2), 166-77.

Dominguez-Sola, D., Ying, C. Y., Grandori, C., Ruggiero, L., Chen, B., Li, M., Galloway, D. A., Gu, W., Gautier, J. & Dalla-Favera, R. (2007) Non-transcriptional control of DNA replication by c-Myc. *Nature*, 448(7152), 445-51.

Dou, Y., Chen, F., Lu, Y., Qiu, H. & Zhang, H. (2020) Effects of Wnt/β-Catenin Signal Pathway Regulated by miR-342-5p Targeting CBX2 on Proliferation, Metastasis and Invasion of Ovarian Cancer Cells. *Cancer Manag Res*, 12, 3783-3794.

Du, L., Li, X., Zhen, L., Chen, W., Mu, L., Zhang, Y. & Song, A. (2018) Everolimus inhibits breast cancer cell growth through PI3K/AKT/mTOR signaling pathway. *Mol Med Rep*, 17(5), 7163-7169.

ECACC (2022) *General Collection Browse.* Available online: https://www.culturecollections.org.uk/products/celllines/generalcell/browse.jsp [Accessed 21/12/2022].

ECACC (n.d) Growth Profile for Cell Line: U-87 MG. Available online: https://www.culturecollections.org.uk/media/53816/89081402-u-87-mg-growth-profile.pdf [Accessed 30/07/2023].

Edmondson, R., Broglie, J. J., Adcock, A. F. & Yang, L. (2014) Three-dimensional cell culture systems and their applications in drug discovery and cell-based biosensors. *Assay Drug Dev Technol*, 12(4), 207-18.

Eskilsson, E., Røsland, G. V., Solecki, G., Wang, Q., Harter, P. N., Graziani, G., Verhaak, R. G. W., Winkler, F., Bjerkvig, R. & Miletic, H. (2018) EGFR heterogeneity and implications for therapeutic intervention in glioblastoma. *Neuro Oncol*, 20(6), 743-752.

Eskilsson, E., Rosland, G. V., Talasila, K. M., Knappskog, S., Keunen, O., Sottoriva, A., Foerster, S., Solecki, G., Taxt, T., Jirik, R., Fritah, S., Harter, P. N., Välk, K., Al Hossain, J., Joseph, J. V., Jahedi, R., Saed, H. S., Piccirillo, S. G., Spiteri, I., Leiss, L., Euskirchen, P., Graziani, G., Daubon, T., Lund-Johansen, M., Enger, P., Winkler, F., Ritter, C. A., Niclou, S. P., Watts, C., Bjerkvig, R. & Miletic, H. (2016) EGFRvIII mutations can emerge as late and heterogenous events in glioblastoma development and promote angiogenesis through Src activation. *Neuro Oncol*, 18(12), 1644-1655.

Estrada, C. C., Maldonado, A. & Mallipattu, S. K. (2019) Therapeutic Inhibition of VEGF Signaling and Associated Nephrotoxicities. *J Am Soc Nephrol*, 30(2), 187-200.

Ewelt, C., Goeppert, M., Rapp, M., Steiger, H. J., Stummer, W. & Sabel, M. (2011) Glioblastoma multiforme of the elderly: the prognostic effect of resection on survival. *J Neurooncol*, 103(3), 611-8.

Fan, Y., Nguyen, D. T., Akay, Y., Xu, F. & Akay, M. (2016) Engineering a Brain Cancer Chip for High-throughput Drug Screening. *Sci Rep*, 6, 25062.

Fan, Y., Potdar, A. A., Gong, Y., Eswarappa, S. M., Donnola, S., Lathia, J. D., Hambardzumyan, D., Rich, J. N. & Fox, P. L. (2014) Profilin-1 phosphorylation directs angiocrine expression and glioblastoma progression through HIF-1α accumulation. *Nat Cell Biol*, 16(5), 445-456.

Fitzgerald, A. A., Li, E. & Weiner, L. M. (2020) 3D Culture Systems for Exploring Cancer Immunology. *Cancers (Basel)*, 13(1), 56.

Fomchenko, E. I. & Holland, E. C. (2006) Mouse models of brain tumors and their applications in preclinical trials. *Clin Cancer Res*, 12(18), 5288-97.

Foty, R. (2011) A simple hanging drop cell culture protocol for generation of 3D spheroids. *J Vis Exp,* (51), 2720.

Franchi-Mendes, T., Lopes, N. & Brito, C. (2021) Heterotypic Tumor Spheroids in Agitation-Based Cultures: A Scaffold-Free Cell Model That Sustains Long-Term Survival of Endothelial Cells. *Front Bioeng Biotechnol*, 9, 649949.

Freire-Benéitez, V., Pomella, N., Millner, T. O., Dumas, A. A., Niklison-Chirou, M. V., Maniati, E., Wang, J., Rajeeve, V., Cutillas, P. & Marino, S. (2021) Elucidation of the BMI1 interactome identifies novel regulatory roles in glioblastoma. *NAR Cancer*, 3(1), zcab009.

Gállego Pérez-Larraya, J. & Delattre, J. Y. (2012) Treating glioblastoma in the elderly. *CNS Oncol*, 1(2), 193-201.

Gan, E. S., Xu, Y. & Ito, T. (2015) Dynamics of H3K27me3 methylation and demethylation in plant development. *Plant Signal Behav*, 10(9), e1027851.

Gao, Z., Zhang, J., Bonasio, R., Strino, F., Sawai, A., Parisi, F., Kluger, Y. & Reinberg, D. (2012) PCGF homologs, CBX proteins, and RYBP define functionally distinct PRC1 family complexes. *Mol Cell*, 45(3), 344-56.

Geng, Z. & Gao, Z. (2020) Mammalian PRC1 Complexes: Compositional Complexity and Diverse Molecular Mechanisms. *Int J Mol Sci*, 21(22), 8594.

Gil, J. & O'Loghlen, A. (2014) PRC1 complex diversity: where is it taking us? *Trends Cell Biol*, 24(11), 632-41.

Gilbert, M. R., Dignam, J. J., Armstrong, T. S., Wefel, J. S., Blumenthal, D. T., Vogelbaum, M. A., Colman, H., Chakravarti, A., Pugh, S., Won, M., Jeraj, R., Brown, P. D., Jaeckle, K. A., Schiff, D., Stieber, V. W., Brachman, D. G., Werner-Wasik, M., Tremont-Lukats, I. W., Sulman, E. P., Aldape, K. D., Curran, W. J., Jr. & Mehta, M. P. (2014) A randomized trial of bevacizumab for newly diagnosed glioblastoma. *N Engl J Med*, 370(8), 699-708.

Gillet, J. P., Calcagno, A. M., Varma, S., Marino, M., Green, L. J., Vora, M. I., Patel, C., Orina, J. N., Eliseeva, T. A., Singal, V., Padmanabhan, R., Davidson, B., Ganapathi, R., Sood, A. K., Rueda, B. R., Ambudkar, S. V. & Gottesman, M. M. (2011) Redefining the relevance of established cancer cell lines to the study of mechanisms of clinical anti-cancer drug resistance. *Proc Natl Acad Sci U S A*, 108(46), 18708-13.

Goenka, A., Tiek, D., Song, X., Huang, T., Hu, B. & Cheng, S. Y. (2021) The Many Facets of Therapy Resistance and Tumor Recurrence in Glioblastoma. *Cells*, 10(3), 484.

Haar, C. P., Hebbar, P., Wallace, G. C. t., Das, A., Vandergrift, W. A., 3rd, Smith, J. A., Giglio, P., Patel, S. J., Ray, S. K. & Banik, N. L. (2012)

Drug resistance in glioblastoma: a mini review. *Neurochem Res*, 37(6), 1192-200.

Haj, A., Doenitz, C., Schebesch, K. M., Ehrensberger, D., Hau, P., Putnik, K., Riemenschneider, M. J., Wendl, C., Gerken, M., Pukrop, T., Brawanski, A. & Proescholdt, M. A. (2017) Extent of Resection in Newly Diagnosed Glioblastoma: Impact of a Specialized Neuro-Oncology Care Center. *Brain Sci*, 8(1).

Hanna, C., Kurian, K. M., Williams, K., Watts, C., Jackson, A., Carruthers, R., Strathdee, K., Cruickshank, G., Dunn, L., Erridge, S., Godfrey, L., Jefferies, S., McBain, C., Sleigh, R., McCormick, A., Pittman, M., Halford, S. & Chalmers, A. J. (2020) Pharmacokinetics, safety, and tolerability of olaparib and temozolomide for recurrent glioblastoma: results of the phase I OPARATIC trial. *Neuro Oncol*, 22(12), 1840-1850.

Hattersley, S. M., Greenman, J. & Haswell, S. J. (2011) Study of ethanol induced toxicity in liver explants using microfluidic devices. *Biomed Microdevices*, 13(6), 1005-14.

Hattersley, S. M., Sylvester, D. C., Dyer, C. E., Stafford, N. D., Haswell, S. J. & Greenman, J. (2012) A microfluidic system for testing the responses of head and neck squamous cell carcinoma tissue biopsies to treatment with chemotherapy drugs. *Ann Biomed Eng*, 40(6), 1277-88.

Hirschhaeuser, F., Menne, H., Dittfeld, C., West, J., Mueller-Klieser, W. & Kunz-Schughart, L. A. (2010) Multicellular tumor spheroids: an underestimated tool is catching up again. *J Biotechnol*, 148(1), 3-15.

Hsu, J. Y., Chang, C. J. & Cheng, J. S. (2022) Survival, treatment regimens and medical costs of women newly diagnosed with metastatic triple-negative breast cancer. *Sci Rep*, 12(1), 729.

Hu, F. F., Chen, H., Duan, Y., Lan, B., Liu, C. J., Hu, H., Dong, X., Zhang, Q., Cheng, Y. M., Liu, M., Guo, A. Y. & Xuan, C. (2022) CBX2 and EZH2 cooperatively promote the growth and metastasis of lung adenocarcinoma. *Mol Ther Nucleic Acids*, 27, 670-684.

Huang, M., Liu, T., Ma, P., Mitteer, R. A., Jr., Zhang, Z., Kim, H. J., Yeo, E., Zhang, D., Cai, P., Li, C., Zhang, L., Zhao, B., Roccograndi, L., O'Rourke, D. M., Dahmane, N., Gong, Y., Koumenis, C. & Fan, Y. (2016) c-Met-mediated endothelial plasticity drives aberrant vascularization and chemoresistance in glioblastoma. *J Clin Invest*, 126(5), 1801-14.

Huang, Z., Yu, P. & Tang, J. (2020) Characterization of Triple-Negative Breast Cancer MDA-MB-231 Cell Spheroid Model. *Onco Targets Ther*, 13, 5395-5405.

Hung, P. J., Lee, P. J., Sabounchi, P., Lin, R. & Lee, L. P. (2005) Continuous perfusion microfluidic cell culture array for high-throughput cell-based assays. *Biotechnol Bioeng*, 89(1), 1-8.

Hutchinson, L. & Kirk, R. (2011) High drug attrition rates--where are we going wrong? *Nat Rev Clin Oncol*, 8(4), 189-90.

Iwamoto, F. M., Reiner, A. S., Panageas, K. S., Elkin, E. B. & Abrey, L. E. (2008) Patterns of care in elderly glioblastoma patients. *Ann Neurol*, 64(6), 628-34.

Jain, R. K. (2003) Molecular regulation of vessel maturation. *Nat Med*, 9(6), 685-693.

Javed, Z., Worley, B. L., Stump, C., Shimko, S. S., Crawford, L. C., Mythreye, K. & Hempel, N. (2022) Optimization of Extracellular Flux Assay to Measure Respiration of Anchorage-independent Tumor Cell Spheroids. *Bio Protoc*, 12(4), e4321.

Jensen, C. & Teng, Y. (2020) Is It Time to Start Transitioning From 2D to 3D Cell Culture? *Front Mol Biosci*, 7, 33.

Joosten, S. E. P., Wellenstein, M., Koornstra, R., van Rossum, A., Sanders, J., van der Noort, V., Ferrandez, M. C., Harkes, R., Mandjes, I. A. M., Rosing, H., Huitema, A., Beijnen, J. H., Wesseling, J., van Diest, P. J., Horlings, H. M., Linn, S. C. & Zwart, W. (2021) IHC-based Ki67 as response biomarker to tamoxifen in breast cancer window trials enrolling premenopausal women. *NPJ Breast Cancer*, 7(1), 138.

Kapałczyńska, M., Kolenda, T., Przybyła, W., Zajączkowska, M., Teresiak, A., Filas, V., Ibbs, M., Bliźniak, R., Łuczewski, Ł. & Lamperska, K. (2018) 2D and 3D cell cultures - a comparison of different types of cancer cell cultures. *Arch Med Sci*, 14(4), 910-919.

Kauther, M. D., Xu, J. & Wedemeyer, C. (2010) Alpha-calcitonin gene-related peptide can reverse the catabolic influence of UHMWPE particles on RANKL expression in primary human osteoblasts. *Int J Biol Sci*, 6(6), 525-36.

Kawaguchi, T., Machida, S., Kurumizaka, H., Tagami, H. & Nakayama, J. I. (2017) Phosphorylation of CBX2 controls its nucleosome-binding specificity. *J Biochem*, 162(5), 343-355.

Kennedy, R., Kuvshinov, D., Sdrolia, A., Kuvshinova, E., Hilton, K., Crank, S., Beavis, A. W., Green, V. & Greenman, J. (2019) A patient tumour-on-a-chip system for personalised investigation of radiotherapy based treatment regimens. *Sci Rep*, 9(1), 6327.

Kim, J. B. (2005) Three-dimensional tissue culture models in cancer biology. *Semin Cancer Biol*, 15(5), 365-77.

Kim, M., Ladomersky, E., Mozny, A., Kocherginsky, M., O'Shea, K., Reinstein, Z. Z., Zhai, L., Bell, A., Lauing, K. L., Bollu, L., Rabin, E., Dixit, K., Kumthekar, P., Platanias, L. C., Hou, L., Zheng, Y., Wu, J., Zhang, B., Hrachova, M., Merrill, S. A., Mrugala, M. M., Prabhu, V. C., Horbinski, C., James, C. D., Yamini, B., Ostrom, Q. T., Johnson, M. O., Reardon, D. A., Lukas, R. V. & Wainwright, D. A. (2021) Glioblastoma as an age-related neurological disorder in adults. *Neurooncol Adv*, 3(1), vdab125.

Kim, S. H., Yoo, H., Chang, J. H., Kim, C. Y., Chung, D. S., Kim, S. H., Park, S. H., Lee, Y. S. & Yang, S. H. (2018) Procarbazine and CCNU Chemotherapy for Recurrent Glioblastoma with MGMT Promoter Methylation. *J Korean Med Sci*, 33(24), e167.

Kimura, H., Sakai, Y. & Fujii, T. (2018) Organ/body-on-a-chip based on microfluidic technology for drug discovery. *Drug Metab Pharmacokinet*, 33(1), 43-48.

Kimura, H., Yamamoto, T., Sakai, H., Sakai, Y. & Fujii, T. (2008) An integrated microfluidic system for long-term perfusion culture and on-line monitoring of intestinal tissue models. *Lab Chip*, 8(5), 741-6.

Koch, J., Mönch, D., Maaß, A., Gromoll, C., Hehr, T., Leibold, T., Schlitt, H. J., Dahlke, M. H. & Renner, P. (2021) Three dimensional cultivation increases chemo- and radioresistance of colorectal cancer cell lines. *PLoS One*, 16(1), e0244513.

Koppens, M. & van Lohuizen, M. (2016) Context-dependent actions of Polycomb repressors in cancer. *Oncogene*, 35(11), 1341-52.

Koshy, M., Villano, J. L., Dolecek, T. A., Howard, A., Mahmood, U., Chmura, S. J., Weichselbaum, R. R. & McCarthy, B. J. (2012) Improved survival time trends for glioblastoma using the SEER 17 population-based registries. *J Neurooncol*, 107(1), 207-12.

Krakstad, C. & Chekenya, M. (2010) Survival signalling and apoptosis resistance in glioblastomas: opportunities for targeted therapeutics. *Mol Cancer*, 9, 135.

Krieger, T. G., Tirier, S. M., Park, J., Jechow, K., Eisemann, T., Peterziel, H., Angel, P., Eils, R. & Conrad, C. (2020) Modeling glioblastoma invasion using human brain organoids and single-cell transcriptomics. *Neuro Oncol*, 22(8), 1138-1149.

Kusanto, B., Gordon, A., Naylor-Adamson, L., Atkinson, L., Coupland, C., Booth, Z., Ahmed, Y., Pires, I. M., Stasiuk, G. J., Sturmey, R., Calaminus, S. D. J. & Arman, M. (2021) Practical Considerations of Dissolved Oxygen Levels for Platelet Function under Hypoxia. *Int J Mol Sci*, 22(24), 13223.

Lee, S. H., Kim, Y. S., Han, W., Ryu, H. S., Chang, J. M., Cho, N. & Moon, W. K. (2016) Tumor growth rate of invasive breast cancers during wait times for surgery assessed by ultrasonography. *Medicine (Baltimore)*, 95(37), e4874.

Lesueur, P., Lequesne, J., Grellard, J. M., Dugué, A., Coquan, E., Brachet, P. E., Geffrelot, J., Kao, W., Emery, E., Berro, D. H., Castera, L., Goardon, N., Lacroix, J., Lange, M., Capel, A., Leconte, A., Andre, B., Léger, A., Lelaidier, A., Clarisse, B. & Stefan, D. (2019) Phase I/IIa study of concomitant radiotherapy with olaparib and temozolomide in unresectable or partially resectable glioblastoma: OLA-TMZ-RTE-01 trial protocol. *BMC Cancer*, 19(1), 198.

Levine, S. S., Weiss, A., Erdjument-Bromage, H., Shao, Z., Tempst, P. & Kingston, R. E. (2002) The core of the polycomb repressive complex is compositionally and functionally conserved in flies and humans. *Mol Cell Biol*, 22(17), 6070-8.

Li, B., Carey, M. & Workman, J. L. (2007) The role of chromatin during transcription. *Cell*, 128(4), 707-19.

Li, D. M., Chen, Q. D., Wei, G. N., Wei, J., Yin, J. X., He, J. H., Ge, X. & Shi, Z. M. (2020) Hypoxia-Induced miR-137 Inhibition Increased Glioblastoma Multiforme Growth and Chemoresistance Through LRP6. *Front Oncol*, 10, 611699.

Li, G., Warden, C., Zou, Z., Neman, J., Krueger, J. S., Jain, A., Jandial, R. & Chen, M. (2013) Altered expression of polycomb group genes in glioblastoma multiforme. *PLoS One*, 8(11), e80970.

Li, H., Lei, B., Xiang, W., Wang, H., Feng, W., Liu, Y. & Qi, S. (2017) Differences in Protein Expression between the U251 and U87 Cell Lines. *Turk Neurosurg*, 27(6), 894-903.

Li, J., Xu, Z., Zhou, L. & Hu, K. (2022) Expression profile and prognostic values of Chromobox family members in human glioblastoma. *Aging (Albany NY)*, 14(4), 1910-1931.

Li, Y. & Seto, E. (2016) HDACs and HDAC Inhibitors in Cancer Development and Therapy. *Cold Spring Harb Perspect Med*, 6(10), a026831.

Li, Z. (2013) CD133: a stem cell biomarker and beyond. *Exp Hematol Oncol*, 2(1), 17.

Li, Z. & Cui, Z. (2014) Three-dimensional perfused cell culture. *Biotechnol Adv*, 32(2), 243-54.

Lin, W., Wu, S., Chen, X., Ye, Y., Weng, Y., Pan, Y., Chen, Z., Chen, L., Qiu, X. & Qiu, S. (2020) Characterization of Hypoxia Signature to Evaluate the Tumor Immune Microenvironment and Predict Prognosis in Glioma Groups. *Front Oncol*, 10, 796.

Linkous, A., Balamatsias, D., Snuderl, M., Edwards, L., Miyaguchi, K., Milner, T., Reich, B., Cohen-Gould, L., Storaska, A., Nakayama, Y., Schenkein, E., Singhania, R., Cirigliano, S., Magdeldin, T., Lin, Y., Nanjangud, G., Chadalavada, K., Pisapia, D., Liston, C. & Fine, H. A. (2019) Modeling Patient-Derived Glioblastoma with Cerebral Organoids. *Cell Rep*, 26(12), 3203-3211.e5.

Liu, W. H., Lin, J. C., Chou, Y. C., Li, M. H. & Tsai, J. T. (2020) CD44-associated radioresistance of glioblastoma in irradiated brain areas with optimal tumor coverage. *Cancer Med*, 9(1), 350-360.

Liu, Y. & Chen, Y. G. (2018) 2D- and 3D-Based Intestinal Stem Cell Cultures for Personalized Medicine. *Cells*, 7(12), 225.

Louis, D. N., Ohgaki, H., Wiestler, O. D., Cavenee, W. K., Burger, P. C., Jouvet, A., Scheithauer, B. W. & Kleihues, P. (2007) The 2007 WHO classification of tumours of the central nervous system. *Acta Neuropathol*, 114(2), 97-109.

Louis, D. N., Perry, A., Wesseling, P., Brat, D. J., Cree, I. A., Figarella-Branger, D., Hawkins, C., Ng, H. K., Pfister, S. M., Reifenberger, G., Soffietti, R., von Deimling, A. & Ellison, D. W. (2021) The 2021 WHO Classification of Tumors of the Central Nervous System: a summary. *Neuro Oncol*, 23(8), 1231-1251.

Lukas, R. V., Wainwright, D. A., Ladomersky, E., Sachdev, S., Sonabend, A. M. & Stupp, R. (2019) Newly Diagnosed Glioblastoma: A Review on Clinical Management. *Oncology (Williston Park)*, 33(3), 91-100.

Luo, L., Zhang, W., Wang, J., Zhao, M., Shen, K., Jia, Y., Li, Y., Zhang, J., Cai, W., Xiao, D., Bai, X., Liu, K., Wang, K., Zhang, Y., Zhu, H., Zhou, Q. & Hu, D. (2021) A Novel 3D Culture Model of Human ASCs Reduces Cell Death in Spheroid Cores and Maintains Inner Cell Proliferation Compared With a Nonadherent 3D Culture. *Front Cell Dev Biol*, 9, 737275.

Ma, C., Peng, Y., Li, H. & Chen, W. (2021a) Organ-on-a-Chip: A New Paradigm for Drug Development. *Trends Pharmacol Sci*, 42(2), 119-133.

Ma, R., Mandell, J., Lu, F., Heim, T., Schoedel, K., Duensing, A., Watters, R. J. & Weiss, K. R. (2021b) Do Patient-derived Spheroid Culture Models Have Relevance in Chondrosarcoma Research? *Clin Orthop Relat Res*, 479(3), 477-490.

Ma, R. G., Zhang, Y., Sun, T. T. & Cheng, B. (2014) Epigenetic regulation by polycomb group complexes: focus on roles of CBX proteins. *J Zhejiang Univ Sci B*, 15(5), 412-28.

MacAlpine, D. M. & Almouzni, G. (2013) Chromatin and DNA replication. *Cold Spring Harb Perspect Biol*, 5(8), a010207.

Malakpour-Permlid, A. & Oredsson, S. (2021) A novel 3D polycaprolactone high-throughput system for evaluation of toxicity in normoxia and hypoxia. *Toxicol Rep*, 8, 627-635.

Mao, J., Tian, Y., Wang, C., Jiang, K., Li, R., Yao, Y., Zhang, R., Sun, D., Liang, R., Gao, Z., Wang, Q. & Wang, L. (2019) CBX2 Regulates Proliferation and Apoptosis via the Phosphorylation of YAP in Hepatocellular Carcinoma. *J Cancer*, 10(12), 2706-2719.

Mao, X. G., Wang, C., Liu, D. Y., Zhang, X., Wang, L., Yan, M., Zhang, W., Zhu, J., Li, Z. C., Mi, C., Tian, J. Y., Hou, G. D., Miao, S. Y., Song, Z. X., Li, J. C. & Xue, X. Y. (2016) Hypoxia upregulates HIG2 expression and contributes to bevacizumab resistance in glioblastoma. *Oncotarget*, 7(30), 47808-47820.

Marsh, D. (2022) Establishing a Novel 3-Dimensional Microfluidic Model of Bunyavirus Infection to Characterise Exosome Release from Tumour Cells, MSc Thesis.

Massey, S. C., Urcuyo, J. C., Marin, B. M., Sarkaria, J. N. & Swanson, K. R. (2020) Quantifying Glioblastoma Drug Response Dynamics Incorporating Treatment Sensitivity and Blood Brain Barrier Penetrance From Experimental Data. *Front Physiol*, 11, 830.

Monteiro, A. R., Hill, R., Pilkington, G. J. & Madureira, P. A. (2017) The Role of Hypoxia in Glioblastoma Invasion. *Cells*, 6(4), 45.

Morgan, R. G., Chambers, A. C., Legge, D. N., Coles, S. J., Greenhough, A. & Williams, A. C. (2018) Optimized delivery of siRNA into 3D tumor spheroid cultures in situ. *Sci Rep*, 8(1), 7952.

Morrison, O. & Thakur, J. (2021) Molecular Complexes at Euchromatin, Heterochromatin and Centromeric Chromatin. *Int J Mol Sci*, 22(13), 6922.

Morton, C. L. & Houghton, P. J. (2007) Establishment of human tumor xenografts in immunodeficient mice. *Nat Protoc*, 2(2), 247-50.

Nacerddine, K., Beaudry, J. B., Ginjala, V., Westerman, B., Mattiroli, F., Song, J. Y., van der Poel, H., Ponz, O. B., Pritchard, C., Cornelissen-Steijger, P., Zevenhoven, J., Tanger, E., Sixma, T. K., Ganesan, S. & van Lohuizen, M. (2012) Akt-mediated phosphorylation of Bmi1 modulates its oncogenic potential, E3 ligase activity, and DNA damage repair activity in mouse prostate cancer. *J Clin Invest*, 122(5), 1920-32.

Nath, S. & Devi, G. R. (2016) Three-dimensional culture systems in cancer research: Focus on tumor spheroid model. *Pharmacol Ther*, 163, 94-108.

NCBI *Transcripts and Proteins; CBX2 – chromobox 2.* Available online: https://www.ncbi.nlm.nih.gov/datasets/gene/id/84733/products/ [Accessed 11/03/2024].

Neufeld, L., Yeini, E., Reisman, N., Shtilerman, Y., Ben-Shushan, D., Pozzi, S., Madi, A., Tiram, G., Eldar-Boock, A., Ferber, S., Grossman, R., Ram, Z. & Satchi-Fainaro, R. (2021) Microengineered perfusable 3D-bioprinted glioblastoma model for in vivo mimicry of tumor microenvironment. *Sci Adv*, 7(34).

NICE (2018) Brain tumours (primary) and brain metastases in over 16s. Available online: https://www.nice.org.uk/guidance/ng99/resources/brain-tumours-primary-and-brain-metastases-in-over-16s-pdf-1837763558341 [Accessed 26/04/2023].

NorthGene™ (2022) *Cell Line Authentication Services.* Available online: https://www.northgene.co.uk/cell-line-authentication/ [Accessed 03/05/2022].

Nunes, A. S., Barros, A. S., Costa, E. C., Moreira, A. F. & Correia, I. J. (2019) 3D tumor spheroids as in vitro models to mimic in vivo human solid tumors resistance to therapeutic drugs. *Biotechnol Bioeng*, 116(1), 206-226.

Ohgaki, H. & Kleihues, P. (2013) The definition of primary and secondary glioblastoma. *Clin Cancer Res*, 19(4), 764-72.

Okada, S., Vaeteewoottacharn, K. & Kariya, R. (2019) Application of Highly Immunocompromised Mice for the Establishment of Patient-Derived Xenograft (PDX) Models. *Cells*, 8(8), 889.

Olubajo, F., Achawal, S. & Greenman, J. (2020) Development of a Microfluidic Culture Paradigm for Ex Vivo Maintenance of Human Glioblastoma Tissue: A New Glioblastoma Model? *Transl Oncol*, 13(1), 1-10.

Ostrom, Q. T., Gittleman, H., Farah, P., Ondracek, A., Chen, Y., Wolinsky, Y., Stroup, N. E., Kruchko, C. & Barnholtz-Sloan, J. S. (2013) CBTRUS statistical report: Primary brain and central nervous system tumors diagnosed in the United States in 2006-2010. *Neuro Oncol*, 15 Suppl 2(Suppl 2), ii1-56.

Ostrom, Q. T., Patil, N., Cioffi, G., Waite, K., Kruchko, C. & Barnholtz-Sloan, J. S. (2020) CBTRUS Statistical Report: Primary Brain and Other Central Nervous System Tumors Diagnosed in the United States in 2013-2017. *Neuro Oncol*, 22(12 Suppl 2), iv1-iv96.

Paolillo, M., Comincini, S. & Schinelli, S. (2021) In Vitro Glioblastoma Models: A Journey into the Third Dimension. *Cancers (Basel)*, 13(10), 2449.

Papale, M., Ferretti, E., Battaglia, G., Bellavia, D., Mai, A. & Tafani, M. (2018) EZH2, HIF-1, and Their Inhibitors: An Overview on Pediatric Cancers. *Front Pediatr*, 6, 328.

Parbin, S., Kar, S., Shilpi, A., Sengupta, D., Deb, M., Rath, S. K. & Patra, S. K. (2014) Histone deacetylases: a saga of perturbed acetylation homeostasis in cancer. *J Histochem Cytochem*, 62(1), 11-33.

Patel, A. P., Tirosh, I., Trombetta, J. J., Shalek, A. K., Gillespie, S. M., Wakimoto, H., Cahill, D. P., Nahed, B. V., Curry, W. T., Martuza, R. L., Louis, D. N., Rozenblatt-Rosen, O., Suvà, M. L., Regev, A. & Bernstein, B. E. (2014) Single-cell RNA-seq highlights intratumoral heterogeneity in primary glioblastoma. *Science*, 344(6190), 1396-401.

Petreus, T., Cadogan, E., Hughes, G., Smith, A., Pilla Reddy, V., Lau, A., O'Connor, M. J., Critchlow, S., Ashford, M. & Oplustil O'Connor, L. (2021) Tumour-on-chip microfluidic platform for assessment of drug pharmacokinetics and treatment response. *Commun Biol*, 4(1), 1001.

Qazi, M. A., Vora, P., Venugopal, C., Sidhu, S. S., Moffat, J., Swanton, C. & Singh, S. K. (2017) Intratumoral heterogeneity: pathways to treatment resistance and relapse in human glioblastoma. *Ann Oncol*, 28(7), 1448-1456.

Raby, L., Völkel, P., Le Bourhis, X. & Angrand, P. O. (2020) The Polycomb Orthologues in Teleost Fishes and Their Expression in the Zebrafish Model. *Genes (Basel)*, 11(4), 362.

Rana, R., Huirem, R. S., Kant, R., Chauhan, K., Sharma, S., Yashavarddhan, M. H., Chhabra, S. S., Acharya, R., Kalra, S. K., Gupta, A., Jain, S. & Ganguly, N. K. (2022) Cytochrome C as a potential clinical marker for diagnosis and treatment of glioma. *Front Oncol*, 12, 960787.

Rapp, M., Baernreuther, J., Turowski, B., Steiger, H. J., Sabel, M. & Kamp, M. A. (2017) Recurrence Pattern Analysis of Primary Glioblastoma. *World Neurosurg*, 103, 733-740.

Refet-Mollof, E., Najyb, O., Chermat, R., Glory, A., Lafontaine, J., Wong, P. & Gervais, T. (2021) Hypoxic Jumbo Spheroids On-A-Chip (HOnAChip): Insights into Treatment Efficacy. *Cancers (Basel)*, 13(16), 4046.

Richmond, A. & Su, Y. (2008) Mouse xenograft models vs GEM models for human cancer therapeutics. *Dis Model Mech*, 1(2-3), 78-82.

Riley, A., Green, V., Cheah, R., McKenzie, G., Karsai, L., England, J. & Greenman, J. (2019) A novel microfluidic device capable of maintaining functional thyroid carcinoma specimens ex vivo provides a new drug screening platform. *BMC Cancer*, 19(1), 259.

Riley, A., Jones, H., England, J., Kuvshinov, D., Green, V. & Greenman, J. (2021) Identification of soluble tissue-derived biomarkers from human thyroid tissue explants maintained on a microfluidic device. *Oncol Lett*, 22(5), 780.

Rock, K., McArdle, O., Forde, P., Dunne, M., Fitzpatrick, D., O'Neill, B. & Faul, C. (2012) A clinical review of treatment outcomes in glioblastoma multiforme--the validation in a non-trial population of the results of a randomised Phase III clinical trial: has a more radical approach improved survival? *Br J Radiol*, 85(1017), e729-33.

Rossi, G., Manfrin, A. & Lutolf, M. P. (2018) Progress and potential in organoid research. *Nat Rev Genet*, 19(11), 671-687.

Roy, S., Kumaravel, S., Sharma, A., Duran, C. L., Bayless, K. J. & Chakraborty, S. (2020) Hypoxic tumor microenvironment: Implications for cancer therapy. *Exp Biol Med (Maywood)*, 245(13), 1073-1086.

Ruigrok, M. J. R., Xian, J. L., Frijlink, H. W., Melgert, B. N., Hinrichs, W. L. J. & Olinga, P. (2018) siRNA-mediated protein knockdown in precision-cut lung slices. *Eur J Pharm Biopharm*, 133, 339-348.

Ryu, E. B., Chang, J. M., Seo, M., Kim, S. A., Lim, J. H. & Moon, W. K. (2014) Tumour volume doubling time of molecular breast cancer subtypes assessed by serial breast ultrasound. *Eur Radiol*, 24(9), 2227-35.

Ryu, N. E., Lee, S. H. & Park, H. (2019) Spheroid Culture System Methods and Applications for Mesenchymal Stem Cells. *Cells*, 8(12), 1620.

Sahu, U., Barth, R. F., Otani, Y., McCormack, R. & Kaur, B. (2022) Rat and Mouse Brain Tumor Models for Experimental Neuro-Oncology Research. *J Neuropathol Exp Neurol*, 81(5), 312-329.

Saito, M., Seo, Y., Yano, Y., Miki, A., Yoshida, M. & Azuma, T. (2012) A high value of serum des-γ-carboxy prothrombin before hepatocellular carcinoma treatment can be associated with long-term liver dysfunction after treatment. *J Gastroenterol*, 47(10), 1134-42.

Santo, V. E., Estrada, M. F., Rebelo, S. P., Abreu, S., Silva, I., Pinto, C., Veloso, S. C., Serra, A. T., Boghaert, E., Alves, P. M. & Brito, C. (2016) Adaptable stirred-tank culture strategies for large scale production of multicellular spheroid-based tumor cell models. *J Biotechnol*, 221, 118-29.

Schneider, A. C., Heukamp, L. C., Rogenhofer, S., Fechner, G., Bastian, P. J., von Ruecker, A., Müller, S. C. & Ellinger, J. (2011) Global histone H4K20 trimethylation predicts cancer-specific survival in patients with muscle-invasive bladder cancer. *BJU Int*, 108(8 Pt 2), E290-6.

Schulte, J. D., Aghi, M. K. & Taylor, J. W. (2021) Anti-angiogenic therapies in the management of glioblastoma. *Chin Clin Oncol*, 10(4), 37.

Senft, C., Franz, K., Blasel, S., Oszvald, A., Rathert, J., Seifert, V. & Gasser, T. (2010) Influence of iMRI-guidance on the extent of resection and survival of patients with glioblastoma multiforme. *Technol Cancer Res Treat*, 9(4), 339-46.

Sennett, C. (2019) Response of brain tumour spheroids to therapeutic agents in a microfluidic environment., MSc Thesis.

Shao, F. & Liu, C. (2018) Revisit the Candidacy of Brain Cell Types as the Cell(s) of Origin for Human High-Grade Glioma. *Front Mol Neurosci*, 11, 48.

Shen, Y., Li, S., Wang, X., Wang, M., Tian, Q., Yang, J., Wang, J., Wang, B., Liu, P. & Yang, J. (2019) Tumor vasculature remolding by thalidomide increases delivery and efficacy of cisplatin. *J Exp Clin Cancer Res*, 38(1), 427.

Shergalis, A., Bankhead, A., 3rd, Luesakul, U., Muangsin, N. & Neamati, N. (2018) Current Challenges and Opportunities in Treating Glioblastoma. *Pharmacol Rev*, 70(3), 412-445.

Shi, J., Dong, B., Zhou, P., Guan, W. & Peng, Y. (2017) Functional network analysis of gene-phenotype connectivity associated with temozolomide. *Oncotarget*, 8(50), 87554-87567.

Shrestha, J., Razavi Bazaz, S., Aboulkheyr Es, H., Yaghobian Azari, D., Thierry, B., Ebrahimi Warkiani, M. & Ghadiri, M. (2020) Lung-on-a-chip: the future of respiratory disease models and pharmacological studies. *Crit Rev Biotechnol*, 40(2), 213-230.

Shukla, G., Alexander, G. S., Bakas, S., Nikam, R., Talekar, K., Palmer, J. D. & Shi, W. (2017) Advanced magnetic resonance imaging in glioblastoma: a review. *Chin Clin Oncol*, 6(4), 40.

Sidoli, S. & Garcia, B. A. (2017) Characterization of Individual Histone Posttranslational Modifications and Their Combinatorial Patterns by Mass Spectrometry-Based Proteomics Strategies. *Methods Mol Biol*, 1528, 121-148.

Skaga, E., Kulesskiy, E., Brynjulvsen, M., Sandberg, C. J., Potdar, S., Langmoen, I. A., Laakso, A., Gaál-Paavola, E., Perola, M., Wennerberg, K. & Vik-Mo, E. O. (2019) Feasibility study of using high-throughput drug sensitivity testing to target recurrent glioblastoma stem cells for individualized treatment. *Clin Transl Med*, 8(1), 33.

Skaga, E., Kulesskiy, E., Potdar, S., Panagopoulos, I., Micci, F., Langmoen, I. A., Sandberg, C. J. & Vik-Mo, E. O. (2022) Functional temozolomide sensitivity testing of patient-specific glioblastoma stem cell cultures is predictive of clinical outcome. *Transl Oncol*, 26, 101535.

So, J. S., Kim, H. & Han, K. S. (2021) Mechanisms of Invasion in Glioblastoma: Extracellular Matrix, Ca(2+) Signaling, and Glutamate. *Front Cell Neurosci*, 15, 663092.

Stacker, S. A. & Achen, M. G. (2013) The VEGF signaling pathway in cancer: the road ahead. *Chin J Cancer*, 32(6), 297-302.

Stangegaard, M., Dufva, I. H. & Dufva, M. (2006) Reverse transcription using random pentadecamer primers increases yield and quality of resulting cDNA. *Biotechniques*, 40(5), 649-57.

Stensjøen, A. L., Solheim, O., Kvistad, K. A., Håberg, A. K., Salvesen, Ø. & Berntsen, E. M. (2015) Growth dynamics of untreated glioblastomas in vivo. *Neuro Oncol*, 17(10), 1402-11.

Stichel, D., Ebrahimi, A., Reuss, D., Schrimpf, D., Ono, T., Shirahata, M., Reifenberger, G., Weller, M., Hänggi, D., Wick, W., Herold-Mende, C., Westphal, M., Brandner, S., Pfister, S. M., Capper, D., Sahm, F. & von Deimling, A. (2018) Distribution of EGFR amplification, combined chromosome 7 gain and chromosome 10 loss, and TERT promoter mutation in brain tumors and their potential for the reclassification of IDHwt astrocytoma to glioblastoma. *Acta Neuropathol*, 136(5), 793-803.

Stupp, R., Hegi, M. E., Mason, W. P., van den Bent, M. J., Taphoorn, M. J., Janzer, R. C., Ludwin, S. K., Allgeier, A., Fisher, B., Belanger, K., Hau, P., Brandes, A. A., Gijtenbeek, J., Marosi, C., Vecht, C. J., Mokhtari, K., Wesseling, P., Villa, S., Eisenhauer, E., Gorlia, T., Weller, M., Lacombe, D., Cairncross, J. G. & Mirimanoff, R. O. (2009) Effects of radiotherapy with concomitant and adjuvant temozolomide versus radiotherapy alone on survival in glioblastoma in a randomised phase

III study: 5-year analysis of the EORTC-NCIC trial. *Lancet Oncol*, 10(5), 459-66.

Stupp, R., Mason, W. P., van den Bent, M. J., Weller, M., Fisher, B., Taphoorn, M. J., Belanger, K., Brandes, A. A., Marosi, C., Bogdahn, U., Curschmann, J., Janzer, R. C., Ludwin, S. K., Gorlia, T., Allgeier, A., Lacombe, D., Cairncross, J. G., Eisenhauer, E. & Mirimanoff, R. O. (2005) Radiotherapy plus concomitant and adjuvant temozolomide for glioblastoma. *N Engl J Med*, 352(10), 987-96.

Stupp, R., Taillibert, S., Kanner, A., Read, W., Steinberg, D., Lhermitte, B., Toms, S., Idbaih, A., Ahluwalia, M. S., Fink, K., Di Meco, F., Lieberman, F., Zhu, J. J., Stragliotto, G., Tran, D., Brem, S., Hottinger, A., Kirson, E. D., Lavy-Shahaf, G., Weinberg, U., Kim, C. Y., Paek, S. H., Nicholas, G., Bruna, J., Hirte, H., Weller, M., Palti, Y., Hegi, M. E. & Ram, Z. (2017) Effect of Tumor-Treating Fields Plus Maintenance Temozolomide vs Maintenance Temozolomide Alone on Survival in Patients With Glioblastoma: A Randomized Clinical Trial. *Jama*, 318(23), 2306-2316.

Taherbhoy, A. M., Huang, O. W. & Cochran, A. G. (2015) BMI1-RING1B is an autoinhibited RING E3 ubiquitin ligase. *Nat Commun*, 6, 7621.

Tajul-Arifin, K., Teasdale, R., Ravasi, T., Hume, D. A. & Mattick, J. S. (2003) Identification and analysis of chromodomain-containing proteins encoded in the mouse transcriptome. *Genome Res*, 13(6b), 1416-29.

Tamimi, A. F. & Juweid, M. (2017) Epidemiology and Outcome of Glioblastoma, in De Vleeschouwer, S. (ed), *Glioblastoma*. Translated from eng by. Brisbane (AU): Codon Publications.

Taniguchi, T., Endo, K. I., Tanioka, H., Sasaoka, M., Tashiro, K., Kinoshita, S. & Kageyama, M. (2020) Novel use of a chemically modified siRNA for robust and sustainable in vivo gene silencing in the retina. *Sci Rep*, 10(1), 22343.

Tanweer, F., Green, V. L., Stafford, N. D. & Greenman, J. (2013) Application of microfluidic systems in management of head and neck squamous cell carcinoma. *Head Neck*, 35(5), 756-63.

Thermo-Scientific (2012) Interpretation of Nucleic Acid 260/280 Ratios. (T123 – TECHNICAL BULLETIN). Available online: https://assets.thermofisher.com/TFS-Assets/CAD/Product-Bulletins/T123-NanoDrop-Lite-Interpretation-of-Nucleic-Acid-260-280-Ratios.pdf [Accessed 10/06/2023].

Tomaszewski, W., Sanchez-Perez, L., Gajewski, T. F. & Sampson, J. H. (2019) Brain Tumor Microenvironment and Host State: Implications for Immunotherapy. *Clin Cancer Res*, 25(14), 4202-4210.

Towner, R. A., Gillespie, D. L., Schwager, A., Saunders, D. G., Smith, N., Njoku, C. E., Krysiak, R. S., 3rd, Larabee, C., Iqbal, H., Floyd, R. A., Bourne, D. W., Abdullah, O., Hsu, E. W. & Jensen, R. L. (2013) Regression of glioma tumor growth in F98 and U87 rat glioma models by the Nitrone OKN-007. *Neuro Oncol*, 15(3), 330-40.

Towner, R. A., Smith, N., Saunders, D., Brown, C. A., Cai, X., Ziegler, J., Mallory, S., Dozmorov, M. G., Coutinho De Souza, P., Wiley, G., Kim, K., Kang, S., Kong, D. S., Kim, Y. T., Fung, K. M., Wren, J. D. & Battiste, J. (2019) OKN-007 Increases temozolomide (TMZ) Sensitivity and Suppresses TMZ-Resistant Glioblastoma (GBM) Tumor Growth. *Transl Oncol*, 12(2), 320-335.

Unal, S., Arslan, S., Yilmaz, B. K., Oktar, F. N., Ficai, D., Ficai, A. & Gunduz, O. (2020) Polycaprolactone/Gelatin/Hyaluronic Acid Electrospun Scaffolds to Mimic Glioblastoma Extracellular Matrix. *Materials (Basel)*, 13(11), 2661.

Unnikrishnan, K., Thomas, L. V. & Ram Kumar, R. M. (2021) Advancement of Scaffold-Based 3D Cellular Models in Cancer Tissue Engineering: An Update. *Front Oncol*, 11, 733652.

Vagia, E., Mahalingam, D. & Cristofanilli, M. (2020) The Landscape of Targeted Therapies in TNBC. *Cancers (Basel)*, 12(4), 916.

Valdoz, J. C., Johnson, B. C., Jacobs, D. J., Franks, N. A., Dodson, E. L., Sanders, C., Cribbs, C. G. & Van Ry, P. M. (2021) The ECM: To Scaffold, or Not to Scaffold, That Is the Question. *Int J Mol Sci*, 22(23), 12690.

van Wijnen, A. J., Bagheri, L., Badreldin, A. A., Larson, A. N., Dudakovic, A., Thaler, R., Paradise, C. R. & Wu, Z. (2021) Biological functions of chromobox (CBX) proteins in stem cell self-renewal, lineage-commitment, cancer and development. *Bone*, 143, 115659.

Van Zundert, I., Fortuni, B. & Rocha, S. (2020) From 2D to 3D Cancer Cell Models-The Enigmas of Drug Delivery Research. *Nanomaterials (Basel)*, 10(11), 2236.

Velásquez, C., Mansouri, S., Mora, C., Nassiri, F., Suppiah, S., Martino, J., Zadeh, G. & Fernández-Luna, J. L. (2019) Molecular and Clinical Insights into the Invasive Capacity of Glioblastoma Cells. *J Oncol*, 2019, 1740763.

Vitovcova, B., Skarkova, V., Rudolf, K. & Rudolf, E. (2020) Biology of Glioblastoma Multiforme-Exploration of Mitotic Catastrophe as a Potential Treatment Modality. *Int J Mol Sci*, 21(15), 5324.

Vora, P., Venugopal, C., Salim, S. K., Tatari, N., Bakhshinyan, D., Singh, M., Seyfrid, M., Upreti, D., Rentas, S., Wong, N., Williams, R., Qazi, M. A., Chokshi, C., Ding, A., Subapanditha, M., Savage, N., Mahendram, S., Ford, E., Adile, A. A., McKenna, D., McFarlane, N., Huynh, V., Wylie, R. G., Pan, J., Bramson, J., Hope, K., Moffat, J. & Singh, S. (2020) The Rational Development of CD133-Targeting Immunotherapies for Glioblastoma. *Cell Stem Cell*, 26(6), 832-844.e6.

Wang, L., Ren, B., Zhuang, H., Zhong, Y. & Nan, Y. (2021) CBX2 Induces Glioma Cell Proliferation and Invasion Through the Akt/PI3K Pathway. *Technol Cancer Res Treat*, 20, 15330338211045831.

Wang, N., Jain, R. K. & Batchelor, T. T. (2017a) New Directions in Anti-Angiogenic Therapy for Glioblastoma. *Neurotherapeutics*, 14(2), 321-332.

Wang, Y., Kong, X., Guo, Y., Wang, R. & Ma, W. (2017b) Continuous dose-intense temozolomide and cisplatin in recurrent glioblastoma patients. *Medicine (Baltimore)*, 96(10), e6261.

Wang, Y., Xing, D., Zhao, M., Wang, J. & Yang, Y. (2016) The Role of a Single Angiogenesis Inhibitor in the Treatment of Recurrent Glioblastoma Multiforme: A Meta-Analysis and Systematic Review. *PLoS One*, 11(3), e0152170.

Wang, Y. I., Abaci, H. E. & Shuler, M. L. (2017c) Microfluidic blood-brain barrier model provides in vivo-like barrier properties for drug permeability screening. *Biotechnol Bioeng*, 114(1), 184-194.

Waters, E. J. (2019) Investigating the role of CBX2 in ER positive breast cancer, MSc Thesis.

Wei, Y., Lu, C., Zhou, P., Zhao, L., Lyu, X., Yin, J., Shi, Z. & You, Y. (2021) EIF4A3-induced circular RNA ASAP1 promotes tumorigenesis and temozolomide resistance of glioblastoma via NRAS/MEK1/ERK1-2 signaling. *Neuro Oncol*, 23(4), 611-624.

Welch, W. C., Morrison, R. S., Gross, J. L., Gollin, S. M., Kitson, R. B., Goldfarb, R. H., Giuliano, K. A., Bradley, M. K. & Kornblith, P. L. (1995) Morphologic, immunologic, biochemical, and cytogenetic characteristics of the human glioblastoma-derived cell line, SNB-19. *In Vitro Cell Dev Biol Anim*, 31(8), 610-6.

Wheeler, L. J., Watson, Z. L., Qamar, L., Yamamoto, T. M., Post, M. D., Berning, A. A., Spillman, M. A., Behbakht, K. & Bitler, B. G. (2018) CBX2 identified as driver of anoikis escape and dissemination in high grade serous ovarian cancer. *Oncogenesis*, 7(11), 92.

Wilson, T. A., Karajannis, M. A. & Harter, D. H. (2014) Glioblastoma multiforme: State of the art and future therapeutics. *Surg Neurol Int*, 5, 64.

Witthayanuwat, S., Pesee, M., Supaadirek, C., Supakalin, N., Thamronganantasakul, K. & Krusun, S. (2018) Survival Analysis of Glioblastoma Multiforme. *Asian Pac J Cancer Prev*, 19(9), 2613-2617.

Wong, C. H., Siah, K. W. & Lo, A. W. (2019) Estimation of clinical trial success rates and related parameters. *Biostatistics*, 20(2), 273-286.

Wu, W., Klockow, J. L., Zhang, M., Lafortune, F., Chang, E., Jin, L., Wu, Y. & Daldrup-Link, H. E. (2021) Glioblastoma multiforme (GBM): An overview of current therapies and mechanisms of resistance. *Pharmacol Res*, 171, 105780.

Xiong, Z., Liu, H., He, C. & Li, X. (2021) Hypoxia Contributes to Poor Prognosis in Primary IDH-wt GBM by Inducing Tumor Cells MES-Like Transformation Trend and Inhibiting Immune Cells Activity. *Front Oncol*, 11, 782043.

Xiong, Z., Yang, Q. & Li, X. (2020) Effect of intra- and inter-tumoral heterogeneity on molecular characteristics of primary IDH-wild type glioblastoma revealed by single-cell analysis. *CNS Neurosci Ther*, 26(9), 981-989.

Xu, H., Li, Z., Yu, Y., Sizdahkhani, S., Ho, W. S., Yin, F., Wang, L., Zhu, G., Zhang, M., Jiang, L., Zhuang, Z. & Qin, J. (2016) A dynamic in vivo-like organotypic blood-brain barrier model to probe metastatic brain tumors. *Sci Rep*, 6, 36670.

Yang, Y. F., Pan, Y. H., Tian, Q. H., Wu, D. C. & Su, S. G. (2018) CBX1 Indicates Poor Outcomes and Exerts Oncogenic Activity in Hepatocellular Carcinoma. *Transl Oncol*, 11(5), 1110-1118.

Yao, M., Li, S., Wu, X., Diao, S., Zhang, G., He, H., Bian, L. & Lu, Y. (2018) Cellular origin of glioblastoma and its implication in precision therapy. *Cell Mol Immunol*, 15(8), 737-739.

Yee, P. P., Wei, Y., Kim, S. Y., Lu, T., Chih, S. Y., Lawson, C., Tang, M., Liu, Z., Anderson, B., Thamburaj, K., Young, M. M., Aregawi, D. G., Glantz, M. J., Zacharia, B. E., Specht, C. S., Wang, H. G. & Li, W. (2020) Neutrophil-induced ferroptosis promotes tumor necrosis in glioblastoma progression. *Nat Commun*, 11(1), 5424.

Yu, W., Gius, D., Onyango, P., Muldoon-Jacobs, K., Karp, J., Feinberg, A. P. & Cui, H. (2008) Epigenetic silencing of tumour suppressor gene p15 by its antisense RNA. *Nature*, 451(7175), 202-6.

Zanotelli, M. R. & Reinhart-King, C. A. (2018) Mechanical Forces in Tumor Angiogenesis. *Adv Exp Med Biol*, 1092, 91-112.

Zeng, M., Li, B., Yang, L. & Guan, Q. (2021) CBX2 depletion inhibits the proliferation, invasion and migration of gastric cancer cells by inactivating the YAP/β-catenin pathway. *Mol Med Rep*, 23(2), 137.

Zhang, C., Molascon, A. J., Gao, S., Liu, Y. & Andrews, P. C. (2013) Quantitative proteomics reveals that the specific methyltransferases Txr1p and Ezl2p differentially affect the mono-, di- and trimethylation states of histone H3 lysine 27 (H3K27). *Mol Cell Proteomics*, 12(6), 1678-88.

Zhang, M., Xu, C., Jiang, L. & Qin, J. (2018) A 3D human lung-on-a-chip model for nanotoxicity testing. *Toxicol Res (Camb)*, 7(6), 1048-1060.

Zhang, P., Yang, X., Zha, Z., Zhu, Y., Zhang, G. & Li, G. (2022) CBX3 regulated by miR-139 promotes the development of HCC by regulating cell cycle progression. *Cell Cycle*, 21(16), 1740-1752.

Zhang, T., Cooper, S. & Brockdorff, N. (2015) The interplay of histone modifications - writers that read. *EMBO Rep*, 16(11), 1467-81.

Zhang, X. N., Yang, K. D., Chen, C., He, Z. C., Wang, Q. H., Feng, H., Lv, S. Q., Wang, Y., Mao, M., Liu, Q., Tan, Y. Y., Wang, W. Y., Li, T. R., Che, L. R., Qin, Z. Y., Wu, L. X., Luo, M., Luo, C. H., Liu, Y. Q., Yin, W., Wang, C., Guo, H. T., Li, Q. R., Wang, B., Chen, W., Wang, S., Shi, Y., Bian, X.

W. & Ping, Y. F. (2021) Pericytes augment glioblastoma cell resistance to temozolomide through CCL5-CCR5 paracrine signaling. *Cell Res*, 31(10), 1072-1087.

Zhang, Z., Jones, A. E., Wu, W., Kim, J., Kang, Y., Bi, X., Gu, Y., Popov, I. K., Renfrow, M. B., Vassylyeva, M. N., Vassylyev, D. G., Giles, K. E., Chen, D., Kumar, A., Fan, Y., Tong, Y., Liu, C. F., An, W., Chang, C., Luo, J., Chow, L. T. & Wang, H. (2017) Role of remodeling and spacing factor 1 in histone H2A ubiquitination-mediated gene silencing. *Proc Natl Acad Sci U S A*, 114(38), E7949-e7958.

Zhang, Z., Yin, J., Lu, C., Wei, Y., Zeng, A. & You, Y. (2019) Exosomal transfer of long non-coding RNA SBF2-AS1 enhances chemoresistance to temozolomide in glioblastoma. *J Exp Clin Cancer Res*, 38(1), 166.

Zheng, S., Lv, P., Su, J., Miao, K., Xu, H. & Li, M. (2019) Overexpression of CBX2 in breast cancer promotes tumor progression through the PI3K/AKT signaling pathway. *Am J Transl Res*, 11(3), 1668-1682.

Zheng, Z. Q., Chen, J. T., Zheng, M. C., Yang, L. J., Wang, J. M., Liu, Q. L., Chen, L. F., Ye, Z. C., Lin, J. M. & Lin, Z. X. (2021) Nestin+/CD31+ cells in the hypoxic perivascular niche regulate glioblastoma chemoresistance by upregulating JAG1 and DLL4. *Neuro Oncol*, 23(6), 905-919.

Zheng, Z. Q., Yuan, G. Q., Kang, N. L., Nie, Q. Q., Zhang, G. G. & Wang, Z. (2022) Chromobox 7/8 serve as independent indicators for glioblastoma via promoting proliferation and invasion of glioma cells. *Front Neurol*, 13, 912039.

Zhou, H., Xiong, Y., Liu, Z., Hou, S. & Zhou, T. (2021) Expression and prognostic significance of CBX2 in colorectal cancer: database mining for CBX family members in malignancies and vitro analyses. *Cancer Cell Int*, 21(1), 402.

Zimna, A. & Kurpisz, M. (2015) Hypoxia-Inducible Factor-1 in Physiological and Pathophysiological Angiogenesis: Applications and Therapies. *Biomed Res Int*, 2015, 549412.